Lithium Extraction via Mechanochemical Treatment of End-of-Life Glass-Ceramics and Lithium Silicate Minerals

Lithiumextraktion durch mechanochemische Behandlung von ausgedienten Glaskeramiken und Lithiumsilikat Mineralen

Genehmigte Dissertation zur Erlangung des Grades eines
Doktors der Naturwissenschaften (Dr. rer. nat.)

von Tobias Necke geboren in Worms

Erstgutachter: Prof. Dr. Hans-Joachim Kleebe
Zweitgutachter: Prof. Dr. Christoph Schüth

Institut für Angewandte Geowissenschaften, Fachbereich Material- und Geowissenschaften,
Technische Universität Darmstadt, 2024

TECHNISCHE
UNIVERSITÄT
DARMSTADT

Lithium Extraction via Mechanochemical Treatment of End-of-Life Glass-Ceramics and Lithium Silicate Minerals

Lithiumextraktion durch mechanochemische Behandlung von ausgedienten Glaskeramiken und Lithiumsilikat Mineralen

Genehmigte Dissertation von Tobias Necke geboren in Worms

Tag der Einreichung: 28.05.2024
Tag der Prüfung: 13.08.2024

Darmstadt, Technische Universität Darmstadt

Jahr der Veröffentlichung der Dissertation auf TUprints: 2024
URN: urn:nbn:de:tuda-tuprints-280502

Erklärungen laut Promotionsordnung

§ 8 Abs. 1 lit. c PromO

Ich versichere hiermit, dass die elektronische Version meiner Dissertation mit der schriftlichen Version übereinstimmt.

§ 8 Abs. 1 lit. d PromO

Ich versichere hiermit, dass zu einem vorherigen Zeitpunkt noch keine Promotion versucht wurde.

§ 9 Abs. 1 PromO

Ich versichere hiermit, dass die vorliegende Dissertation selbstständig und nur unter Verwendung der angegebenen Quellen verfasst wurde.

§ 9 Abs. 2 PromO

Die Arbeit hat bisher noch nicht zu Prüfungszwecken gedient.

Darmstadt, 28.05.2024

Tobias Necke

Content

Content I

Abbreviations III

Symbols IV

Abstract V

Zusammenfassung VII

1 Introduction 1

1.1 Motivation and Concept 1

1.2 Objectives 2

2 Fundamentals 4

2.1 Mechanochemistry 4
2.1.1 Definitions 4
2.1.2 Historical Background 4
2.1.3 Theoretical Background 5
2.1.4 Mechanochemical Reactors 6
2.1.5 Applications 8

2.2 The Alkali Metal Lithium 9
2.2.1 History and Discovery 9
2.2.2 Lithium Chemistry 10
2.2.3 Lithium Minerals and Deposits 11
2.2.4 Investigated Lithium Minerals 14

2.3 Lithium Extraction of Primary and Secondary Sources 16
2.3.1 Lithium Resources and Reserves 16
2.3.2 Processing of Lithium Brines 16
2.3.3 Beneficiation and Pretreatment of Hard Rock Ores 17
2.3.4 Lithium Extraction of Hard Rock Ores 18
2.3.5 Lithium Recovery of LAS Glass-Ceramics 22

2.4 Applications of Lithium and its Compounds 23
2.4.1 Overview of the Industrial Applications 23
2.4.2 Lithium-Ion Batteries (LIB) 24
2.4.3 LAS Glass-Ceramics 25

3 Experimental Procedures 27

3.1 Sample Treatment 27
3.1.1 Utilized Chemicals 27
3.1.2 Sample Materials and Pretreatment 27
3.1.3 Reference Experiments 29
3.1.4 Mechanochemical Leaching Experiments 29
3.1.5 Desilication Experiments 30
3.1.6 Precipitation of Lithium Compounds 30
3.1.7 Adsorption Experiments 32

3.2 Analytical Techniques 33

3.2.1 Inductively Coupled Plasma Optical Emission Spectrometry (ICP-OES) ... 33
3.2.2 Powder X-ray Diffraction (PXRD) ... 35
3.2.3 Fourier Transform Infrared Spectroscopy (FT-IR) ... 36
3.2.4 Gas Adsorption/Desorption ... 37
3.2.5 Optical Microscopy (OM) ... 38
3.2.6 Scanning Electron Microscopy (SEM) ... 38
3.2.7 Transmission Electron Microscopy (TEM) ... 39
3.2.8 Energy-Dispersive X-ray Spectroscopy (EDS) ... 39
3.2.9 Determination of the Loss on Ignition (LOI) ... 40
3.2.10 Particle Size Measurements ... 40

4 Results and Discussion ... 41

4.1 Characterization of the Feed Materials ... 41
4.1.1 Chemical Investigations via ICP-OES ... 41
4.1.2 Structural Characterization via PXRD ... 42
4.1.3 Microscopic Investigations using OM, SEM and SEM-EDS ... 44
4.1.4 TEM Investigation on LAS Glass-Ceramic Samples ... 46

4.2 Mechanochemical Treatments of LAS Glass-Ceramics ... 49
4.2.1 Experimental Results at Various NaOH Concentrations and Reaction Times ... 49
4.2.2 Influences of Rotational Speed and Ball-to-Powder Ratio ... 52
4.2.3 Intermittent Milling Experiments and the Role of Temperature ... 54
4.2.4 Reference Experiments including Regular Leaching ... 55
4.2.5 Reference Experiments including Ball Milling in Water ... 56
4.2.6 Structural Changes and Physicochemical Properties of Leaching Residues ... 57
4.2.7 SEM and TEM Investigations ... 59

4.3 Mechanochemical Treatment of Primary Lithium Minerals ... 62
4.3.1 Lithium Recovery at Favorable Experimental Conditions ... 62
4.3.2 Structural Changes and Physicochemical Properties of Leaching Residues ... 63
4.3.3 Reference Experiments ... 66
4.3.4 Influence of Different Crystal Structures on the Leachability of Lithium ... 68
4.3.5 Discussion of the Results in the Context of the Literature ... 70
4.3.6 Wear of the Milling Balls during Mechanochemical Experiments ... 70

4.4 Hydrometallurgical Procedures on Enriched Solutions ... 73
4.4.1 Desilication Experiments of NaOH Solutions ... 73
4.4.2 Precipitation of Lithium as Li_3PO_4 ... 75
4.4.3 Transformation of Li_3PO_4 into $LiOH \cdot H_2O$ ... 76
4.4.4 Discussion of the Overall Results ... 77

4.5 Adsorption Studies on Zeolite Byproducts ... 79

5 Conclusions and Outlook ... 82

6 References ... 85

List of Figures ... 94

List of Tables ... 97

Acknowledgments ... 98

Publications & Conference Contributions ... 99

Abbreviations

BET	Brunauer-Emmet-Teller
BF	Bright-field
BSE	Backscattered electrons
BPR	Ball-to-powder ratio
CTE	Coefficient of thermal expansion
EDS	Energy-dispersive X-ray spectroscopy
FFT	Fast Fourier transformation
FT-IR	Fourier transform infrared spectroscopy
FWHM	Full width at half maximum
GIS	Gismondine type framework
HRTEM	High-resolution transmission electron microscopy
ICP-OES	Inductively coupled plasma optical emission spectrometry
LAS	Lithium-Alumina-Silica
LCO	Lithium cobalt oxide
LCT	Lithium-Cesium-Tantalum
LIB	Lithium-ion battery
LOI	Loss on ignition
Lpd	Lepidolite
LSR	Liquid-to-solid ratio
LTA	Linde Type A zeolite framework
LTN	Linde Type N zeolite framework
OM	Optical microscopy
Ptl	Petalite
PXRD	Powder X-ray diffraction
QTZ	Quartz
RIR	Reference Intensity Ratio
SAED	Selective area electron diffraction
SE	Secondary electron
SEM	Scanning electron microscopy
SOD	Sodalite type framework
Spd	Spodumene
TEM	Transmission electron microscopy

Symbols

B	Broadening at full width at half maximum
C	Empirical constant
C_0	Mass concentration of metal ions in the leachate
C_f	Final concentration of metal ions
C_i	Initial concentration of metal ions
d	Spacing of lattice planes
D	Crystallite size
d_{10}, d_{50}, d_{90}	Volume fractions (10; 50; 90 %) in particle size distribution
E, E^*	Activation energy of an ordered phase, disordered phase
i	Intercept with the Y-axis
K	Scherrer constant
k, k^*	Rate constant during leaching of an ordered phase, disordered phase
λ	Wavelength radiation
m	Sample mass
n	Natural number
N_A	Avogadro number
p, p_0	Pressure, saturation pressure
R	Gas constant
R_{Li}	Extraction rate for lithium
s	Adsorption cross section
S_{BET}	BET surface area
T	Reaction Temperature
Θ	Bragg angle
V_c	Total volume of all cations and anions per formula unit
V_l	Total volume of the unit cell
v, v_m	Adsorbed volume, adsorbed volume monolayer
V_o	Leachte volume
w%	Metal mass fraction
Z	Ionic porosity

Abstract

Owing to recent trends in e-mobility, lithium is in high demand resulting in increased global production and record prices for lithium ores and compounds. Accordingly, many efforts are being made to maintain supply by exploiting primary resources around the world, while effective lithium recycling from secondary sources is still lacking. Concerning primary pegmatite ores, the current state of industrial technology necessitates energy intense high-temperature pretreatments to increase the reactivity of the refractory lithium minerals prior to leaching. Moreover, these routes are focused only on the low but economically relevant lithium content, disregarding the main components Al and Si, leading to large quantities of leaching residues. In addition to primary lithium minerals, a similar chemical assemblage of elements is found in secondary raw materials, such as Li_2O-Al_2O_3-SiO_2 glass-ceramics (LAS), which can be seen as an untapped urban source of lithium found in significant quantities in discarded electrical appliances. Although the recycling of these devices is already established, large quantities of valuable lithium are lost on this disposal route, as recycling has so far only concentrated on recovering the transition metals while neglecting the glass-ceramic sections. Encouraged by these circumstances, the present dissertation investigated a holistic approach that attempts to utilize the entire chemical inventory of the feedstock materials, leading to various value-added by-products during extraction and downstream hydrometallurgical treatments on the way to a pure lithium compound. For this study, a LAS glass-ceramic plate from an end-of-life cooktop and naturally occurring lithium silicate minerals such as lepidolite, spodumene and petalite were selected as source materials for alkaline mechanochemical studies, focusing on lithium extraction without thermal pretreatments.

The first section addresses the experimental investigations of the LAS samples, leading to efficient decomposition of the lithium-containing β-quartz phase under alkaline conditions, while lithium was significantly enriched in the leach liquor. Optimal experimental parameters were identified at a NaOH concentration, a rotational speed and a ball-to-powder ratio of 7 mol/L, 600 rpm and 50:1 g/g respectively, resulting in a substantial extraction of up to 92.4 %. In addition to leaching, the entire feedstock was transformed into different zeolite frameworks as a function of NaOH concentration.

In the second section, the findings from the investigations of LAS samples were transferred to the three most common lithium silicate minerals lepidolite, spodumene and petalite. In these studies, petalite was identified to be significantly more compatible with the chosen mechanochemical approach compared to spodumene or lepidolite. This resulted in a considerable lithium extraction of up to 84.9 %, while in parallel a nearly complete conversion of petalite into a sodalite zeolite was achieved. The significantly higher reactivity of petalite under mechanochemical conditions was associated with specific features in its crystal structure, such as the less dense atomic packing and the pronounced activation of cleavage planes along the lithium sites during ball milling.

Unavoidably, as a side effect of alkaline leaching, parts of the silicon from the starting materials went into solution during the mechanochemical experiments, necessitating desilication as an intermediate step prior to lithium precipitation. CaO proved to be an effective agent leading to high desilication rates for LAS- and petalite-based solutions, while the lithium content remained unaffected in both cases. Upon purification of the solution by desilication, lithium was precipitated by adding moderate amounts of phosphoric acid, permitting the formation of sparingly soluble Li_3PO_4 at specific P:Li ratios. In a final step, the obtained Li_3PO_4 was further treated

with $Ca(OH)_2$, resulting in the precipitation of hydroxyapatite $Ca_5(PO_4)_3OH$ and the formation of lithium hydroxide $LiOH \cdot H_2O$ in solution, which can be crystallized to a pure phase after filtration. In addition, Ca-silicate phases, formed during the desilication of the enriched solution, as well as apatite, resulting from the transformation procedure, are regarded as value-added byproducts as they offer specific applications and thus correspond to the holistic approach.

The leaching residues obtained during mechanochemical treatments of LAS or petalite samples revealed comparable high specific surface areas, and consisted mainly of sodalite and/or LTN zeolites, renowned for their special properties in molecular sieving or selective adsorption. Accordingly, these byproducts were investigated as potential adsorbents in a side study, demonstrating excellent sorption performance for divalent heavy metal ions in synthetic wastewater samples.

Zusammenfassung

Aufgrund der jüngsten Trends im Bereich der Elektromobilität besteht eine hohe Nachfrage nach Lithium, was zu einem Anstieg der weltweiten Produktion und Rekordpreisen für Lithiumerze und -verbindungen geführt hat. Dementsprechend werden viele Anstrengungen unternommen, um das Angebot durch die Ausbeutung von primären Ressourcen auf der ganzen Welt aufrechtzuerhalten, während ein effektives Lithiumrecycling aus Sekundärquellen noch immer aussteht. Bei primären Pegmatit-Erzen erfordert der derzeitige Stand der industriellen Technik energieintensive Hochtemperaturvorbehandlungen, um die Reaktivität der refraktären Lithiumminerale vor der Laugung zu erhöhen. Außerdem konzentrieren sich diese Verfahren nur auf den geringen, aber wirtschaftlich relevanten Lithiumgehalt, wobei die Hauptbestandteile Al und Si außer Acht gelassen werden, was zu großen Mengen an Laugungsrückständen führt. Neben primären Lithiummineralen findet sich eine ähnliche chemische Zusammensetzung von Elementen in sekundären Rohstoffen wie Li_2O-Al_2O_3-SiO_2 Glaskeramik (LAS), die als ungenutzte urbane Lithiumquelle angesehen werden kann und in erheblichen Mengen in ausrangierten Elektrogeräten zu finden ist. Obwohl das Recycling dieser Geräte bereits etabliert ist, gehen auf diesem Entsorgungsweg große Mengen an wertvollem Lithium verloren, da sich das Recycling bisher nur auf die Rückgewinnung der Übergangsmetalle konzentriert und die Glaskeramik vernachlässigt. Motiviert durch diese Umstände wurde in der vorliegenden Dissertation ein ganzheitlicher Ansatz untersucht, der versucht, das gesamte chemische Inventar der Ausgangsmaterialien zu nutzen, was zu verschiedenen wertschöpfenden Nebenprodukten bei der Extraktion und nachgeschalteten hydrometallurgischen Behandlungen auf dem Weg zu einer reinen Lithiumverbindung führt. Für diese Studie wurden eine LAS-Glaskeramik aus einem ausgedienten Kochfeld und natürlich vorkommende lithiumhaltige Minerale wie Lepidolith, Spodumen und Petalit als Ausgangsmaterialien für alkalische mechanochemische Untersuchungen ausgewählt, wobei der Schwerpunkt auf der Lithiumextraktion ohne thermische Vorbehandlungen lag.

Der erste Abschnitt befasst sich mit den experimentellen Untersuchungen der LAS-Proben, die zu einer effizienten Zersetzung der lithiumhaltigen β-Quarz Phase unter alkalischen Bedingungen führten, während Lithium in der Laugungsflüssigkeit deutlich angereichert wurde. Als optimale Versuchsparameter wurden eine NaOH-Konzentration, eine Rotationsgeschwindigkeit und ein Kugel-Pulver-Verhältnis von 7 mol/L, 600 U/min bzw. 50:1 g/g ermittelt, was zu einer erheblichen Extraktion von bis zu 92,4 % führte. Zusätzlich zur Auslaugung wurde das gesamte Ausgangsmaterial in Abhängigkeit von der NaOH-Konzentration in verschiedene Zeolith-Strukturen umgewandelt.

Im zweiten Abschnitt wurden die Erkenntnisse aus den Untersuchungen der LAS-Proben auf die drei häufigsten lithiumhaltigen Silikat Minerale Lepidolith, Spodumen und Petalit übertragen. Dabei zeigte sich, dass Petalit im Vergleich zu Spodumen oder Lepidolith deutlich besser mit dem gewählten mechanochemischen Ansatz vereinbar ist. Dies führte zu einer beträchtlichen Lithiumextraktion von bis zu 84,9 %, während gleichzeitig eine nahezu vollständige Umwandlung von Petalit in einen Sodalith-Zeolith erreicht wurde. Die deutlich höhere Reaktivität von Petalit unter mechanochemischen Bedingungen wurde mit spezifischen Merkmalen seiner Kristallstruktur in Verbindung gebracht, wie der weniger dichten Atompackung und der ausgeprägten Aktivierung von Spaltebenen entlang der Lithium Positionen beim Kugelmahlen.

Als unvermeidlicher Nebeneffekt der alkalischen Auslaugung ging während der mechanochemischen Experimente ein Teil des Siliziums aus den Ausgangsmaterialien in Lösung, so dass eine Entkieselung als Zwischenschritt vor der Lithiumausfällung erforderlich wurde. CaO erwies sich als wirksames Mittel, das zu hohen Entkieselungsraten für LAS- und Petalit-basierte Lösungen führte, während der Lithiumgehalt in beiden Fällen unbeeinflusst blieb. Nach der Reinigung der Lösung durch Entkieselung wurde Lithium durch Zugabe moderater Mengen von Phosphorsäure ausgefällt, was die Bildung von schwerlöslichem Li_3PO_4 bei bestimmten P:Li-Verhältnissen ermöglichte. In einem letzten Schritt wurde das erhaltene Li_3PO_4 mit $Ca(OH)_2$ weiter behandelt, was zur Ausfällung von Hydroxylapatit $Ca_5(PO_4)_3OH$ und zur Bildung von $LiOH{\cdot}H_2O$ in Lösung führte, dass nach der Filtration zu einer reinen Verbindung kristallisiert werden kann. Zusätzlich, werden Ca-Silikat Phasen, die bei der Entkieselung der angereicherten Lösung entstehen, oder Hydroxyapatit, der aus dem Umwandlungsverfahren resultiert, als wertsteigernde Nebenprodukte betrachtet, da sie spezifische Anwendungen bieten und somit dem ganzheitlichen Ansatz entsprechen.

Die bei der mechanochemischen Behandlung von LAS- oder Petalit-Proben anfallenden Auslaugungsrückstände wiesen vergleichbar hohe spezifische Oberflächen auf und bestanden hauptsächlich aus Sodalith und/oder LTN-Zeolithen, die für ihre besonderen Eigenschaften bei der Molekularsiebung oder selektiven Adsorption bekannt sind. Dementsprechend wurden diese Nebenprodukte in einer Nebenstudie als potenzielle Adsorbens untersucht und zeigten eine hervorragende Sorptionsleistung für zweiwertige Schwermetallionen in synthetischen Abwasserproben.

1 Introduction

1.1 Motivation and Concept

Lithium, discovered around 200 years ago by the Swedish chemist Johan August Arfwedson [1], has recently experienced a renaissance as it plays a central role in the transition from combustion engines to electric mobility, by combining a remarkably low atomic weight with the highest electrochemical potential of all alkali metals [2,3]. Driven by current trends in Lithium-ion battery (LIB) technology, which currently consumes about 80 % of global lithium production, this element is in demand as never before, leading to 21 % increase in global output to 130,000 t in 2022 [4]. In parallel, record prices for spodumene ore (α-$LiAlSi_2O_6$) and for both lithium carbonate (Li_2CO_3) and lithium hydroxide (LiOH), the key compounds for LIB manufacturing, have been achieved recently [4]. Consequently, many efforts are being made nowadays to maintain lithium supply through the exploitation of primary deposits around the world, while recovery from secondary sources is almost non-existent [5,6].
Considering the crucial role of lithium in LIB and other future technologies, demand is expected to further increase in the upcoming years; hence recycling and recovery of lithium from end-of-life products will be mandatory to meet future requests [7,8]. In addition to discarded batteries, end-of-life Lithium-Alumina-Silica glass-ceramics (LAS, Li_2O-Al_2O_3-SiO_2) should also be considered as a promising and previously untapped secondary raw material for lithium recovery, as their lithium content of about 2-3 wt% can compete with currently mined hard rock ores. Due to its low coefficient of thermal expansion, this type of glass-ceramic is particularly used as stove tops for kitchen ranges, resulting in a promising waste stream with an estimated volume of up to 900,000 discarded appliances per year in Germany [9–11]. Until now, large amounts of valuable lithium have been lost through this disposal route, mainly as the recycling of waste electrical devices focuses only on the recovery of transition metals, while glass-ceramics are generally neglected.
On the other hand, the processing of primary lithium ores, including the minerals lepidolite, α-spodumene and petalite, poses challenges due to their low reactivity and poor leachability, requiring intensive pretreatments to convert them into a more reactive state in which the lithium ions are more available to the extraction reagent [12–14]. To overcome this drawback, energy intense high-temperature calcination is widely used, resulting in a phase transformation to tetragonal β-spodumene, which is much more susceptible to leaching owing to its more open structure [13,15,16]. However, mechanical activation through ball milling of spodumene or lepidolite in air and aqueous media has also been considered as an alternative to thermal pretreatment, leading to an increase in specific surface area, a reduction in particle and crystallite sizes, and the formation of amorphous phases, generally advantageous conditions for the achievement of high leaching rates [14,15,17–19]. Moreover, present state of industrial technology does not include holistic approaches and focuses only on the low but economically relevant lithium content, while omitting the main constituents Al and Si, resulting in large amounts of residues during sulfuric acid leaching [12,20]. These circumstances encouraged several authors to explore approaches without any thermal phase transformation, which are using the entire inventory of lithium minerals via decomposition of silicates at alkaline conditions typically at high pressures in autoclaves, leading to the formation of zeolites, while lithium enriches simultaneously in the solution [21,22].
Inspired by these findings, a new route for lithium extraction by simultaneously zeolite synthesis without thermal pretreatments was proposed and investigated in the present work, which combines mechanical activation with alkaline decomposition via mechanochemical treatment of lithium silicates using moderate sodium hydroxide concentrations, thus avoiding autoclaving. In the first section of this study, the focus was set on the Li recycling out of LAS glass-ceramics by alkaline mechanochemistry [23], while in the second part, the

experimental findings were transferred to the three most important naturally occurring lithium minerals lepidolite, spodumene, and petalite [24]. Upon mechanochemical treatment, several hydrometallurgical stages are mandatory to obtain a pure lithium compound, while special attention has been paid to holistic approaches, in which each byproduct has its specific area of application.

1.2 Objectives

Mechanochemistry, known as a versatile method for various applications, was used in this work for lithium extraction in parallel to synthesis of zeolites using various feedstocks such as discarded LAS glass-ceramics as well as lithium silicate minerals e.g., lepidolite, spodumene and petalite shown in Figure 1-1.

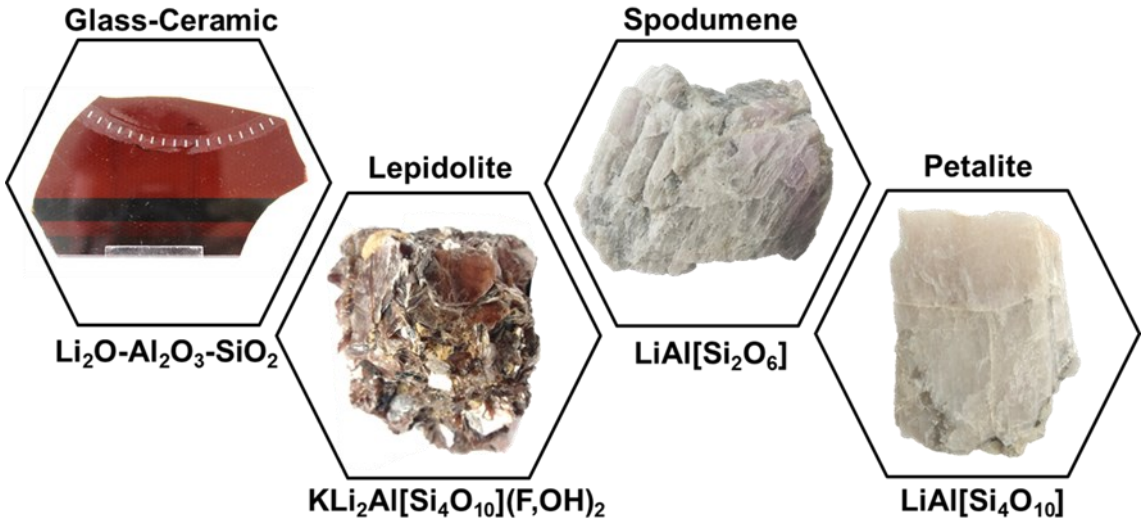

Figure 1-1. *Investigated lithium sources including end-of-life LAS glass-ceramic and primary lithium silicate minerals such as lepidolite, spodumene and petalite.*

So far, the few preceding studies investigated either mechanical activation combined with acid leaching or alkaline leaching under high pressure in autoclaves on mineral samples, while lithium recovery from glass-ceramics is only scarcely reported in literature. Therefore, a novel route was investigated in this work by combining the approaches of mechanical activation with alkaline leaching by performing alkaline mechanochemistry on various lithium source materials using a laboratory-size planetary ball mill. The present study is structured in two sections, the first of which comprises an experimental feasibility study on the holistic recycling of glass-ceramics, in which various parameters were investigated to address the following fundamental questions:

- How do experimental parameters such as NaOH concentration, experimental time, ball-to-powder ratio and rotational speed influence the lithium extraction during alkaline mechanochemistry?
- How do these parameters affect zeolite formation and which types of zeolites are generated under specific experimental conditions such as different NaOH concentrations?

- How much accompanying elements such as Al and Si pass into solution alongside the targeted lithium during alkaline leaching, and which hydrometallurgical steps are required to purify the solution before precipitation of a pure lithium compound?

However, in the second part, the results from the experiments with glass ceramics were extended to lithium silicate minerals, where the following additional questions emerged:

- How are the experimental results from LAS samples transferable to the lithium minerals?
- How do the position of lithium sites and the different crystal structures of lithium silicate minerals play a role during mechanochemical processing?
- How do the formed zeolites compare to the types produced when a LAS glass-ceramic is used as a precursor?
- How do the hydrometallurgical steps, including purification of the solution and precipitation of a lithium compound, differ from the treatment in the first part?

In order to address the questions raised, a range of analytical methods were selected to characterize different types of samples taken along the chosen processing route from the starting material to the final lithium compound. Therefore, inductively coupled plasma optical emission spectrometry (ICP-OES) was chosen to evaluate chemical changes during the various hydrometallurgical steps, while powder X-ray diffraction (PXRD) was applied to obtain structural data for phase analysis of solid samples. Moreover, these measurements were combined with complementary methods such as Fourier transform infrared spectroscopy (FT-IR), N_2 adsorption/desorption, scanning electron microscopy (SEM), and transmission electron microscopy (TEM) to assess the changes in molecular bonding, specific surface area, morphology, or microstructures, respectively. Finally, additional experiments have been required to evaluate the adsorption behavior of selected zeolite samples and to investigate their potential as adsorbents for the removal of heavy metal ions from aqueous solutions.

2 Fundamentals

2.1 Mechanochemistry

2.1.1 Definitions

Although the origin of mechanochemistry dates back to ancient times, the term was first introduced into the systematics of chemistry by Ostwald in 1887 [25], while the actual definition was formulated by Heinecke in 1984 [26] as follows: "*Mechanochemistry is the branch of chemistry concerned with the chemical and physical transformations of solids under the action of mechanical influences*." Likewise, the IUPAC Compendium of Chemical Terminology [27] has chosen a similar term, defining mechanochemistry as a "*chemical reaction initiated by mechanical energy*." In contrast, the term mechanical activation defined by Butyagin [28] as an "*increase in reactivity due to stable changes in the solid-state structure*" is commonly applied when mechanical energy is used to change physicochemical properties of samples without a direct chemical reaction being involved. Thereby, the enhancement of reactivity is mainly attributed to the accumulation of defects, including partly amorphization of crystal structures and the formation of metastable polymorphs due to mechanical forces [29], as illustrated in Figure 2-1.

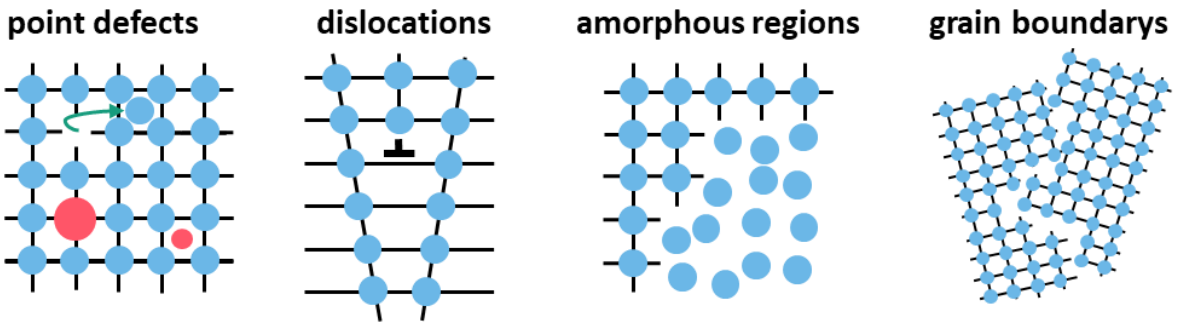

***Figure 2-1**. Reported defects in mechanical activated crystalline solids including point defects (Frenkel and Schottky defects), dislocations, amorphous regions and grain boundaries. Redrawn from [29].*

In particular, this mechanical activation is also involved in mechanochemistry, but frequently precedes the underlying reaction and has no further influence on it [29]. Complementarily, tribochemistry is often referred to a special branch of mechanochemistry, dealing with the chemical behavior of solids by mechanical action on their interfaces. Although the term is used synonymously with the more general terminology of mechanochemistry [26,30].

2.1.2 Historical Background

Already in ancient times, people recognized that grinding of solids not only lead to smaller particles, but can also cause changes in materials leading to the first mechanochemical experiments [31]. Among the most prominent examples was the Greek philosopher and natural scientist Theophrastos of Eresos, who as early as 315 B.C. revealed in his book "De Lapidibus" (On Stones) the reaction of cinnabar (HgS) to elemental mercury when it

was rubbed together with vinegar in a copper mortar according to equation (1), which is considered as the first mechanochemical reaction and the first documented isolation of an element from its ore [25,31–33]. Recent investigations have confirmed that this reaction also proceeds under dry or aqueous conditions, whereby acetic acid is attributed a catalytic role, presumably through the removal of passivation sites on metal surfaces [33].

$$HgS + 2\,Cu \rightarrow Hg + Cu_2S \quad (1)$$

At the end of the 19th century, the first systematic mechanochemical experiments were attributed to the American Matthew Carey Lea, who investigated the influence of different forms of energy on silver halides [34]. In his studies, Lea subjected AgCl and AgBr particles to mechanical stresses such as simple pressure or shear and recorded their decomposition via the formation of elemental silver and the release of chlorine (Cl_2) or bromine (Br_2), contrary to heating, which leads to a melt of the entire compound without any further decomposition phenomena [25,34]. However, in the heydays of chemistry in the 20th century, mechanochemistry was only little represented since wet chemical processes were much more established, which changed rapidly at the turn of the millennium, when mechanochemistry experienced a veritable renaissance [31]. One of the main reasons for this trend is the growing environmental awareness and the emergence of "green chemistry" by Anastas and Warner [35], which have strengthened the concept of mechanochemistry, in particular by enabling solvent-free synthesis and the achievement of a higher product selectivity during synthesis [31,36].

2.1.3 Theoretical Background

Contrary to classical chemical routes, which have been researched in detail for decades, mechanisms taking place in mechanochemical reactors are still largely in the dark, since massive metal or ceramic vessels hinder in-situ observation of the reactions. Consequently, relatively little is known about the processes that are occurring during the reaction, which has led to various theories being proposed in the past. [31].
As early as the 1950s, the so-called hot-spot theory was postulated by Bowden, Yoffe and Tabor [37,38], which assumes temperatures of over 1000 K for a fraction of a second during the collision of milling balls, which can provide the required activation energy for mechanochemical reactions. Even though such high temperatures have already been theoretical assumed to occur at crack tips in single crystals [39], this theory is considered controversial nowadays [25,31]. Little later, in 1960s, Thiessen et al. [40] postulated a more comprehensive explanation for mechanochemical reactions via the magma-plasma model (see Figure 2-2).

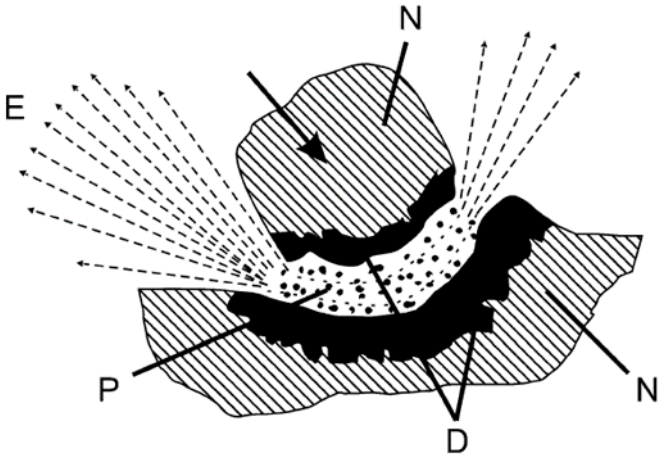

Figure 2-2. *Schematic drawing of the magma-plasma model for mechanochemical reactions after Thiessen et. al [40], where (E) represents excited electrons, (N) the non-deformed solid, (D) the deformed surface layer and (P) the triboplasm. Image reproduced from [31].*

This approach is based on the release of very high energies at surfaces at the time of collision, which lead to the formation of a triboplasm characterized both by the emission of excited particles and by temperatures of 10,000 K, thereby enabling short-lived reactions. Since Maxwell's velocity distribution of the particles cannot occur due to the short lifetime of the plasm, mechanochemical reactions can take different pathways than their wet-chemical counterparts [26,31].
In particular, new analytical developments that emerged recently, including in-situ Raman spectroscopy and in-situ XRD methods, have provided detailed insights into mechanochemical reactors, leading to the establishment of the pseudo-fluid model, revealing the direct influence of the grinding speed and the temperature of the grinding bowls on the reaction rate in conjunction with the Arrhenius equation [31]. As illustrated by the schematical drawing in Figure 2-3, the milling balls primarily support the intensive intermixing of the powders as a kind of fluid in the mill at high accelerations speeds, while each collision with the sample leads to new reactive surfaces and the removal of resulting product layers at surfaces, whereby diffusion problems become secondary in consequence [31,41].

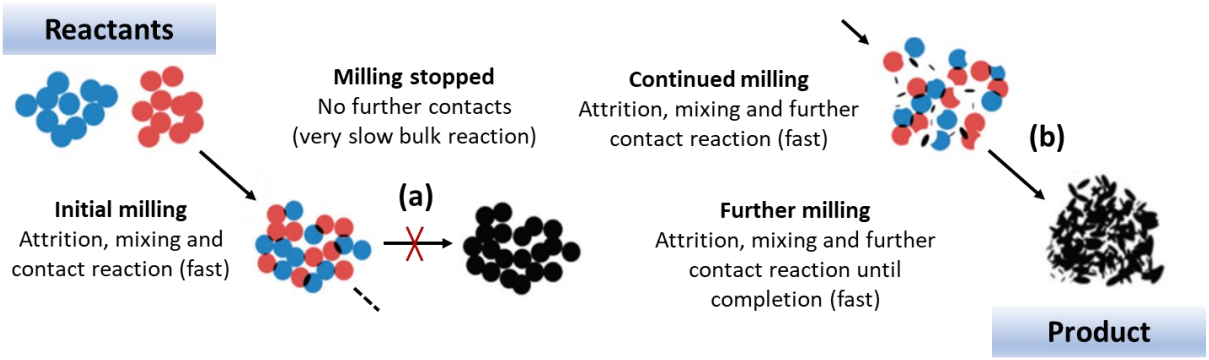

Figure 2-3. *Pseudo-fluid model for mechanochemical reactions, where the blue and red spheres represent reactant particles, which were converted to a product (black) while milling. Thereby the contact reaction occurring between reactants is fast but self-limiting due to the formation of a product layer at the interface (a). Therefore, continuous milling is required for entire transformation of the reactants to the product phase (b). Figure reproduced from [41].*

2.1.4 Mechanochemical Reactors

In general, mills of different shapes and sizes are being used as mechanochemical reactors, which are further diversified both in their mode of operation and in the forces acting on the material to be ground, such as impact, friction or shear. Suitable types of mills can be divided into two groups depending on the grinding media used, with representative examples shown in Figure 2-4. On the one hand, there are mills with freely movable grinding media such as ball mills, planetary ball mills or vibration mills (see Figure 2-4 (a) to (c)), usually applying grinding balls of medium to high densities and a good abrasion resistance, which are inserted into the grinding chamber together with the material to be processed. In contrast, pin or roller mills (see Figure 2-4 (e) and (f)) are based on fixed integrated tools such as rotors, knives or screws. In addition, attritor mills (see Figure 2-4 (d)) are a mixture of both types, as they combine integrated tools with free-moving grinding media [31]. For the purpose of this work, a planetary ball mill was employed, which derive its name from the planetary movement of the grinding vessels on a so-called sun wheel. Besides the rotation of the vessels around an inner axis, there is also a counter-rotation around an outer axis, leading to the superposition of two centrifugal fields, which causes the intense stressing of the sample material, since the grinding balls roll along the vessel wall. Whenever the milling

balls collide with each other or the balls hit the container wall, impact energy is transferred to the sample material, whereby the amount of energy mainly depends on the mass and speed of the accelerated milling balls.

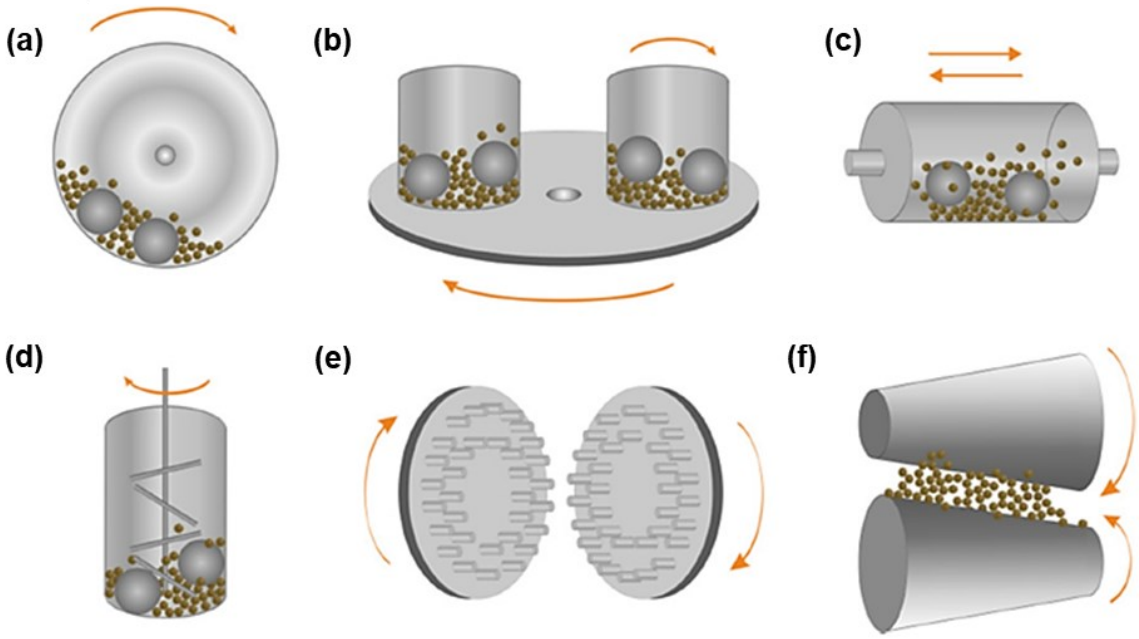

Figure 2-4. *Schematical drawings of different mill types, capable for mechanochemical treatments, including (a) ball mill, (b) planetary ball mill, (c) vibration mill, (d) attritor mill (also known as stirring ball mill), (e) pin mill and (f) roller mill. Image reproduced from [42].*

Thereby, the milling leads to the comminution of particles, the generation of new surfaces and partly amorphous samples, involving various comminution mechanisms such as impact, friction and shear, mainly depending on the angle of impact (see Figure 2-5). As a rule, centrifugal forces occur in planetary ball mills that are 50-100 times higher than the acceleration due to gravity, which leads to an energy input that is up to 1000 times higher compared to vibration or drum mills and thus significantly shortens the reaction time and enables mechanochemical reactions requiring a high energy input [31].

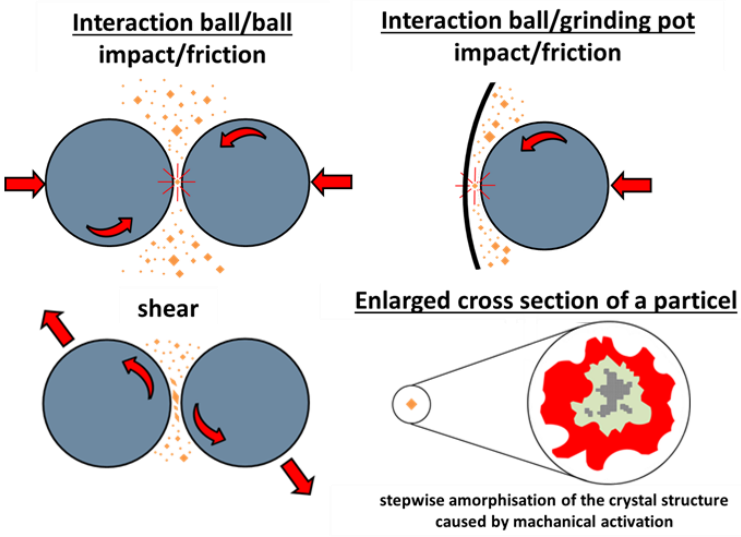

Figure 2-5. *Schematic showing the comminution mechanisms occurring in planetary ball mills including impact, friction and shear scenarios. Besides the comminution of particles, partly amorphous samples were observed during mechanical activation experiments. Own work, reproduced from [43].*

2.1.5 Applications

The use of mechanochemistry and/or mechanical activation has already demonstrated its high efficiency in various scientific and industrial syntheses, including inorganic materials such as alloys, oxides, halides, sulfides, nitrides or composites, in addition to cocrystals, pharmaceuticals, organic compounds, metal complexes or organometallic frameworks [31,44,45]. Moreover, mechanochemistry offers great potential for solving environmental challenges such as the remediation of pollution, waste management or the recycling of various materials [46–48]. Of particular relevance for this work is the application of mechanochemistry and mechanical activation in the context of metal recovery from primary and secondary resources, as these approaches are known to significantly enhance the reactivity of refractory phases as part of hydrometallurgical processes [47,49,50]. This phenomenon was first associated by Zelikman et al. [51] with the disruption of chemical bonds in crystalline materials during ball milling, which consequently lowers the activation energy and thus support the metal extraction process according to equation (2) and (3) [52].

$$\Delta E^* = E - E^* \tag{2}$$

$$k^* = k \exp(\Delta E^*/RT) \tag{3}$$

Here, the apparent activation energy is represented by E for the ordered phase and E^* for the disordered phase after milling, while k and k^*represent the rate constants of leaching of the parent phase and disordered phase, in addition to R and T, which represent the gas constant and reaction temperature, respectively [52]. For the case of $E^* > E$, the terms $\exp(\Delta E^*/RT) > 1$ and $k^* > k$ result; therefore, leaching of the activated phase is expected to be significantly higher, when compared to the starting material [52].

In consequence, mechanochemical treatments are typically applied to improve leaching kinetics of ore minerals such as chalcopyrite ($CuFeS_2$), tetrahedrite ($Cu_{12}Sb_4S_{13}$), wolframite ($(Fe,Mn)WO_4$), or scheelite ($Ca(WO_4)$), which are characterized by having high activation energies, surface controlled leaching mechanisms and are consequently challenging to leach [50,53]. Overcoming this drawback requires harsh leaching conditions including autoclaving at temperatures of up to 240 °C, or alternatively increasing the reactivity via mechanochemical treatments, thus enabling leaching at lower temperatures and under atmospheric pressure conditions due to the smaller particle size and larger surface area of the sample [50]. In addition to the transition-metal ores already described, also lithium minerals are affected by these drawbacks, which is why mechanical activation prior to leaching is being discussed as an alternative pre-treatment by various authors (see chapter 2.3.3).

Besides the various applications mentioned above, mechanochemistry also contribute to the synthesis or modification of zeolites, a class of microporous materials, typically aluminosilicates, characterized by a three-dimensional framework structure, a large surface area, a uniform pore size distribution and a relatively high chemical and thermal resistance [54–57]. So far, the hydrothermal route has been the most frequently utilized method for zeolite synthesis for decades, requiring a distinctive combination of experimental parameters such as high temperature, pressure, long reaction time, appropriate aqueous medium, compatible structuring agent and suitable starting materials to produce a high-purity product [58]. In the meantime, mechanochemistry emerged as a complementary method for improved solvent-free and template-free synthesis, leading to the successfully preparation of zeolites with various frameworks including industrial relevant species such as ZSM-5 (MFI, Pentasil group), zeolite Y (Faujasite framework) or zeolite A (LTA) [58–64]. One of the main advantages of this route is the pre-synthesis step including mechanical activation and intimate mixing of the aluminosilicate

precursors, leading to increased kinetics during subsequent calcination, which in addition increases the crystallinity of the zeolite and further converts remaining starting materials into the product phase [58]. In terms of chemical and physical properties, the zeolites synthesized via mechanochemistry showed similar properties to hydrothermally grown ones. Therefore, this methodology seems to be promising for large-scale production as it allows significant savings in raw materials, energy and costs, providing a new gateway for zeolite applications [63]. In addition, mechanochemical processes are also employed in zeolite technology for post-synthetic treatments such as the incorporation of heteroatoms or the modification of structural properties such as crystallinity, surface area and porosity, which typically serve to improve catalytic performance [58].

2.2 The Alkali Metal Lithium

2.2.1 History and Discovery

The lithium minerals petalite and spodumene were first described in 1800 by Jose de Andrada from an iron ore deposit on the island of Utö near Stockholm, Sweden [65], without much being known about their chemical composition. Further studies on these minerals were carried out by the Swedish chemist Johan August Arfwedson, an associate of the famous chemist Jöns Jakob Berzelius, who first discovered an unknown alkali metal in 1817 by determining the chemical composition of petalite $LiAl[Si_4O_{10}]$ [1,66]. Since the occurrence of the new element was limited to rock-forming minerals, Berzelius named it lithium in reference to the ancient Greek word *líthos* for rock [1]. In 1818, just one year after his discovery, Sir Humphrey Davy succeeded in producing small amounts of metallic lithium by electrolysis of molten Li_2CO_3, while larger-scale production was first achieved in 1855 by Robert W. Bunsen and Augustus Matthiessen by electrolysis of a lithium chloride (LiCl) melt [67,68]. As early as 1819, Christian Gottlob Gmelin synthesized various lithium compounds and recognized the characteristic bright red flame of lithium for the first time [2,69,70]. Exactly 100 years after the discovery of lithium, Wilhelm Schlenk published in 1917 his results about the synthesis of the first organolithium compounds methyllithium (CH_3Li), ethyllithium (C_2H_5Li) and phenyllithium (C_6H_5Li) from the corresponding organic mercury compounds [2,71]. For a long time, there was little interest in lithium and its compounds, which changed after World War I, when lithium was needed as a hardener for lead alloys (railroad metals), which were mainly used for bearings [68,72]. This development was the reason for the first commercial production of Li_2CO_3 and lithium metal, which was started in 1923 by the Deutsche Metallgesellschaft in the Hans-Heinrich smelter in Langelsheim in the Harz Mountains, Germany, on the basis of the domestic mineral Zinnwaldite ($K(Li,Fe^{2+},Al)_3[(F,OH)_2AlSi_3O_{10}]$) [68]. Between the two world wars, demand for lithium was still modest, as it was mainly used as a lubricant (lithium stearate) and in the glass industry in form of Li_2CO_3. This changed abruptly in 1954, when the U.S. Atomic Energy Commission needed large quantities of lithium hydroxide (LiOH) to produce tritium out of the ^6Li nuclide for their nuclear weapons program [72]. Subsequently, intensive mining and production took place, especially in the U.S., until capacity exceeded demand and several plants were shut down in the 1960s [72]. Since these days, lithium and its compounds have a wide range of industrial applications, which will be further discussed in chapter 2.4.

2.2.2 Lithium Chemistry

Lithium with the symbol Li and the atomic number 3 belongs to the group of alkali metals in the periodic table of elements. Natural lithium occurs in the form of the two isotopes ^{6}Li (7.5%) or ^{7}Li (92.5%) and it is the lightest of all solid elements under standard conditions due to its low density of 0.534 g/cm^3. Moreover, lithium metal crystallizes in the cubic space group *Im-3m* (space group number 229) with the lattice parameter a = 3.51 Å and two formula units per unit cell and forms a soft, silvery-white metal that tarnishes quickly in moist air, while forming lithium hydroxide and lithium nitride (Li_3N). In the group of alkali metals, lithium has the highest melting point (180.75 °C), the highest boiling point (1341.85 °C) and the highest specific heat capacity (3.482 J/(gK)). In the periodic table, it has the lowest normal potential (E_0 = -3.045 V), after which it can be classified as the least noble of all elements. This is also the reason why metallic lithium can only be obtained by electrolysis of molten salts, typically LiCl. Similar to all other alkali metals, lithium is also a chemically extremely reactive, which reacts with all gases, with the only exception of the noble gases, with all main group elements as well as with a number of subgroup elements as summarized in Figure 2-6.

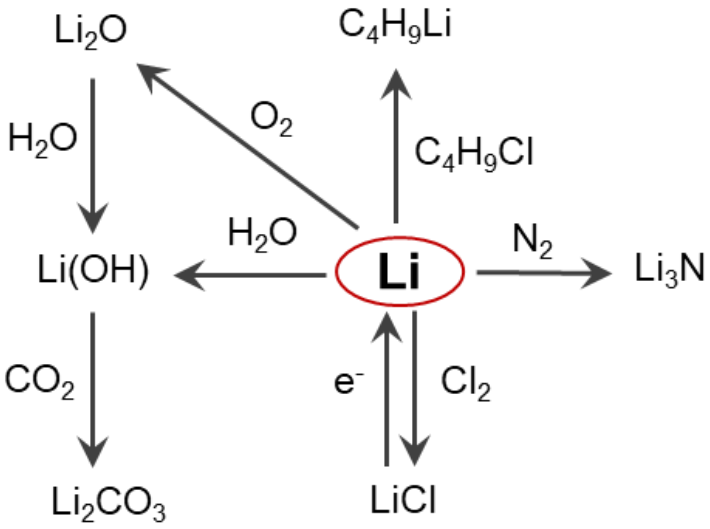

Figure 2-6. *Summary of the most important reactions of lithium. Please note, there was no consideration of the stoichiometry and the exact reaction conditions. Image Redrawn from https://commons.wikimedia.org /wiki /File: Lithium _reactions.svg*

Concerning its compounds with more electronegative bonding partners (e.g., LiH, LiF, Li_2O), lithium occurs in the oxidation state +I, which is a consequence its electron configuration [He] 2s1 with only one outer electron [65]. Within the periodic table, a diagonal relationship between lithium and magnesium exists, which can be attributed to the similar charge-radius ratios of Li^+ (1 : 0:60 = 1:7), Mg^{2+} (2 : 0:65 = 3:1), versus Na^+ (1 : 0:95 = 1:0). Although the diagonal Li/Mg relationship is not as pronounced as for the pairs Be/Al or B/Si, several properties of lithium are more similar to magnesium than to sodium. A prominent example of this relationship, which also plays a role in lithium extraction and refining, are the solubilities of the lithium salts, which often differ significantly from those of the sodium salts and rather resemble those of the magnesium salts. For example, LiOH, Li_2CO_3 and Li_3PO_4 are only partially dissolvable in water in contrast to NaOH, Na_2CO_3 and Na_3PO_4, in analogy to $Mg(OH)_2$, $MgCO_3$ and $Mg_3(PO_4)_2$ [67].

Within this chapter, the large field of organic lithium compounds has been neglected, as they are not of relevance for this work. For more in-depth information on inorganic and organic lithium compounds please see the textbook by Hollemann and Wiberg [67].

2.2.3 Lithium Minerals and Deposits

According to Goldschmidt's geochemical classification of elements, lithium can be classified as lithophilic due to its predominant occurrence in the earth crust [73,74]. Since the average content of lithium in crustal rocks is estimated to be about 0.006 % [75], it ranks with elements such as copper, zinc, and lead in terms of scarcity. Unlike these heavy metals, lithium is rarely enriched and is instead widely distributed in low concentrations in numerous igneous rocks [67]. Consequently, commercially viable lithium deposits are sparse and occur only in certain geological environments such as salt brines, specific sedimentary rocks or granitic pegmatites [5,75,76], as exemplarily shown in Figure 2-7.

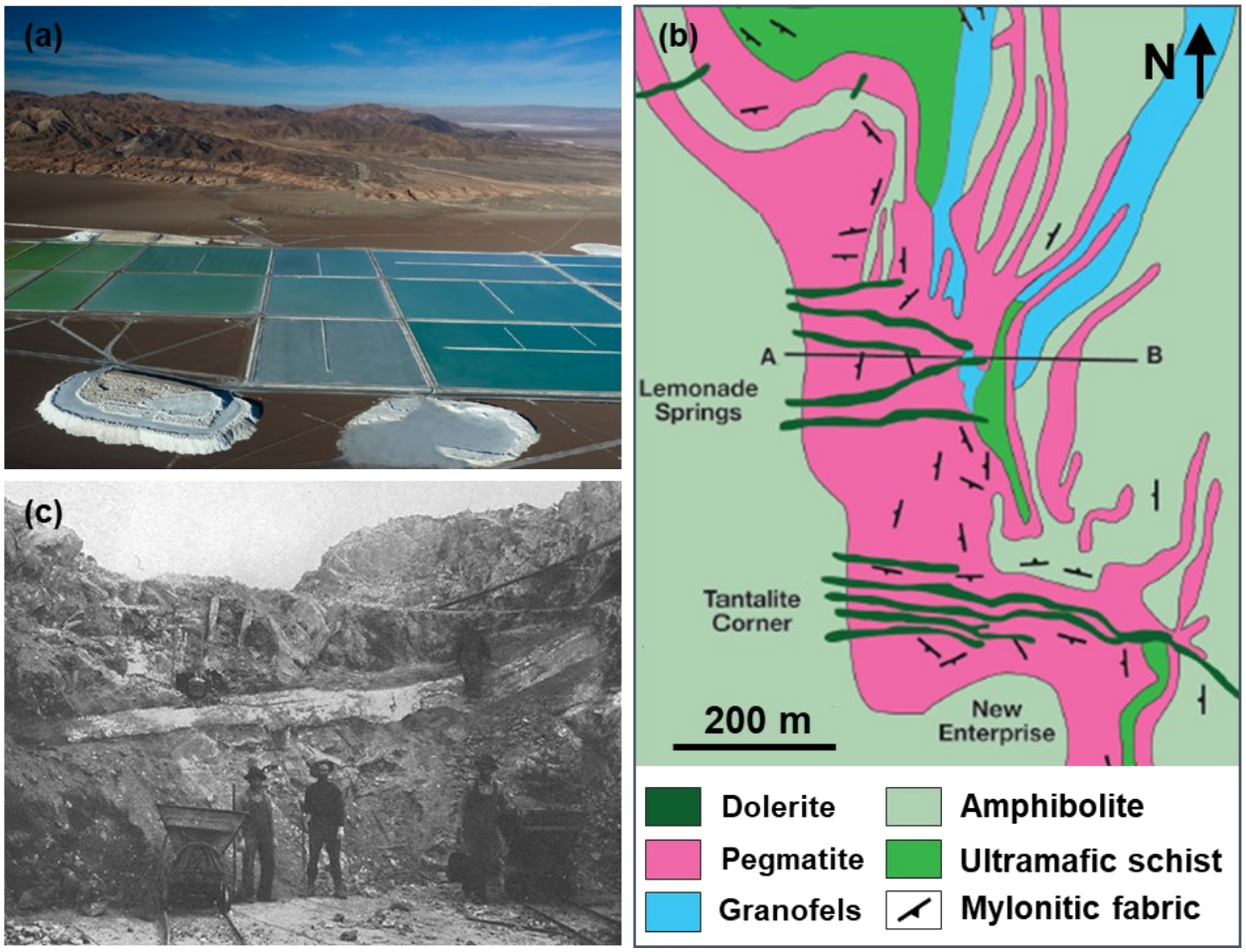

Figure 2-7. *Relevant examples of worldwide lithium deposits and operations; (a) reveals evaporation ponds of a lithium brine operation in the Salar de Atacama, Chile, (b) represents a geological map of the Greenbushes pegmatite deposit in Western Australia with predominant tin, tantalum and lithium mineralization, while (c) shows an enormous spodumene crystal of up to 14 m in length and 82 t in weight, which was mined as lithium ore at the renowned Etta Mine in the Black Hills of South Dakota, U.S. at the beginning of the 20th century. Figures adapted and slightly modified from [77–79].*

Lithium-bearing salt brine deposits are geologically related to sedimentary basins containing lacustrine evaporites formed during dry periods with low precipitation and high evaporation rates. Compared to marine evaporites, lacustrine evaporites and their associated brines generally have a much broader range of chemical compositions and are frequently enriched in lithium. However, the geogenic source of the lithium enriched in these brines remains controversial, although weathering of felsic volcanic rocks or geothermal activity

associated with nearby volcanoes or magma bodies are among the most common possibilities [5,76]. Most of these brine deposits are located in the South American lithium triangle along the borders of Chile, Bolivia and Argentina, including the well-known Salar de Uyuni and Salar de Atacama (see Figure 2-7 (a)) with enormous estimated lithium resources of 10.2 and 6.3 Mt, respectively [5,76]. Additionally, there are brine deposits of much smaller size on the Qinghai-Tibet Plateau in China, including the Qaidam Lakes with predominant magnesium sulfate mineralization and the Zabuye Lake with carbonate-rich brines, which is the typical location for the mineral zabuyelite, the naturally occurring form of Li_2CO_3. Crucial economic factors for the extraction of lithium from brines are not only the absolute lithium content, but also the amount of impurities such as magnesium and sulfate, which in turn impede conventional processing routes. Recently, geothermal brines became another promising source, especially since the generation of steam in the power plant increases the concentration of dissolved components such as lithium in wastewater, which allows its recovery as a valuable byproduct through various adsorption techniques [5,80,81].

Up to now, the International Mineralogical Association has recognized 112 valid mineral species containing essential Li in their respective stoichiometries [74]. Regarding the systematics of minerals, which classifies minerals according to their chemical composition, most of them belong to the group of silicates (82 species), while the class of phosphates is in the second place (16). In addition, Lithium-containing halides (4), oxides (5), carbonates (4), and sulfates (1) also occur in nature, but not abundantly. Since most of these minerals are rather rare and/or occur only in small quantities, only a limited amount of them is of economic interest, in particular, silicates and some phosphates as can be summarized in Table 2-1.

Table 2-1. *Most important lithium-bearing minerals including their chemical composition and theoretical lithium content [75,79]. The three minerals highlighted in blue will be discussed in more detail throughout the text. For better comparison with the own analysis data, the lithium content of each mineral was additionally converted into lithium oxide values.*

Mineral	Chemical Formular	Li-Content [wt%]	Li_2O-Content [wt%]
Amblygonite	$LiAlFPO_4$	3.73	8.04
Bikitaite	$LiAlSi_2O_6 \cdot H_2O$	3.28	7.07
Hectorite	$Na_{0.3}(Mg,Li)_3Si_4O_{10}(F,OH)_2$	0.56	1.20
Jardarite	$LiNaSiB_3O_7(OH)$	3.39	7.30
Lepidolite	**$K(Li,Al)_3(Si,Al)_4O_{10}(F,OH)_2$**	**3.56**	**7.67**
Petalite	**$LiAlSi_4O_{10}$**	**2.27**	**4.89**
Spodumene	**$LiAlSi_2O_6$**	**3.73**	**8.04**
Triphylite	$LiFe[PO_4]$	4.40	9.48
Zabuyelite	Li_2CO_3	18.79	40.49
Zinnwaldite	$K(Li,Fe^{2+},Al)_3[(F,OH)_2AlSi_3O_{10}]$	1.70	3.66

From the geological point of view, only few of them are related to sedimentary rocks, such as hectorite ($Na_{0.3}(Mg,Li)_3Si_4O_{10}(OH)_2$), a trioctahedral member of the smectite group [72,82], or jardarite ($LiNaSiB_3O_7(OH)$), a rare mineral occurring only in the unique combined lithium-boron deposit of Jardar in central Serbia [5,75]. However, the predominant majority of economically important lithium minerals are enriched in granitic pegmatites and accessory rocks, as a result of the special properties of lithium [75].In particular due to its small

size, it is incompatible with the common rock-forming minerals during magmatic differentiation [83,84]. Therefore, it remains in the liquid phase for a long time and crystallizes typically at the very end in residual melts [75,84], such as Lithium-Cesium-Tantalum (LCT) pegmatites. Moreover, the formation of lithium aluminosilicate phases during crystallization of a residual melt is mainly controlled by temperature and pressure, as shown in the corresponding phase diagram for quartz-saturated conditions (see Figure 2-8) [84,85].

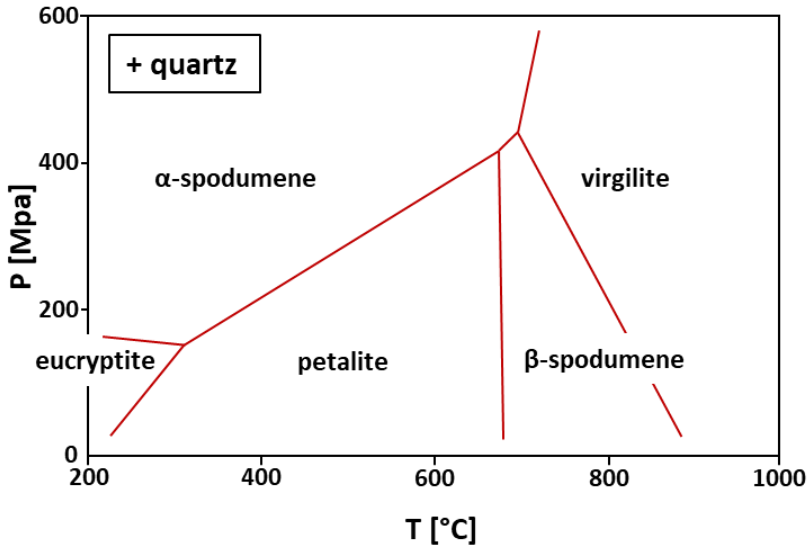

Figure 2-8. *Pressure-temperature phase diagram for lithium aluminosilicates under quartz-saturated conditions, occurring in LCT-type pegmatites. Redrawn from [84].*

Accordingly, α-spodumene is more stable than petalite at higher pressure, while eucryptite exists only in a narrow pT range at low pressures and temperatures [84,85]. In addition to these phases, β-spodumene and virgilite [86], a solid solution between β-quartz and γ-spodumene, occur as high-temperature phases under conditions rarely reached during the formation of common magmatic rocks. In addition to the lithium-bearing minerals, these LCT-type pegmatites are usually enriched in other valuable elements such as beryllium, niobium, tin or rubidium [5,75,82], which in turn enable lithium hard-rock mining in an economic way.

By far the most significant deposit of this type, with estimated lithium resources of 0.85 Mt Li, is the 2.57 Ga old Greenbushes pegmatite in Western Australia (see Figure 2-7 (b)), with predominant Li-Sn-Ta mineralization and spodumene as the main ore mineral [5]. Other significant resources are located in the U.S., such as the Kings Mountain pegmatite belt, which runs along the border between North and South Carolina and includes the Bessemer City deposit (0.42 Mt Li) and the Kings Mountain deposit (0.32 Mt Li), where in both deposits spodumene is the source of lithium [5]. In addition to lithium, the latter deposit is particularly important from a mineralogical perspective, as it is well known for its phosphate mineralization, being the type locality for several rare species such as kingsmountite ($Ca_3MnFeAl_4(PO_4)_6(OH)_4{\cdot}12H_2O$) or footemineite ($Ca_2Mn^{2+}Mn^{2+}{}_2Mn^{2+}{}_2Be_4(PO_4)_6(OH)_4{\cdot}6H_2O$) [5,74]. Another U.S. locality with only historic lithium production is the Etta Mine in the Black Hills of South Dakota, known for the world's largest spodumene crystals, up to 14 m long and 82 t in weight (see Figure 2-7 (c)), which occurred in the extremely coarse-grained inner zone of the pegmatite body [5,87].

Although pegmatite deposits are often much smaller than brine deposits in terms of size and total estimated resources, they remain of particular interest due to their generally higher lithium content and wider geographic distribution, which consequently carries lower geopolitical risks [5]. For more details on the major lithium deposits worldwide, see Kesler et al. 2012 and the literature cited there [5].

2.2.4 Investigated Lithium Minerals

In the following section some further mineralogical details on the lithium silicates lepidolite, spodumene and petalite are presented, which were investigated in this work with respect to lithium extraction and zeolite synthesis. General physical and optical properties of these minerals are summarized in Table 2-2, while their idealized crystal structures are depicted on the unite cell level in Figure 4-21.

Table 2-2. *Selected physical and optical properties of investigated lithium minerals [88–90]. Highlighted in blue are the Mohs hardness and the coordination of the lithium, which are of particular importance for wear of the milling balls and the lithium extraction during the mechanical-chemical treatments.*

	Lepidolite	**Spodumene**	**Petalite**
Mohs hardness	2.5 - 3.5	6.5 - 7.5	6.0-6.5
Color	light purple to pink	colorless, gray-white	Colorless, gray-white
Streak color	white	grey-white	white
Density [g/cm^3]	2.84	3.184	2.4
Refractive Indices nα	1.530	1.648 - 1.661	1.504
Refractive Indices nβ	1.551 - 1.556	1.655 - 1.670	1.510
Refractive Indices nγ	1.555 - 1.559	1.662 - 1.679	1.516
Birefringence δ	0.025 - 0.029	0.014 - 0.018	0.012
Coordination of Li	6	6	4

Lepidolite is a commonly used term to denote unspecified light-colored Li-rich trioctahedral micas of the polylithionite-trilithionite series ranging in composition between $KLi_2Al(Si_4O_{10})(F,OH)_2$ and $K(Li_{1.5}Al_{1.5})(AlSi_3O_{10})(F,OH)_2$ [88]. Members of this series generally have monoclinic symmetry, but there are several polytypes with slightly different cell parameters such as Polylithionite-1M (space group *C*2), Polylithionite-2M2 (space group *C*2/*c*) or Trilithionite-2M2 (space group *C*2/*c*) [88]. In addition to lithium, lepidolite is often enriched in rubidium, which can be recovered as a valuable byproduct [21]. Also noteworthy is Zinnwaldite, another lithium-bearing mica group mineral, which in turn belongs to a series between siderophyllite ($KFe^{2+}{}_2Al(Al_2Si_2O_{10})(OH)_2$) and polylithionite [88]. From an economic point of view, this dark mica is a less attractive source of lithium due to the high iron and fluorine content combined with the relatively low Li content in the ores [75]. Based on its crystal structure (see Figure 4-21 (a)) Lepidolite is a typical phyllosilicate based on a three-layer structure consisting of a sandwich-like alternating sequence of tetrahedral layer - octahedral layer - tetrahedral layer [73]. While to achieve charge balance between these sequences large K+ cations are required to saturate the layers [73]. As a consequence of its small ionic radius Li^+ does not sit on these interstitial sites, but instead replaces the Al^{3+} in the octahedral layers [73]. The relatively strong bonding forces of Si-O (and Al-O) within a tetrahedral layer and the tight bonding to the octahedral layer explain the perfect cleavage along the {001} basal plane between the layer packages, which is a characteristic feature of almost all phyllosilicates [73].

Spodumene $LiAl[Si_2O_6]$, an inosilicate of the pyroxene group, crystallizes in the monoclinic space group *C*2/*c* with lattice parameters a = 9.46 Å; b = 8.39 Å; c = 5.22 Å and β = 110.17 ° and four formula units per unit cell [73,89]. The mineral has a Mohs hardness of 6,5 - 7, a gray-white streak color and is typically colorless or gray-white. In addition to this most common modification, gem-quality spodumene also occurs in yellow (triphan), light to emerald green (hiddenite), and pink to purple (kunzite) varieties [73,89]. The crystal structure of spodumene (see Figure 4-21 (b)) consists of parallel chains of $[SiO_4]$-tetrahedra and $[AlO_6]$-octahedra, both running in the direction of the c-axis and are connected by corners, while Li^+ cations fill the gaps in the structure [73]. Spodumene exhibits perfect cleavages along the (110) and (1-10) planes parallel to the chains, intersecting at an angle of 87 °, which is a characteristic feature of the entire pyroxene group [73]. In nature only the monoclinic α-polymorph occurs, while β-spodumene with tetragonal space group $P4_32_12$ or γ-spodumene with hexagonal space group $P6_222$ exist only under synthetic conditions, for example, after calcination of the α-phase at high temperatures [13].

Petalite $LiAl(Si_4O_{10})$, crystallizes with a = 11.74 Å; b = 5.17 Å; c = 7.63 Å and β = 112.54° with two formula units per unit cell in the monoclinic space group *P*2/*b* [90]. The mineral is typically colorless to gray, has a white streak and a Mohs hardness of 6.5. In addition to its use as a source of lithium, gem-quality petalite, occurring only in a few select deposits, is turned into jewelry [90]. Petalite's crystal structure (see Figure 4-21 (c)) is composed of a three-dimensional framework of TO_4 tetrahedra (with T = Li; Al or Si) interconnected by corners sharing one oxygen, which is typical for tectosilicates [91]. On the other hand, petalite can also be considered as a phyllosilicate due to the perfect arrangement of cations at certain crystallographic sites represented by folded $[Si_4O_{10}]$-layers perpendicular to (001), which are connected by LiO_4 and AlO_4 tetrahedra [91]. Regarding the crystal structure of petalite, the tetrahedral coordination of Al^{3+} and Li^+ is particularly noteworthy [92,93], which distinguishes petalite from lepidolite and spodumene, where these ions are present in octahedral coordination. When petalite is heated to temperatures of about 1100 °C, it forms an isomorphous solid solution series between SiO_2 and the high-temperature modifications of spodumene, while the presence of tetragonal (β-spodumene) and/or hexagonal (γ-spodumene) phase was also observed [68,72]. From the physical properties, the perfect cleavage perpendicular to (001) and parallel to the $[Si_4O_{10}]$-layers is most remarkable, which also gave this mineral its name based on the Greek word “petalon” for leaf [90].

2.3 Lithium Extraction of Primary and Secondary Sources

2.3.1 Lithium Resources and Reserves

In recent years, demand for lithium has been remarkably high, driven by current advancements in electromobility, leading to a 21 % increase in global production from 107,000 t in 2021 to 130,000 t in 2022 besides all-time record prices for spodumene ore (6% lithium oxide content; US$ 5,800/t) and for the most common compounds Li_2CO_3 (US$ 67,000/t) and LiOH (US$ 78,000/t) in November 2022 [4]. At this point it is noteworthy that this steadily increasing demand for lithium is actually being met by the production of a limited number of countries such as Australia (61,000 t), Chile (39,000 t), China (19,000 t), Argentina (6200 t) and Brazil (2200 t), which are in fact responsible for the majority of global mine production in 2022 [4], as shown in Figure 2-9. In terms of deposit type, current operations in Australia and Brazil are based exclusively on mineral ores, while large brine facilities are located in Chile and Argentina; contrary to China, which benefits from both types [4]. In addition, smaller operations located in Canada, Portugal, or Zimbabwe also contributed to global lithium production through mining and processing of pegmatite ores. Besides the current mine production of about 130,000 t for the year 2022, additional reserves of about 26 Mt were calculated for the above-mentioned countries, while ongoing exploration identified additional global lithium resources of about 98 Mt [4].

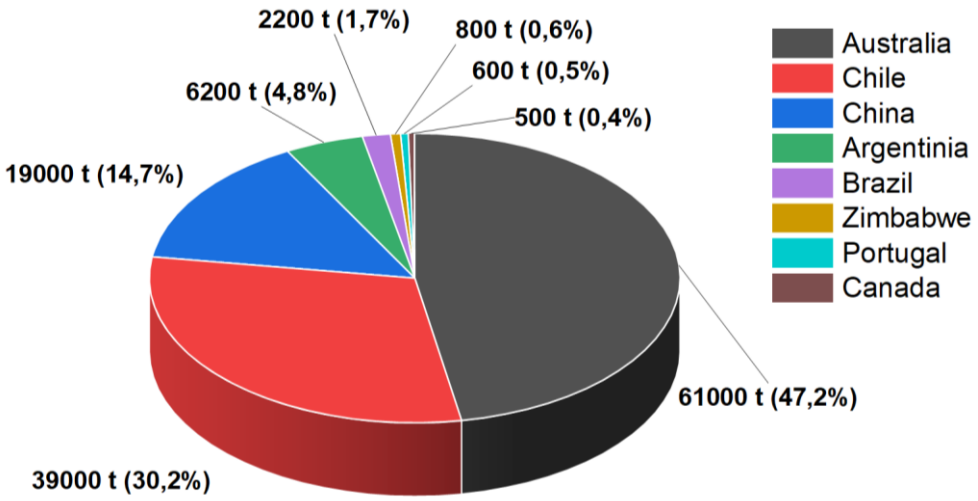

Figure 2-9. *Global mine production in t of lithium for 2022, sorted by country. Own figure, data derived from [4].*

2.3.2 Processing of Lithium Brines

Since the chemical composition of the recovered brines varies in certain ranges, downstream steps to the final lithium intermediate differ from deposit to deposit. In these processes, the amount of impurities, such as Mg, K, Na, SO_4, and the technical effort required to produce a lithium product of adequate purity were identified as the main cost drivers, hence brines with low Mg/Li and low SO_4/Li are most preferable [75].
From the series of various routes, the way of the Rockwood Lithium, established for the brines of the renown Salar de Atacama deposits located in Chile, has been selected as a representative example, which involves concentration and subsequent evaporation in large on-site ponds [75]. The aim of this first processing step is the removal of interfering components such as carbonates, sulfates and potassium and magnesium chlorides by fractional crystallization, while at the same time the lithium content from an initial 0.15 % is enriched to about

6 % [75,76]. One of the major advantages of this step is the favorable geographical location of the deposit in the Atacama Desert, which allows the use of solar energy for evaporation in place [75,76]. On the other hand, the prolonged time of up to 18 months for evaporation is considered as a disadvantage [75], especially when compared to the much faster processing routes applied for lithium mineral ores. Subsequent purification procedures include removal of boron by solvent extraction, precipitation of magnesium and sulfate ions by treatment with Calcium oxide (CaO), followed by a slight addition of Sodium carbonate (Na_2CO_3) to ensure the separation of the last residues of Mg and Ca [75,76]. During these purification steps, a mixture of various precipitates is generated, including $MgCO_3$, $Mg(OH)_2$, $CaSO_4$, and $CaCO_3$, which are classified as tailings since they do not meet the actual requirements for further use [75]. After removal of all impurities, lithium carbonate can be precipitated by adding Na_2CO_3 at elevated temperature [75,76]. For an in-depth survey of lithium brine processing, reference is made to the work of Garret [76] and Schmidt [75], from which the remarks summarized above are derived.

2.3.3 Beneficiation and Pretreatment of Hard Rock Ores

Prior to lithium extraction, the mined raw ores (e.g. pegmatites) require several processing steps involving sorting, crushing, gravity separation, magnetic separation, flotation, washing and drying to become lithium-bearing concentrates [75]. However, the main beneficiation methods are dense media separation and flotation, taking advantage of the differences in specific gravity or chemical and physical properties observed between the lithium minerals and the accompanying gangue minerals [94]. Depending on the quality, these concentrates are divided into a "technical grade" with a higher level of purity (e.g. low iron content) for direct use in the glass or ceramics industry and a less pure "chemical grade" for the production of lithium compounds [75]. However, downstream processing of these concentrates, which contain minerals such as lepidolite, α-spodumene and petalite, presents some inherent difficulties, such as their low reactivity, which generally results in poor leachability, requiring either thermal treatments with or without further additions of chemicals or leaching with harsh chemicals to overcome this drawback.

Therefore, calcination via conventional heating at about 1000 °C is by far the most common pretreatment during processing of lithium ores, converting the densely packed monoclinic α-spodumene with a specific gravity of 3.15 g/cm^3 into the more open tetragonal β-spodumene with a specific gravity of only 2.4 g/cm^3, which is consequently much more susceptible to leaching, in particular compared to the α-polymorph [13]. Similar results were obtained for petalite, where calcination at about 1100 °C led to the formation of β-spodumene in the presence of a SiO_2 phase, thus dramatically increasing leachability [72,95].

Since pretreatment by conventional heating requires large quantities of energy and contributes significantly to the cost and environmental impact of lithium extraction, microwave heating and mechanical activation are also under consideration as potentially less energy-intensive alternatives [15]. In general, microwave-assisted heating is known to provide faster and more energy-efficient heat transfer because only the sample inside the furnace is selectively heated, while the peripheral region remains unheated [15]. However, since spodumene, as many other silicates, does not absorb microwave energy, the experimental setup requires a suitable design with special crucibles made of silicon carbide to ensure rapid heat transfer, which is known as hybrid microwave heating. Nevertheless, these heating experiments led to promising results such as the almost complete conversion of α- to β-spodumene after 170 s at a final sample temperature of 1197 °C. [15,16].

In addition to thermal processes, mechanical activation including ball milling in air and aqueous media has been identified as a further applicable technique for enhancing the reactivity of refractory lithium minerals by modifying their physiochemical properties [15]. It has been observed that mechanical activation leads to an

increase in specific surface area, a decrease in particle and crystallite sizes, together with the formation of amorphous phases, which are generally favorable preconditions for higher reactivity associated with metal leaching [15]. In this context, Gasalla et al. [19], investigated the mechanical activation of α-spodumene in air with the aid of a vibratory disc mill and reported an immediate reduction in particle size from 370 to 15 µm after 30 min of grinding, while simultaneously the specific surface area measured by BET analysis increased significantly from a not measurable surface for the initial sample to 8 m^2/g after milling. Supplementary to the decreasing particle sizes, XRD analyses of the activated spodumene samples additionally confirmed a decrease in crystallite size due to partial amorphization upon prolonged milling from an initial value of 0.2 µm to 360 Å (5 min) and to 200 Å (10 min), while further milling did not contribute to a further decrease [19]. In another study by Kotsupalo et al. [18] α-spodumene was mechanically activated in water rather than in air, resulting in fewer structural changes, while specific surface area measurements gave a significantly higher value of 213 m^2/g, compared with 6 or 8 m^2/g [19] obtained under dry media milling conditions. In consequence of activation in aqueous medium for 30 min, the α-spodumene structure became amorphous, while lithium and aluminum were partially leached into the activation medium [18]. Moreover, Vieceli et al. [14,17] investigated mechanical activation as a pretreatment of lepidolite by dry grinding in a steel disk mill prior to sulfuric acid digestion. Specifically, they report on an entire amorphization of the lepidolite structure by 30 min of milling, resulting in promising extraction yield of > 90 % [17]. However, the same authors generalized their approach to several other lithium ores such as spodumene, petalite, lithiophilite-triphylite ($LiMn^{2+}PO_4$ to $LiFe^{2+}PO_4$) and amblygonite-montebrasite ($LiAlPO_4F$ to $LiAlPO_4OH$), confirming their previous findings [96].
Although hybrid microwave heating and mechanical activation of lithium ores appear to be promising pretreatment methods for more efficient lithium extraction, they still need to be optimized and scaled up to industrial-scales to allow economic comparison with the state-of-the-art processing (e.g., calcination) [15].

2.3.4 Lithium Extraction of Hard Rock Ores

Over the last decades, various approaches for lithium extraction from hard rock ores have been investigated, which are briefly summarized in Table 2-3 and described in more detail below, whereby reference is made to the cited literature for in-depth information.

Table 2-3. *Methods reported in the literature for Li extraction from hard rock ores, including the most relevant reagents required, which are discussed in the following subsections [12,97]. The abbreviation sc stands for super critical.*

Reported Routes	Major Reagents
Acidic Treatment	H_2SO_4 / HF / H_2SO_4 + HF / CaF + H_2SO_4
Alkaline Treatment	NaOH / NaOH + CaO / CaO / $Ca(OH)_2$ / KOH
Sulfate Roasting or Autoclaving	K_2SO_4 / Na_2SO_4 / $FeSO_4$ / $CaSO_4$
Carbonate Roasting or Autoclaving	Na_2CO_3 / $CaCO_3$
Chlorination Roasting	Cl_2 / $CaCl_2$ / NH_4Cl / NaCl
Direct Carbonation	sc-CO_2

Acidic Routes

Acidic treatments are mostly predominant in lithium industry, which include the roasting of β-spodumene with concentrated sulfuric acid (H_2SO_4) at temperatures of about 250 °C as the most prominent one, resulting in an ion exchange within the structure (Li^+ vs. H^+) and the formation of solid lithium sulfate (Li_2SO_4) according to equation (4) [98,99]. Further downstream processes involve water leaching (equation (5)) to transfer metal sulphates into the liquid water phase, while separating lithium from the residue consisting mainly of H^+-exchanged β-spodumene ($HAlSi_2O_6$). Following equation (6), finally Li_2CO_3 is precipitated through the addition of Na_2CO_3 to the enriched solution, while receiving sodium sulfate (Na_2SO_4) as a byproduct. Besides β-spodumene, the sulfuric acid approach can be extended to other lithium minerals such as calcined petalite [95] or lepidolite without prior thermal treatment [12]. In addition, it is also suitable for the recovery of lithium from mechanically activated α-spodumene and lepidolite samples with significantly higher yields and lower acid consumption when compared to samples without this type of physiochemical treatment [14,17,18,96]. Apart from the relatively high energy consumption for calcination and acid roasting, the formation of relatively large amounts of Na_2SO_4 during precipitation is regarded as a disadvantage, since the market for this compound is already oversaturated, as it arises during several industrial processes as a byproduct [12].

$$2\,\beta - LiAlSi_2O_{6\,(s)} + H_2SO_4\,(conc.) \rightarrow 2\,HAlSi_2O_{6\,(s)} + Li_2SO_{4\,(s)} \quad (4)$$

$$Li_2SO_{4\,(s)} \rightarrow Li_2SO_{4\,(aq)} \quad (5)$$

$$Li_2SO_{4\,(aq)} + Na_2CO_{3\,(aq)} \rightarrow Li_2CO_{3\,(s)} + Na_2SO_{4\,(aq)} \quad (6)$$

In particular, the high energy consumption during the thermal treatments including calcination and/or roasting is considered as a serious drawback during processing of spodumene, which has encouraged several authors to develop direct acidic leaching processes [12]. Owing to its unique property to decompose silicates, hydrofluoric acid (HF) is in particular applied during sample digestion for analytical purposes, but is also considered as agent for lithium extraction out of mineral ores [12]. In general, there are different approaches for this purpose, using HF only [100], a mixture of HF and H_2SO_4 [101], or a combination of H_2SO_4 and solid fluorite (CaF) for the in-situ production of HF [99,102]. With respect to lithium extraction all these methods gave promising results as HF decomposes silicates reliably (exemplarily shown in equation (7) using HF only) and requiring only moderate temperatures of 75-100 °C [100,101]. Therefore, the use of HF indicating a certain advantage on the energy consumption when compared to the standard H_2SO_4 method, which necessitates 250 °C [12].
On the other hand, there are some major drawbacks associated with HF-based leaching processes, such as significant safety issues, environmental and disposal problems [12] due to the production of large amounts of F-containing waste, including mixed fluoride salts (Na_3AlF_6/Na_2SiF_6) occurring as byproduct during purification of the solution (see equation (8)) [100] and residues of hexafluorosilicic acid (H_2SiF_6) [101]. Since in-situ generation of HF following equation (9) lowers safety requirements and thus avoiding direct use of HF [12], it is considered to be the most promising approach, culminating in the development of the SiLeach© process, which has already proven its effectiveness for various low-grade ores at pilot scale level [102].

$$\beta - LiAlSi_2O_{6\,(s)} + 19\,HF_{(aq)} \rightarrow LiF_{(aq)} + H_3AlF_{6\,(aq)} + 2\,H_2SiF_{6\,(aq)} + 6\,H_2O \quad (7)$$

$$H_3AlF_{6\,(aq)} + H_2SiF_{6\,(aq)} + 5\,NaOH_{(aq)} \rightarrow Na_3AlF_{6\,(s)} + Na_2SiF_{6\,(s)} + 5\,H_2O \quad (8)$$

$$CaF_{2\,(s)} + H_2SO_{4\,(aq)} \rightarrow 2\,HF_{(aq)} + CaSO_{4\,(aq)} \quad (9)$$

Alkaline Routes

In contrast, decomposition of silicates are also achievable in the presence of alkalis such as NaOH, which was investigated by several authors in the context of direct lithium extraction out of α-spodumene [22,103], lepidolite [21] or petalite [104] via hydrothermal high-pressure autoclaving without any thermal pretreatment. These approaches differ slightly in detail, but in general the highest leaching rates of more than 90 % were obtained at temperatures of about 250 °C, using strongly alkaline conditions achieved at 400 to 760 g/L NaOH, sometimes with additional CaO to improve leachability [21,22,103,104]. Recently, it was reported on a novel two-step process in which α-spodumene is decomposed to Li_2SiO_3 and $KAlSiO_4$ by alkaline treatment with a 50 wt% KOH solution at 250 °C in the first step (see equation (10), followed by acidic (H_2SO_4) leaching, thereby decomposing Li_2SiO_3 and transferring Li into solution, while $KAlSiO_4$ remains in the residue for further applications [97].

$$3\,\alpha - LiAlSi_2O_{6\,(s)} + 3\,K^+ + 6\,OH^- \rightarrow Li_2SiO_{3\,(s)} + 3\,KAlSiO_{4\,(s)} + 2\,H_2SiO_{4\,(l)}^{2-} + Li^+ + H_2O \quad (10)$$

Besides high extraction yields, the alkaline treatment enables, contrary to all other approaches, the generation of value-added byproducts, such as hydrosodalite zeolites [21,22] or a zeolite precursor such as $KAlSiO_4$ [97], thus utilizing the entire inventory of source minerals, which consist mainly of Al and Si. In particular, these holistic approaches would be able to mitigate large amounts of solid waste, considering that sulfuric acid leaching of spodumene currently generates about 8 to 10 t of leaching residues per ton of Li_2CO_3 [12,20]. Worth mentioning is that sodium zeolites such as hydrosodalites, with the general formula $Na_{6+x}[Al_6Si_6O_{24}](OH)_x{\cdot}nH_2O$, generated as byproducts in alkaline routes, are known for their special properties as molecular sieves or selective adsorbers, which render them suitable for various potential applications including the removal of hazardous substance from aqueous solutions or as a membrane material for H_2/CH_4 separation or the production of ultrapure water [54,56,105,106]. However, among many advantages, the high caustic consumption (e.g. 760 g/L NaOH) associated with these routes is still considered critically for economic and technical reasons [12].

Sulphate and Carbonate Roasting or Autoclaving

Owing to the high reactivity of sulfates or carbonates at high temperatures and/or pressures, these compounds can be used to promote lithium extraction during roasting or autoclaving of lithium ores. In this context sulfate roasting involves the reaction of spodumene or lepidolite with various sulfates such as K_2SO_4, Na_2SO_4, $FeSO_4$, or $CaSO_4$ at high temperatures of 850-1000 °C, thereby generating water-soluble Li_2SO_4, which can be extracted and further processed to Li_2CO_3 via the addition of Na_2CO_3 to the leaching liquor (see equation (6)) [12]. Moreover, sulfate roasting of lepidolite also has the potential to recover K, Rb, and Cs, which can be separated to produce value-added byproducts [107]. Besides the solid-solid reactions Kuang et al. [108] reported on an autoclaving process for hydrothermal extraction while also using Na_2SO_4 with the addition of CaO, delivering a high yield at much lower temperature of 230 °C and a pressure of about 1.7 MPa.
In addition, roasting with carbonates such as Na_2CO_3 or $CaCO_3$ at high temperatures is also reported for both spodumene and lepidolite and proceeds analogous to the sulfate method, involving an ion exchange between

Li^+ and the metal ion (e.g., Na^+ or Ca^{2+}) provided by the added carbonate or sulfate [12]. Exemplary equation (11) illustrates the reaction of β-spodumene with Na_2CO_3 leading to the formation of Li_2CO_3 in addition to analcime ($Na[AlSi_2O_6]\cdot H_2O$) as a mineral phase, which can be achieved through solid-solid reaction during roasting at 450-750 °C [109] or hydrothermally by autoclaving at about 225 °C [110]. Further developed on this autoclaving route were done by Tiihonen et al. [111] by adding a conversion leaching step to directly transfer the synthesized Li_2CO_3 to battery-grade LiOH with the aid of $Ca(OH)_2$ according to equation (12).

$$2\,\beta - LiAlSi_2O_{6\,(s)} + Na_2CO_{3\,(s)} + 2\,H_2O \rightarrow Li_2CO_{3\,(s)} + 2\,Na(AlSi_2O_6) * H_2O_{(s)} \quad (11)$$

$$Li_2CO_{3\,(s)} + Ca(OH)_{2\,(s)} \rightarrow 2\,LiOH_{(aq)} + CaCO_{3\,(s)} \quad (12)$$

Chlorination Roasting

High-temperature chlorination roasting of α- and β-spodumene and lepidolite has been established by several authors as an effective route for lithium recovery, attributable to the high reactivity of chlorine and its strong affinity towards the formation of lithium chloride (LiCl), which can be easily separated via water leaching from the residues [12]. Therefore, equation (13) is exemplarily shown, indicating the reaction of β-spodumene with Cl_2 gas at 1100°C resulting in the formation of LiCl, while the silicious compound are represented by the high-temperature phases mullite ($Al_6Si_2O_{13}$) and cristobalite (SiO_2) [112].

$$12\,\beta - LiAlSi_2O_{6\,(s)} + 6\,Cl_{2\,(g)} \rightarrow 3\,O_{2\,(g)} + 12\,LiCl_{(l)} + 2\,Al_6Si_2O_{13\,(s)} + 20\,SiO_{2\,(s)} \quad (13)$$

In addition to chlorine gas, various salts such as calcium chloride ($CaCl_2$), ammonium chloride (NH_4Cl), or sodium chloride (NaCl), decomposing at high temperatures, have also been shown to be appropriate chlorinating agents in several experimental studies leading to high recovery rates [12]. However, chlorination of β-spodumene using solid $CaCl_2$ [113] generally benefits from the lower process temperatures of 900 °C compared to 1100 °C when using gaseous Cl_2 [114], which exhibit a much higher safety risk as it is both more toxic and corrosive [12]. Furthermore, an economically feasible method was reported by Yan et al. [115] in which lepidolite can be treated with a NaCl/CaCl mixture at 880 °C, effectively recovering both the intended lithium and accompanying elements such as K, Rb, and Cs with a high yield.

Direct Carbonation Approach

This process was initially developed for the extraction of lithium from calcined zinnwaldite ores, while little later it was also applied to the most common lithium minerals such as spodumene, lepidolite and petalite as well as the black mass from LIB recycling [116–119].

Similar to other routes, lithium minerals require a pretreatment such as calcination, leading in the case of zinnwaldite to the formation of β-spodumene, leucite and iron-rich phases such as magnetite or hematite after a treatment 950 °C for 3 h. Following this route, leaching involves the use of super critical CO_2 in water (sc-CO_2/H_2O) at 10 MPa and 230 °C for 3 h in an autoclave filled with an aqueous suspension of fine milled zinnwaldite ore (d_{50} particle size = 18 µm) at liquid to solid ratio of 100. As a result of this experimental setup, up to 75 % of Li were transferred under optimal conditions into the liquid phase as soluble lithium bicarbonate ($LiHCO_3$), while reaching an elemental content of approximately 100 mg/L. Therefore, further downstream processing steps, focusing on the enrichment of lithium via dual digestion and the use of electrodialysis with

special cation exchange membranes, resulted in enriched and purified solutions with about 8500 mg/L Li. These solutions can be directly used for precipitation via heating at 90 °C, leading to a release of CO_2 and the formation of Li_2CO_3 in a product grade of 99.0 %. In general, the direct carbonation route benefits from high selectivity in leaching, low consumption of chemicals (only CO_2), relatively high purity of the product and the reuse of leach residues in geopolymers, although details on phase composition are lacking. However, with the respect to the use of Zinnwaldite with its low Li and high Fe and F content, the energy-intensive calcination, the fine grinding required and the enrichment steps associated with this route are regarded critically for economic and technical reasons [12,116–119].

2.3.5 Lithium Recovery of LAS Glass-Ceramics

Besides the variety of different routes which have been investigated for primary lithium minerals, there are only a comparatively limited number of studies in the literature on lithium recovery from glass-ceramics, applying roasting routes or classical leaching approaches [120–122]. In this context, roasting with the addition of CaO and $CaCl_2$ at 1000 °C was performed by Kim et al. [120] to produce water-soluble LiCl, resulting in a rate of 90 % at optimal parameters during water leaching at 100 °C. A similar approach was adopted by Lee et al. [121], where the glass-ceramic powder was first calcined at 1000 °C without additives to increase reactivity. The samples were then mixed with CaO, while subsequent water leaching at 100 °C partially transferred lithium into the solution via an ion exchange mechanism (Ca^{2+} vs. 2 Li^{+}). This process required a second calcination at 600 °C and an additional leaching step to recover a total amount of 99.9 % of the lithium, while the leaching residues were claimed to have applications in the cement industry [121].
In contrast to roasting processes at high temperatures, direct leaching is also achievable via alkaline hydrometallurgical processes, whereby the efficiency generally depends on the NaOH concentration, the specific surface area and the reaction temperature. According to Lee [122], who investigated this route, about 70 % of the lithium was leached into solution at optimum parameters such as 12 h reaction time, 2 mol/L NaOH, 53 µm particle size, 1:10 solid/liquid ratio, 250 rpm stirring speed and 100 °C reaction temperature. However, a rather uncommon phenomenon was observed when the leaching experiment was extended from 12 to 48 h, resulting in a significant decrease in the Li concentration in the leach liquor from 1160 to 236 mg/L. More specifically, this observation required further XRD analysis, which were supplemented by SEM-EDS examinations on particle cross-sections. According to this investigation, the lithium loss was attributable to the formation of zeolite P shells around unreacted LAS particles, which on the one side hinder further lithium extraction and on the other side lead to a partial adsorption of already extracted Li^{+} ions [122]. From an economic and technical point of view, the comparatively low extraction rate of 70 % after 12 h of stirring in conjunction with the required fine grinding prior to leaching and the incomplete conversion of the feedstock must be discussed critically before further implementation of this route.

2.4 Applications of Lithium and its Compounds

2.4.1 Overview of the Industrial Applications

Nowadays, lithium and its compounds are used in a variety of ways in industry due to their specific properties, making this element a sought-after resource [3,7]. Figure 2-10 therefore summarizes the most common applications for lithium compounds in 2022, based on estimates of global end-use markets, revealing that most lithium has been consumed for the production of batteries (80 %) [4]. In contrast to the high lithium consumption for LIB (described in more detail in chapter 2.4.2), classical applications such as ceramics and glasses (7 %), lubricating greases (4 %), mold flux powders (2 %), air treatment (1 %) or pharmaceutical applications (1 %) are less important [4]. The use of lithium in ceramics and glasses, which is the second important application, dates back to Otto Schott, who discovered the beneficial role of lithium oxide (Li_2O) in glass melting as early as 1879 [2]. Therefore, Li_2CO_3 is commonly used, which decomposes into Li_2O and carbon dioxide (CO_2) at high temperatures, resulting in a lower melting point, lower viscosity and, above all, lower thermal expansion [2]. In addition, lithium is frequently adopted as a flux in the fabrication of glazes and ceramic products such as tiles, sanitary ware or tableware [75]. Especially in the production of glazes or enamels, the addition of lithium reduces the viscosity of the glaze while increasing the gloss, luminosity, chemical resistance and abrasion resistance of the finished ware [75]. In addition, the use of lithium compounds is of significant importance for the manufacturing of LAS glass-ceramics with a low thermal expansion coefficient close to zero [2,75], which will be discussed in more detail in section 2.4.3. In the field of ceramics and glasses Li_2CO_3 is mainly used, while the direct use of natural minerals such as spodumene or petalite is generally possible, if they reach a high degree of purity and have negligible iron content [75].

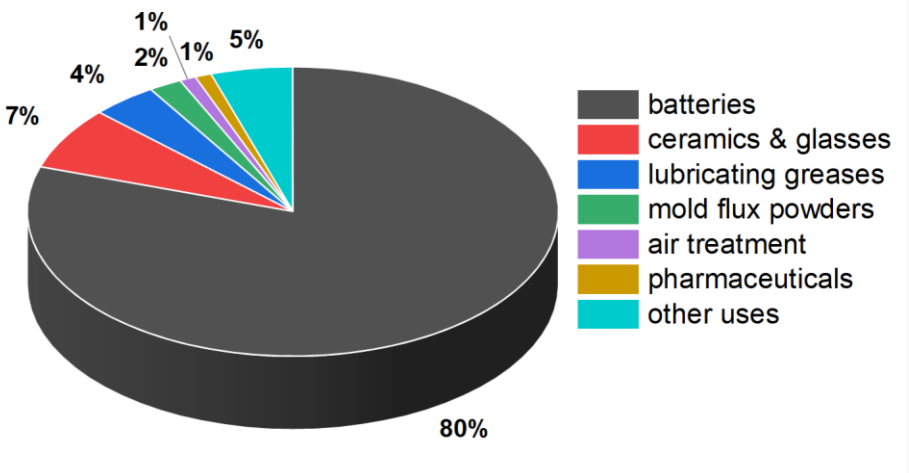

Figure 2-10. *Estimates of the global end-use markets for lithium compounds in 2022. Own work, data derived from [4].*

Lithium, sodium or aluminum salts of fatty acids are required to thicken mineral oil during the production of lubricating greases. For this purpose lithium stearate, synthesized from stearic acid and lithium hydroxide monohydrate ($LiOH \cdot H_2O$), is commonly adopted, giving the grease a high dropping point of about 180 °C and low water solubility, which prevents the washout under humid conditions [2,75]. Due to these excellent properties, lithium greases are widely used in harsh environments where high speeds and heavy mechanical loads occur, such as mining operations, paper machines, automobiles, aircraft or ships [2,75].

Moreover, lithium containing fluxes are required in the steel casting industry to optimize the process, to minimize the risk of defective goods and to prevent the formation of imperfections in the finished castings [75]. Therefore, fluxes containing up to 5 % lithium oxide are demanded, which can be added either as Li_2O or Li_2CO_3, while the addition of spodumene or petalite is also possible [75].

The application of lithium in air treatment salts includes various applications, such as lithium bromide (LiBr) solutions used in refrigeration systems, highly hydroscopic LiCl in dehumidifiers, and anhydrous lithium hydroxide (LiOH) for the removal of CO_2 of enclosed environments, such as submarines or space capsules [2,75]. For the latter application in particular, LiOH is preferable to all other alkali metal salts because it is much lighter and, consequently, the average amount of CO_2 of about 1.0 kg a human releases per day under normal conditions can be absorbed by 1.1 kg of LiOH through the formation of Li_2CO_3 [2,75].
In addition to the more technical applications already mentioned, lithium compounds such as carbonates, citrates, sulfates, acetates or aspartates also have pharmaceutical uses, dating back to the Australian psychiatrist John Cade, who discovered in 1949 their curative effect in the treatment of manic-depressive disorders [2,76]. Therefore, lithium supplements are used in abundance today, although the cause of the curative effect of the lithium cation is still debated and different hypotheses need to be proven [2].

2.4.2 Lithium-Ion Batteries (LIB)

In recent years, a trend towards the extensive production of LIB is emerging, which can be explained in the context of the transition from combustion to electric mobility, in which these batteries play an essential role as they combine the comparatively low atomic weight of lithium with the highest electrochemical potential of all alkali metals [2,3]. Since this type of battery revolutionizes energy storage technology by having an enormous impact on our society, the researchers John B. Goodenough, M. Stanley Whittingham and Akira Yoshino have been awarded the Nobel Prize in Chemistry in 2019 for their fundamental work on this topic [123]. In particular, their breakthrough developments led to the release of the first commercially available LIB in 1991 consisting of a petroleum coke-based anode, a $Li_{1-x}CoO_2$ cathode, along with an anhydrous electrolyte composed of lithium hexafluorophosphate ($LiPF_6$) in propylene carbonate [123]. Since its introduction to the market, the basic design of LIB has remained unchanged and consists of the main components shown in Figure 2-11.

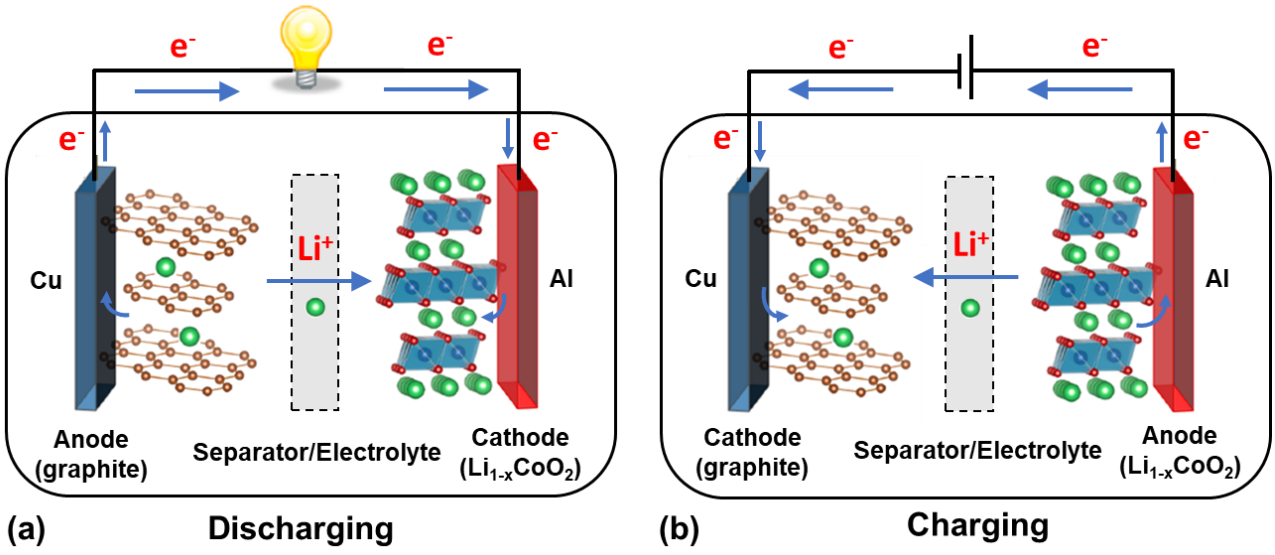

Figure 2-11. *Schematic drawing of a conventional LIB cell during discharging (a) and charging (b), while illustrating the most relevant components including anode, cathode, separator, electrolyte and collector foils. Figure adapted and slightly modified from Goodenough & Park [124].*

These include the positive electrode, often referred to as the "cathode", and the negative electrode, known as the "anode". However, these terms for the electrodes only reflect the reality when the battery is being

discharged; on charging, it is reverse and the positive electrode acts as the anode and the negative electrode as the cathode [125]. As can be clearly seen in the scheme, both electrodes are separated by a microporous separator but are electrochemically connected via an ion-conductive electrolyte, which consists of a lithium salt solution typically based on $LiPF_6$, in a mixture of organic solvents. Benefitting from its layered structure of alternating cobalt- and lithium-rich sheets, lithium cobalt oxide ($LiCoO_2$, LCO) is frequently employed as the cathode material in LIBs, while graphitic carbon, in which the carbon atoms are arranged in parallel layers, is conventionally adopted as the anode. When charging a LIB, the lithium ions leave the LCO crystal by deintercalation, pass through the separator via the liquid electrolyte and is embedded again between the graphite layers by means of intercalation, while discharging leading to a reversal movement of the lithium ions [125].

Notably, only about 50% of the lithium can contribute to this process, since a larger loss would destabilize the LCO crystal structure, resulting in a substantial loss of performance. The reactions occurring during the discharge of a cell are summarized in Equations (14) and (15), involving the intercalation of Li^+ ions at the positive electrode, while in parallel electrons are emitted and Li^+ ions leave the negative electrode through deintercalation [125].

$$2\ Li_{0.5}CoO_2 + Li^+ + e^- \rightarrow 2\ LiCoO_2 \tag{14}$$

$$LiC_6 \rightarrow Li^+ + e^- + 6\ C \tag{15}$$

Considering the fact that the application of layered LCO involves some major disadvantages such as high cost, toxicity, and relatively poor rate capability, derivatives were investigated in which Co was to some extent replaced by more abundant and environmentally less critical elements such as Ni, Mn and/or Al [126]. These developments led to new compounds such as $LiNi_{0.8}Co_{0.15}Al_{0.05}O_2$ (NCA) or $LiNi_{0.33}Mn_{0.33}Co_{0.33}O_2$ (NMC), which have become the favored choice for several applications [126,127]. Besides layered cathode materials, there are several other structures suitable for LIBs, such as olivine-type $LiFePO_4$ (LFP), which is characterized by low cost, environmental friendliness and excellent safety, but exhibits low electronic and Li^+ ion conductivity due to the one-dimensional pathway in its structure [126,127]. Therefore, the application of this type of cathode material is limited mainly to large-scale batteries such as stationary energy storage systems [126].

2.4.3 LAS Glass-Ceramics

Glass-ceramics are a group of inorganic non-metallic solid materials that usually have a crystallinity of up to 95 % and contain a glassy residual phase [128]. These materials are produced by ceramization of glasses, which involves controlled nucleation and crystallization during thermal annealing, generally improving mechanical properties in terms of strength and toughness [9,128]. Within this group, Li_2O-Al_2O_3-SiO_4 (LAS) glass-ceramics in particular are characterized by their low coefficient of thermal expansion (CTE) of 0.1×10^{-6}/K or less for the temperature range from 20 to 700 °C, in addition to high mechanical strength, excellent thermal shock resistance and chemical durability [128]. Achieving the goal of low expanding LAS ceramics, the formation of crystalline phases with highly anisotropic CTE values such as high-quartz (β-SiO_2) with hexagonal symmetry (space group $P6_222$) or tetragonal keatite-type alumino-silicates (space group $P4_32_12$) are mandatory during manufacturing [128,129]. This rather unusual behavior of these LAS phases has been known since the early 1950s, when Hummel [130] and Smoke [131] contributed fundamental research on this material system [129]. The use of high-quartz materials for room temperature applications generally requires stabilization of the crystal

structure, since a reversible phase transition between low and high-quartz exists at 573 °C [129]. Therefore, at least 20 mol% of SiO_2 must be replaced by the pairs (Al_2O_3, Li_2O), (Al_2O_3, MgO) or (Al_2O_3, ZnO) to produce "stuffed derivates of high-quartz" [132,133], as can be seen in Figure 2-12. During this substitution, the strongly negative influence of lithium, the slightly negative influence of zinc and the strongly positive influence of magnesium on the CTE must be taken into account [10,129].

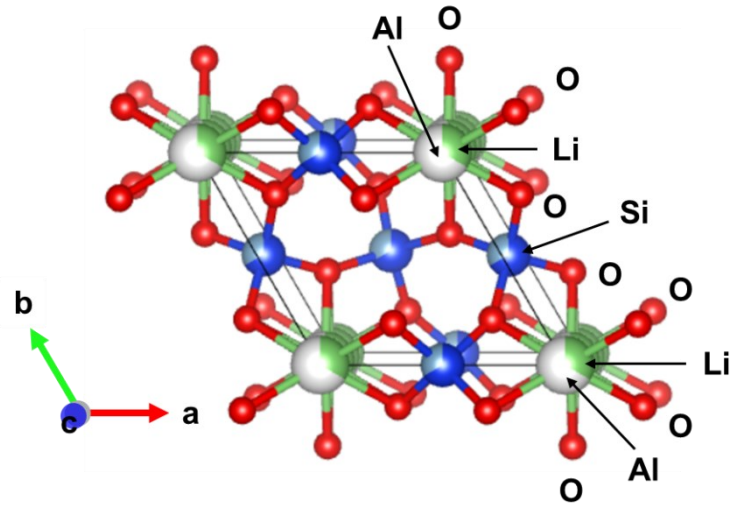

***Figure 2-12**. Idealized crystal structure on the unite cell level of a hexagonal high-quartz derived LAS phase, with a chemical composition of $Li_{0.33}Al_{0.33}Si_{0.67}O_2$, where significant amounts of the initial SiO_2 were substituted by Al_2O_3 and Li_2O to stabilize the structure for room temperature applications. Note that the figure was created with the use of VESTA 3 [134] employing atomic radii.*

In addition to the oxides already mentioned, components such as alkali oxides (Na_2O, K_2O) and alkaline earth oxides (BaO, CaO) are used to improve the melting behavior of the glass melt, while Sb_2O_3 and SnO_2 are used as fining agents [128,135]. Moreover, in order to obtain the characteristic fine-grained microstructure of LAS glass-ceramic with crystallites below 100 nm, the addition of TiO_2, ZrO_2 or a mixture of both is mandatory to promote the nucleation of the high-quartz phase [9,128,136]. Finally, the addition of transition metals or rare-earth elements are mandatory to produce glass-ceramic with a distinct color [135].

Especially the unique properties of LAS glass-ceramics are favorable for the production of cookware for household applications, stove tops for kitchen ranges or telescopic mirror blanks [9]. Therefore it is not surprising that Ceran© brand glass-ceramic cooktops are widely used around the world and have a market share of more than 70 % in the sale of electric cooking devices in Western Europe [137]. In addition, the high market share is supported by another study from 2014, which shows that around 600.000 to 900.000 of these cooktops are discarded in Germany every year [11]. In particular, the widespread utilization and the lithium content in the range of 2 to 3 wt%, which corresponds to hard rock ores currently mined [75], turn waste glass ceramics into a promising and previously unused secondary raw material for lithium recovery. Recycling of discarded electrical devices involved so far only on the recovery of transition metals, resulting in large quantities of lithium being lost along this disposal route [23]; an important aspect, which also triggered the research of this work.

3 Experimental Procedures

3.1 Sample Treatment

3.1.1 Utilized Chemicals

Sodium hydroxide solution made of solid sodium hydroxide (NaOH, Carl Roth, ≥ 99 %) was used for extraction and zeolite synthesis, while calcium oxide (CaO; Carl Roth, ≥ 96 %), phosphoric acid (H_3PO_4, 85 %, Carl Roth, analytical grade) and calcium hydroxide ($Ca(OH)_2$, Sigma Aldrich, ≥ 99 %) were used for desilication, precipitation and conversion of lithium phosphate into lithium hydroxide, respectively. Metal standard solutions (Titrisol, Merck, 1000 mg/L, analytical grade) were used to study the adsorption behavior of Pb^{2+}, Cu^{2+}, Zn^{2+} or Ni^{2+} ions on the synthesized zeolite samples. Sodium peroxide (Na_2O_2; Merck, ≥ 95 %), hydrochloric acid (HCl; Merck, analytical grade) and nitric acid (HNO_3; Merck, analytical grade) were used to digest solid samples for ICP-OES measurements, while potassium bromide (KBr, Carl Roth, analytical grade) was required to prepare pellets for FT-IR analyses.

3.1.2 Sample Materials and Pretreatment

In this study, four different lithium-containing sample materials were investigated with respect to lithium extraction and zeolite synthesis. Firstly, a glass−ceramic plate (see Figure 3-1 (a)) from an end-of-life cooktop, served as a secondary lithium source. Secondly, naturally occurring lithium minerals have been studied, such as lepidolite (see Figure 3-1 (d)) from the Bikita pegmatite near Masvingo in Zimbabwe, spodumene (see Figure 3-1 (g)) from the Sahatany pegmatite field (Mt. Ibity area) in the Vakinankaratra region of central Madagascar (purchased from MIKON Mineralienkontor GmbH, Gleichen, Germany) and Petalite (see Figure 3-1 (j)) from Luolamäki pegmatite near Somero, Finland (acquired from Rockhunter Handels UG, Waldalgesheim, Germany). Leaching experiments generally require fine and homogeneous powders, which is why a pre-treatment of the samples becomes necessary. This process involves first crushing the initial materials with a jaw crusher (Pulverisette 1, Fritsch, Idar-Oberstein, Germany), followed by comminution with a vibrating disk mill (Pulverisette 9, Fritsch, Germany) to a fine powder, and finally sieving with a vibrating screen (AS 300, Retsch, Haan, Germany) to a particle size of ≤ 500 µm. Additionally, the pretreatment of a glass-ceramic plate from a discarded cooktop, required manual disassembly to separate the plate from adhering electronical parts. Moreover, the mineral samples were additionally handpicked after jaw crushing and before disk milling to remove natural associated species such as quartz, feldspar or fluorite and altered parts of the sample, since both may affect subsequent analyses and experiments. For an illustration of the fractions obtained after the several pretreatment steps, see Figure 3-1.

Figure 3-1. *(a) to (c) Glass-ceramic samples derived from an end-of-life cooktop, (a) shard after manual dismantling, (b) after jaw crushing and (c) powder < 500 µm. (d) to (f) Lepidolite samples from the Bikita pegmatite, Simbabwe, (d) as received, (e) flakes after jaw crushing and (f) powder < 500 µm. (g) to (i) Spodumene samples from the Sahatany pegmatite, Madagascar, (g) as received, (h) cleavage pieces after jaw crushing and (i) powder < 500 µm. (j) to (l) Petalite samples from the Luolamäki pegmatite, Finland, (j) as received, (k) cleavage pieces after jaw crushing and (l) powder < 500 µm.*

3.1.3 Reference Experiments

Reference experiments were conducted with the objective of determining crystallite size without secondary chemical reactions by ball milling in water, while regular leaching attempts were undertaken to evaluate whether the use of ball milling in alkaline media is substantial for lithium release and/or zeolite formation. For this purpose, deionized water was employed instead of the NaOH solution in the ball milling experiments, while all other test parameters were retained. For the regular leaching experiments, a new experimental setup had to be prepared in which the samples were solely stirred in a 250 ml round-bottom flask in a temperature-controlled oil bath at 90 °C. In order to achieve results comparable with mechanochemical experiments, parameters such as time, liquid-to-solid ratio, temperature and concentration were fixed at the same values. After completion of the reference experiments, the same experimental procedure as described in chapter 3.1.4 was followed, including separation, washing, and drying of the samples.

3.1.4 Mechanochemical Leaching Experiments

In the context of this study, mechanochemical leaching experiments were performed on different source materials using a planetary ball mill (Pulverisette 6, Fritsch, Germany) equipped with 250 mL vessels with the aim of achieving high lithium extraction yields by combining ball milling with alkaline leaching in sodium hydroxide solution of varying concentrations. In general, mechanochemistry is a rather versatile method where several experimental parameters, as summarized in Figure 3-2, can be adjusted to promote the intended reaction.

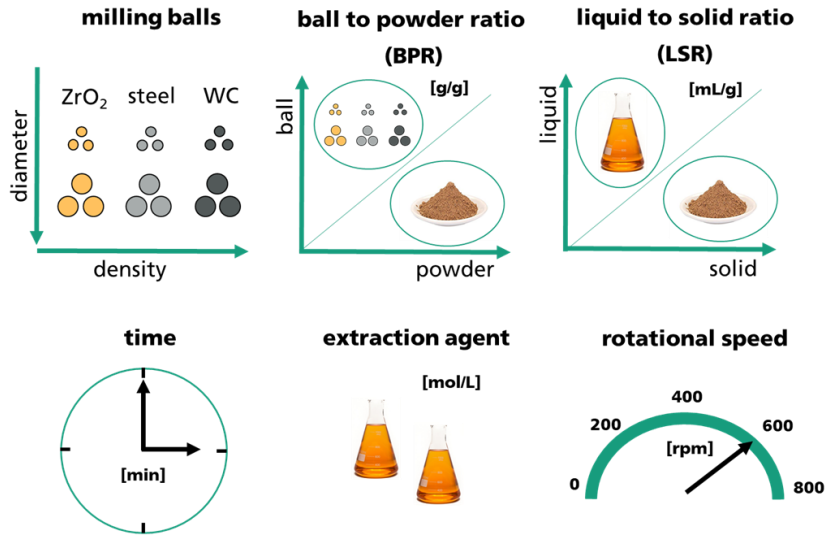

Figure 3-2. *Graphical abstract of typical experimental parameters during mechanochemical sample treatment. Own work, reproduced from [43].*

The majority of mechanochemical experiments are performed with milling balls, which are available in various diameters and made of materials with different densities, such as agate (2.6 g/cm^3), zirconium dioxide (6.0 g/cm^3), stainless steel (7.8 g/cm^3), or tungsten carbide (15.6 g/cm^3), as they provide an excellent means of transferring rotational energy to the sample materials. Therefore, when milling in alkaline media, balls and vessels made of a martensitic stainless steel 1.4125 (X105CrMo17) were used, which has excellent mechanical properties, suitable corrosion resistance and a Rockwell hardness of 55-60 HRC corresponding to a Vickers

hardness of 653 – 746 HV. During these studies, various experimental parameters namely NaOH concentration, rotational speed, milling time, and ball-to-powder ratio (BPR) were varied within the ranges of 1-9 mol/L, 100-650 rpm, 30-120 min, and 10-60 g/g, respectively, to examine their influence on lithium extraction as well as zeolite formation. At the same time the liquid-to-solid ratio (LSR), sample amount, and ball size were maintained at 10:1 mL/g, 10 g, and 10 mm, respectively. Additionally, the temperature of the reactor was recorded manually with a digital temperature sensor at the end of each milling step, since no cooling and heating procedure of the milling device was possible. Upon mechanochemically reaction, the obtained suspension was separated into a lithium-rich liquid and a solid fraction using a lab centrifuge (Allegra X-30R, Beckman Coulter, Brea, CA, USA). In order to avoid the formation of byproducts such as Na_2CO_3 via the reaction of residual NaOH with atmospheric CO_2 during drying, the leaching residues were washed with deionized water. An almost complete removal of the adhering NaOH could be achieved by repeating this washing procedure three times. Finally, the specimens were dried at 85 °C for 48 h and then gently homogenized in a mortar for further experiments and analysis.

3.1.5 Desilication Experiments

However, as an unavoidable side effect of alkaline Li extraction, Si and Al are also partially leached into the solution, requiring desilication of the solution as an important intermediate step to obtain a pure lithium compound, while avoiding precipitation of silica during further processing steps. For this purpose, two different approaches are known in the literature, where CaO [22,138] or calcium sulfate dihydrate ($CaSO_4 \cdot 2H_2O$) [139] are considered to be inexpensive and effective in removing silica from alkaline solution. Based on the experimental results of a previous study (Wolf 2022) [140], in which both routes were investigated in the context of lithium-containing alkaline solutions, the application of CaO possesses several advantages, such as shorter reaction time, higher desilication rate, and additional provided beneficial calcium silicate byproducts; hence, this route was preferred for this study. The experimental setup for desilication studies included a temperature-controlled oil bath in which the samples were stirred in a 250 ml round bottom flask at constant temperature and rotation speed of 95 °C and 450 rpm, respectively. In addition, the reaction time and CaO/SiO_2 ratio were varied to determine their influence on the on the removal of silica. During these experiments, only a few milliliters of samples were taken every 30 min to analyze the elemental composition of the solution via ICP-OES. Subsequently, the obtained reaction products were separated from the solution, rinsed with deionized water and finally dried at 85 °C and/or calcined at 900 °C.

3.1.6 Precipitation of Lithium Compounds

Upon purification of the solution through desilication, precipitation of a pure and easily handled lithium compound in the presence of excess Na^+-ions can be considered the final challenge of the adopted hydrometallurgical procedure. Considering that the precipitation of compounds mainly depends on their degree of solubility, the values for the relevant Li and Na species are summarized in Table 3-1.

Table 3-1. *Solubility of relevant lithium and sodium salts at different temperatures [141]. The lithium species relevant for precipitation are Li_3PO_4 and Li_2CO_3, which are both characterized by their low solubility, especially compared to their corresponding Na compounds. Noteworthy is the temperature-dependent solubility of Li_2CO_3 (highlighted in green) and Na_2CO_3 (highlighted in blue), which enable selective lithium precipitation at elevated temperatures.*

Compound	Solubility in H_2O [g/L]	Temperature [°C]
Li_2CO_3	13.3	20
Li_2CO_3	7.8	90
Li_3PO_4	0.3	20
LiOH	110.8	20
Na_2CO_3	178.6	20
Na_2CO_3	308.4	90
Na_3PO_4	107.8	20

By far the most frequently utilized route is the precipitation of lithium carbonate according to equation (16), which is accomplished by adding Na_2CO_3 to the lithium-containing solution at a temperature of about 90 °C. This setting is especially relevant for achieving high yields and purer precipitates, since the solubility of Li_2CO_3 decreases with rising temperature from 13.3 g/L (20 °C) to 7.8 g/L (90 °C), while the solubility of Na_2CO_3 increases in parallel from 178.6 g/L (20 °C) to 308.4 g/L (90 °C). These counteracting tendencies in solubility can be attributed to differences in enthalpy of solvation; for Li_2CO_3 this value is negative, therefore its solubility decreases with increasing temperature, whereas the opposite is observed for Na_2CO_3 with a positive enthalpy of solvation.

$$2\,Li^+_{(aq)} + Na_2CO_{3\,(aq)} \rightarrow Li_2CO_{3\,(s)} + 2\,Na^+_{(aq)} \qquad (16)$$

However, a previous study [140] has shown that the carbonate precipitation is only appropriate for highly enriched solutions with Li contents of 10 g/L or more, since at lower concentrations, as in this work of approximately 3 g/L, byproducts are formed in addition to the targeted Li_2CO_3 [140]. For this reason, an alternative approach was found via the precipitation of lithium phosphate (Li_3PO_4), which has a remarkably low solubility of 0.3 g/L at 20 °C, especially when compared to its sodium analogue Na_3PO_4 (107.8 g/L; 20 °C) or Li_2CO_3 (13.3 g/L; 20 °C). Therefore, this enables lithium precipitation even at lower concentrations according to equation (17), which can be further converted into ($LiOH{\cdot}H_2O$) following equation (18).

$$3\,LiOH_{(aq)} + H_3PO_{4\,(aq)} \rightarrow Li_3PO_{4\,(s)} + 3\,H_2O \qquad (17)$$

$$3\,Li_3PO_{4\,(s)} + 5\,Ca(OH)_{2\,(aq)} + 9\,H_2O \rightarrow 9\,LiOH * H_2O_{\,(aq)} + Ca_5(PO_4)_3OH_{(s)} \qquad (18)$$

Precipitation of Li_3PO_4 and further processing into $LiOH{\cdot}H_2O$ followed in general the approach of Mulwanda et al. [142], in which small amounts of phosphoric acid in molar ratios of phosphorus to lithium of 1.0:3.0; 1.2:3.0; 1.4:3.0; 1.6:3.0; and 1.8:3.0 were added to the solution, preheated to 90 °C in a round bottom flask through a glass cannula to produce Li_3PO_4. After prolonged stirring for another 60 min, the precipitated phosphates were isolated from the liquid, washed repeatedly with deionized water, and finally dried at 85 °C for 48 h. For

conversion into $LiOH \cdot H_2O$, 1.65 g of precipitated Li_3PO_4 was mixed with 50 mL of deionized water in a reflux vessel, while adding $Ca(OH)_2$ in 1.8-fold molar excess, heated to about 60 °C and held for 120 min. Subsequently, after the liquid solid separation, the dissolved $LiOH \cdot H_2O$ was crystallized through evaporation of the solution under an inert argon (Ar) atmosphere, avoiding any interaction with CO_2 from the atmosphere, which would favor the formation of Li_2CO_3.

3.1.7 Adsorption Experiments

Taking advantage of their special properties, zeolites are widely used for applications where molecular sieving or selective adsorption is required, such as the removal of harmful heavy metal ions in aqueous media [105,143,144]. Therefore, selected zeolite byproducts were investigated as potential adsorbents for the removal of Pb^{2+}, Cu^{2+}, Zn^{2+}, or Ni^{2+} ions from synthetic wastewater samples, which were made of single metal solutions diluted to a concentration of 100 mg/L. During these studies the adsorbent dosage was investigated in the range of 1 up to 15 g/L to evaluate their influence on the heavy metal removal efficiency. To achieve these dosages 50, 100, 150, 200, 300, 400, 500, 600, and 750 mg of zeolite were added to each of the 50 mL wastewater samples and placed afterwards in an overhead shaker for 120 min at room temperature. Upon liquid solid separation the adsorption efficiencies were calculated based on the ICP-OES results for the remaining liquid sample.

3.2 Analytical Techniques

As part of this work, various analytical methods were employed to be able to evaluate the solid and liquid samples arising from the mechanochemical investigations or the associated hydrometallurgical procedures. These methods are briefly summarized in Figure 3-3 as a flow sheet and are described in more detail below, whereby reference is made to the recommended literature for more detailed information.

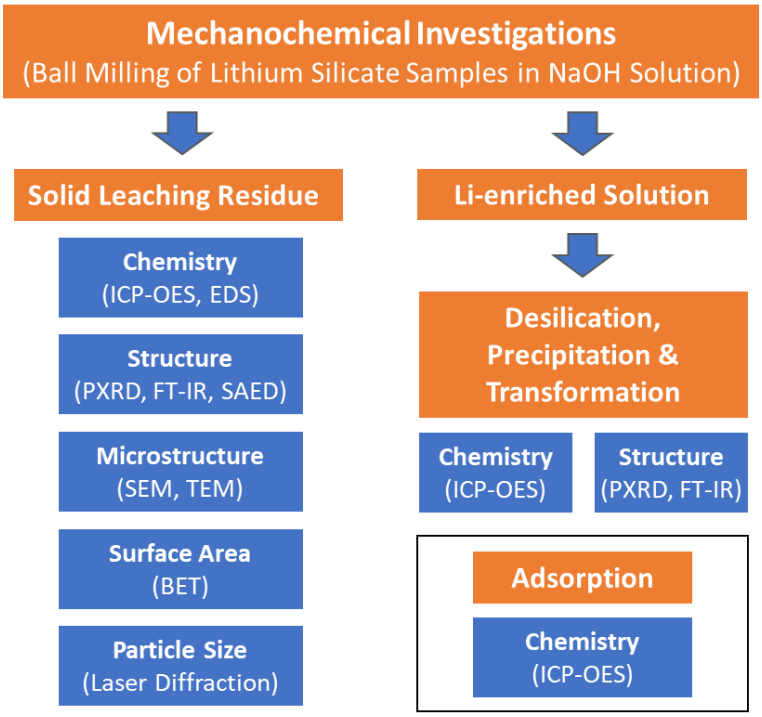

Figure 3-3. *Flowchart of analytical techniques applied during this work to evaluate liquid and solid samples, arising during mechanochemical investigations or the associated hydrometallurgical procedures. The corresponding samples are marked in ochre, while the methods are highlighted in blue.*

3.2.1 Inductively Coupled Plasma Optical Emission Spectrometry (ICP-OES)

ICP-OES was chosen for the chemical characterization of various samples, especially for the study of the inventory of starting materials as well as for the evaluation of the extraction, desilication, precipitation and adsorption experiments. For this purpose, an Optima 8300 spectrometer (PerkinElmer, Waltham, MA, USA) was selected, which allows the simultaneous determination of all metals relevant to this work, including lithium and some nonmetals such as P, at a low detection limit and excellent reproducibility from acidified aqueous solutions. During the measurement, several characteristic wavelengths were determined for each element, from which the two most suitable ones, which did not show any interferences or overlaps, were selected for quantification using the Syngistix 5.1 software (PerkinElmer, USA).

Each ICP device, as schematically illustrated in Figure 3-4, includes two analytical features that gave the method its name, where the term plasma refers to the ionized argon gas, while the energy required to maintain the plasma is transmitted electromagnetically via special induction coils. Especially, this plasma can be considered as the heart of any emission spectrometer, since here the injected substances are immediately atomized at high temperatures between 6,000 and 10,000 K, while subsequently atoms and ions are excited to emit electromagnetic radiation, mainly occurring in the ultraviolet and visible spectral range. After passing through several wavelength dispersive optics, the emitted light is used for detection and quantification, since there exists a linear relationship between intensity and concentration. Since the exact correlation between intensity and

concentration depends on a large number of partly unknown influencing variables, calibration with appropriate standard solutions is mandatory before each measurement, assuming that the slope of the calibration line of an element is equal in the standard and in the samples. In addition, internal standards of elements not present in the sample such as Sc are added to check the recovery rate and ensure reliable quantitative results. Finally, for more in-depth look on the ICP method, the textbook by Nölte is highly recommended, which covers both theoretical principles and practical aspects of ICP-OES analysis [145].

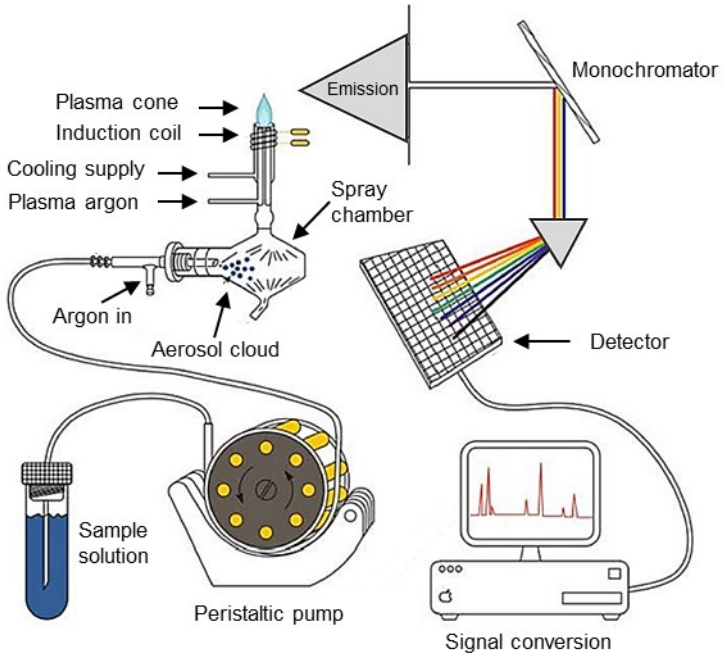

Figure 3-4. *Relevant components of an ICP-OES system. The most remarkable feature of this type of spectrometer is the argon plasma, in which the injected substances are immediately atomized at high temperatures, while atoms and ions are subsequently excited to emit electromagnetic radiation, thereby providing a chemical fingerprint of the sample. Figure adopted from [146].*

Liquid samples of low concentration are directly measurable by the ICP-OES method, while highly concentrated solutions such as leachates required a dilution in a ratio of 1:100 or 1:200 depending on the elemental content. However, solids have to be digested prior to analysis. Silicate samples had to be fused with threefold excess of Na_2O_2 in a zirconium metal crucible (HRT Fusion, Seevetal, Germany) at 460 °C for 60 min, followed by digestion with HCl, while solids expected to be more soluble were prepared for analysis via aqua regia digestion (HCl:HNO_3 in a ratio of 3:1) without any heat treatment.

In order to evaluate the leaching experiments, the obtained ICP-OES results were taken to calculate an extraction rate (synonymously extraction) for lithium R_{Li} [%] following equation (19), where C_0 [g/L] represents the mass concentration of metal ions in the leachate, V_0 [L] the leachate volume, *m* [g] the sample mass, and w % [g/g] the metal mass fraction of lithium in the feed stock.

$$R_{Li} = \frac{C_0 * V_0}{m * w\,\%} * 100 \qquad (19)$$

In addition, the adsorbent removal efficiency (%) was calculated by using ICP-OES results of the initial heavy metal concentration in the waste water sample C_i [mg/L] and the final concentration of metal ions after adsorption C_f [mg/L] following equation (20).

$$Removal\ effiency\ [\%] = \frac{(C_i - C_f)}{C_i} * 100 \qquad (20)$$

3.2.2 Powder X-ray Diffraction (PXRD)

Phase analysis of various samples including source materials, leaching residues, solid byproducts or precipitates obtained along the extraction route were performed via PXRD. Therefore, an X-ray diffractometer in Bragg-Brentano geometry (Empyrean, Malvern Panalytical, Malvern, UK), as depicted in Figure 3-5, was selected, operating at 40 mA and 40 kV and equipped with a cobalt source with a wavelength of λ = 1.78901 Å. These investigations recorded diffraction patterns within the 2 θ range from 10 to 75 °, which includes all of the main diffraction peaks of the expected phases, using a scan speed of 0.006 °/s and a step size of 0.013 °. Moreover, the data obtained were evaluated with the aid of the HighScore Plus software (Malvern Panalytical, U.K.), equipped with an inorganic crystal structure database (ICSD; FIZ Karlsruhe, Karlsruhe, Germany).

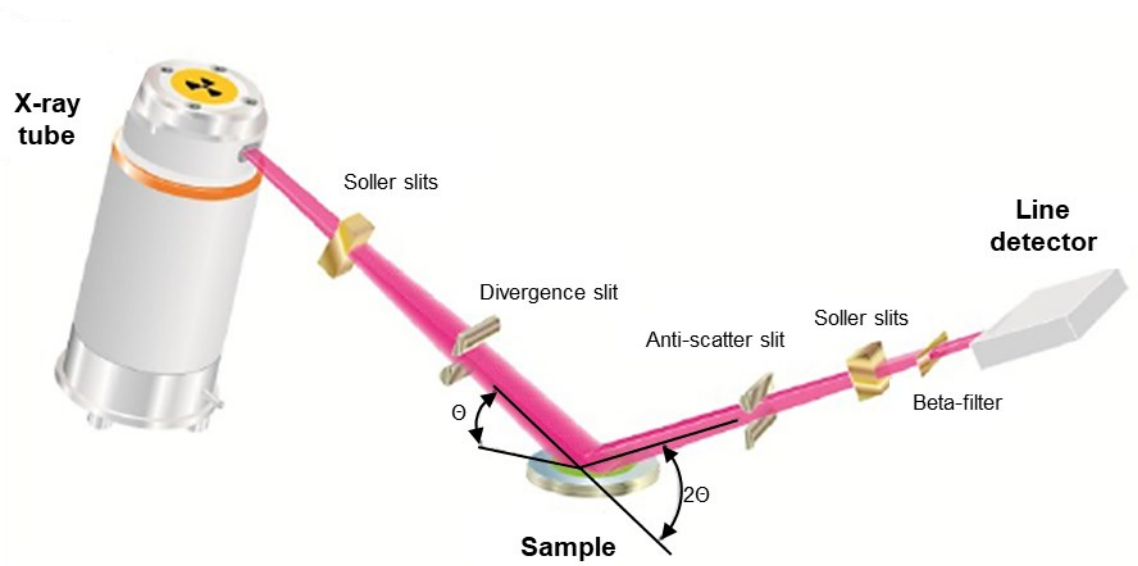

Figure 3-5. *Typical PXRD setup in Bragg-Brentano geometry including several beam optics to ensure a high signal-to-noise ratio. During the measurements, both the X-ray tube and the detector are moved upwards to collect data at higher 2Θ angles. Figure adopted from [147].*

Physically, diffraction occurs only when the wavelength of the incident wave and the spacing of the diffraction lattice have the same order of magnitude, which is the case for crystalline materials with lattice spacings equal to the wavelength of the X-rays. Therefore, the X-rays are diffracted by the electron shell of the irradiated atoms, while the diffracted waves of the individual atoms interfere with each other, resulting in constructive or destructive interference, which for a fixed angle depends solely on the distance between the atoms. Since constructive interference occurs only at certain characteristic angles, they can be related to the distance of certain lattice planes in the crystal on the basis of the Bragg equation (see equation (21)), where *n* represents a natural number, λ the wavelength of monochromatic radiation, *d* the spacing of lattice planes and Θ the Bragg angle between the beam and the lattice plane.

$$n * \lambda = 2 * d * sin\,\theta \tag{21}$$

In addition, the Scherrer equation (equation (22)) was chosen for the determination of the crystallite size *D* in reference experiments, where *K* stands for the Scherrer constant, λ for the wavelength of the radiation, *B* for the full width at half maximum (FWHM), and Θ for the Bragg angle. It is noteworthy that all calculations were

performed on the main diffraction peaks, assuming K = 0.9, in accordance with Salakjani et al. [13], who studied similar samples. For a comprehensive overview of X-ray diffraction, the reader is referred to Spieß et al. [148] and Waseda et al. [149].

$$D = K * \lambda/(B * \cos\theta) \quad (22)$$

Specimen preparation for PXRD includes manual homogenization of the powders using mortar and pestle, while the following procedures differ slightly depending on the amount of sample available for analysis. In cases where only small quantities were available, a sample holder with zero diffraction plate was employed, which consists of a boron-doped oriented silicon crystal that guarantees no background noise for a wide range of 2θ angles. When using this holder, the powder must be loaded into the well from the front and the sample height has to be carefully leveled manually by adjusting the powder with a glass plate. For larger sample volumes, ring-shaped stainless-steel holders were chosen, which were back-loaded with the powders using a semi-automatic preparation device to ensure a smooth and uniform surface, which is generally mandatory for accurate measurements.

3.2.3 Fourier Transform Infrared Spectroscopy (FT-IR)

FT-IR analysis was chosen to identify changes in the molecular bonding of silicon and aluminum within the samples during mechanochemical reactions initiated by intensive ball milling. Therefore, a Michelson type interferometer (model Nicolet is50, Thermo-Fisher Scientific, Waltham, MA, USA), schematically illustrated in Figure 3-6, was chosen, analyzing KBr pellets in the mid-infrared region from 4000 to 400 cm^{-1}. Moreover, for each sample 32 scans were recorded at a resolution of 4 cm^{-1}, while blank values were acquired before each data set. The OMNIC software (Thermo-Fisher Scientific, USA) was taken to evaluate the recorded FT-IR data.

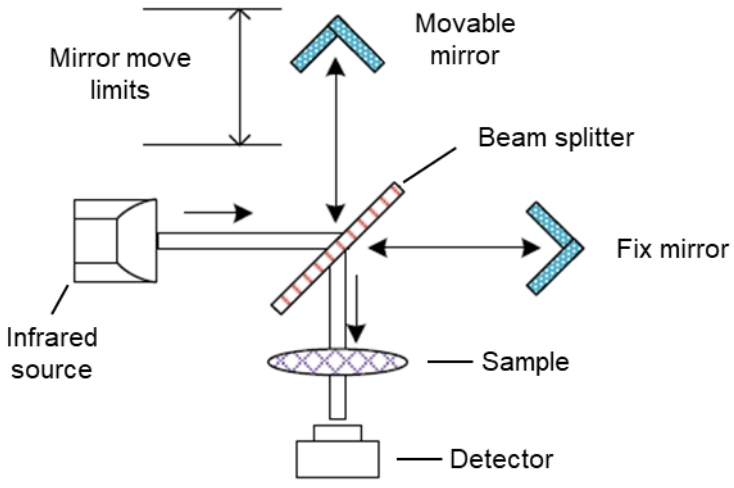

Figure 3-6. *Schematic illustration of a Michelson interferometer adopted for Fourier transform infrared (FT-IR) investigations. Figure adopted from [150].*

Generally, in IR spectroscopy, the interaction of electromagnetic radiation with matter is examined in the infrared range, which triggers the vibration of certain molecular bonds such as symmetric or antisymmetric stretching vibrations or bending vibrations such as deformation, rocking, wagging or twisting. In principle, the oscillation of molecular bonds leads to a partial consumption of energy by absorption, which is lacking when compared to the original IR radiation. Within the resulting IR spectrum this energy loss can be considered as a

chemical fingerprint, which is characteristic for each material. For a more profound insight, the textbooks by Stuart [151] and Günzler & Gremlich [152] are recommended, which summarize relevant aspects of IR spectroscopy.

Specimen preparation for FT-IR examinations involves the preparation of IR-transparent KBr pellets, which ensure a high signal-to-noise ratio during the measurement. Therefore, the sample was mixed with oven-dried KBr in a ratio of about 1:100, homogenized with a mortar and pestle, and finally pressed into a pellet using a manual hydraulic laboratory press (Specac, Orpington, UK) equipped with a customized pellet die.

3.2.4 Gas Adsorption/Desorption

Gas adsorption/desorption in combination with the F (BET) method [153] was chosen to determine the specific surface area of the synthesized zeolite samples, using a 3Flex adsorption analyzer (Micromeritics, Norcross, GA, USA). The application of the BET method assumes the physical multilayer adsorption of probing gas molecules (adsorptive) such as N_2 on solid surfaces (adsorbent) without chemical reaction, which can be used for the quantification of a specific surface area. During these studies, full adsorption/desorption isotherms were recorded for each sample of interest at constant temperature of – 196 °C (boiling point of liquid nitrogen), where the adsorbed N_2 volume was recorded as a function of partial pressure. Moreover, for the calculation of the specific surface via a BET plot only a 10-point measurement in the lower linear part of the isotherm at relative pressures between 0.05 and 0.3 p/po was selected, as exemplarily shown in Figure 3-7.

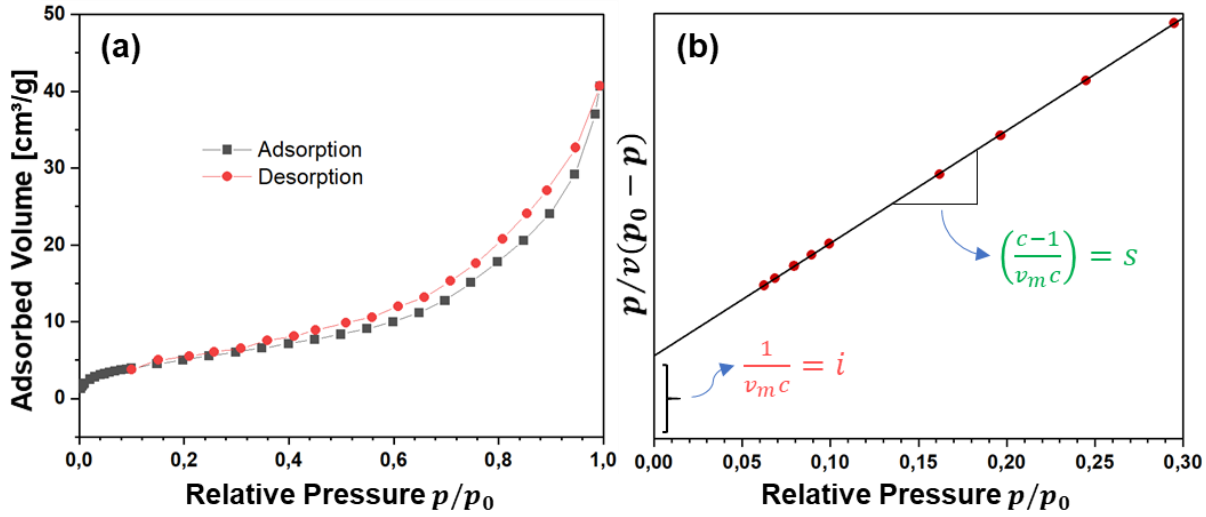

Figure 3-7. *Gas adsorption/desorption investigations exemplarily shown for one of the zeolite samples. (a) Full adsorption/desorption isotherm and (b) BET plot based on a 10-point measurement at relative pressures between 0.05 and 0.3 p/p_o, which represents the linear section of the isotherm (a). The intercept (i) and the slope (s) in (b) are considered for the calculation of the monolayer adsorption v_m, which in turn is necessary for the determination of the BET surface area S_{BET} according to equation (25).*

The BET model can be described by equation (23), where *v* is the adsorbed volume, v_m the adsorbed volume of the monolayer, *C* an empirical constant, *p* the pressure and p_0 the saturation pressure. Since a BET plot represents a linear equation, the intercept (*i*) with the Y-axis corresponds to $\frac{1}{v_m c}$, while the slope (*s*) is equal to $\left(\frac{c-1}{v_m c}\right)$. Therefore, both values can be taken to calculate the BET monolayer capacity v_m following equation (24). Subsequently, the specific BET surface (S_{BET}) can be determined according to equation (25), where *s* represents

the adsorption cross section of the adsorbate, N_A = 6.022 · 10^{23} molecules/mol the Avogadro number, *V* the volume of the adsorbate gas and *m* the mass of the sample.

$$\frac{p}{v(p_0-p)} = \frac{1}{v_m c} + \left(\frac{c-1}{v_m c}\right)\frac{p}{p_0} \tag{23}$$

$$v_m = \frac{1}{i+s} \tag{24}$$

$$S_{BET} = \frac{v_m s N_A}{Vm} \tag{25}$$

Since gas adsorption/desorption is sensitive to any physically adsorbed substances on the sample surface, a preconditioning step by outgassing with a Smart VacPrep unit (Micromeritics, Norcross, GA, USA) at 200 °C for 720 min under vacuum is mandatory to produce clean and dry surfaces, which are essential for reproducible results. For a more profound perspective on gas adsorption/desorption for analytical purposes , the textbooks by Lowell et al. [154] and Webb & Orr [155] are recommended.

3.2.5 Optical Microscopy (OM)

An Axio Zoom.V16 microscope (Zeiss, Jena, Germany) was chosen for the characterization via OM of the starting materials. Therefore, approximately 50 focus-stacked images per sample were recorded and merged together to obtain a three-dimensional image of the powder specimens.
Sample preparation for light microscopy of the starting materials included suspension of the powders in ethanol using an ultrasonic bath, while removing the finest dust fraction after sedimentation to obtain clean and pristine particles for imaging. Therefore, after evaporation of the ethanol, the pre-treated particles were loosely spread on a glass slide for further examinations.

3.2.6 Scanning Electron Microscopy (SEM)

A high-resolution field emission Merlin SEM (Zeiss, Jena, Germany) was employed to study the morphological properties and microstructures of the starting materials and the synthesized zeolite samples, mainly via secondary electron (SE) imaging at low acceleration voltages of 2 – 5 kV. In general, SEM involves scanning the sample surface with an electron beam, where the interaction of the beam and the sample volume generates various secondary signals which are captured by special detectors. This includes, surface-near secondary electrons (SE), which are acquired for high-resolution topographical imaging of the sample surfaces. Besides, backscattered electrons (BSE), exhibiting a chemical contrast, since scattering of the primary electron beam strongly depends on the atomic number of the elements contained in the sample. Lastly, both of these imaging modes are supplemented by semiquantitative elemental energy-dispersive X-ray spectroscopy (EDS) analysis, while employing the emitted characteristic X-rays at acceleration voltages of about 8 – 10 kV. More detailed information on the methodology and a comprehensive overview can be found in Goldstein [156].
SEM investigations of the starting materials involved the same sample preparation procedures, already described in chapter 3.2.5, followed by mounting of the pristine particles on a SEM stup by using conducting silver paint. For the much finer zeolite particles in contrast, a drop of the ethanol suspension of the sample was applied directly to a piece of a polished silicon wafer without further adhesive. After evaporation, the adhesive

forces of the fine particles were strong enough to hold them in place during subsequent SEM analysis. Finally, all SEM samples were gently sputtered with a thin, approximately 5 nm thick layer of copper, thus reducing charging artifacts during electron microscopic examinations.

3.2.7 Transmission Electron Microscopy (TEM)

For micro- and nano structural characterization of selected samples via conventional TEM, a JEM-2100F microscope (JEOL, Tokyo, Japan) operating at 200 kV and equipped with a field emission electron gun and a double-tilt beryllium holder (JEOL, Tokyo, Japan) was selected. For image acquisition an UltraScan 1000 CCD camera (Gatan, Pleasanton, USA) together with the corresponding Gatan Microscopy Suit software was chosen, while obtained diffraction patterns were analyzed either manually or using specialized diffraction analysis tools such as PIEP [157] or ReciPro [158]. Once the challenge of fabricating thin, electron-transparent samples (typically less than 100 nm) is overcome, TEM is a remarkably versatile characterization method for a wide range of materials, as it combines the key capabilities of simultaneously obtaining both real-space images of a region of interest at high magnifications and localized diffraction patterns using selective area electron diffraction (SAED). Further details on this topic can be found in the cited literature by Williams & Carter and Thomas & Gemming [159,160].
Powder samples for the TEM examinations were prepared according to the standard procedure involving gentle comminution in a mortar, suspension in ethanol for deagglomeration, and dispersion in an ultrasonic bath, followed by deposition of a few droplets on a special TEM copper grid coated with a holey carbon film. Finally, upon evaporation of the solvent, the samples were coated with a thin carbon layer to reduce charging artifacts during TEM investigations.

3.2.8 Energy-Dispersive X-ray Spectroscopy (EDS)

To complement the SEM and TEM studies, semiquantitative chemical data with spatial resolution were obtained by EDS using an XMAX 80 detector (Oxford Instruments, Abingdon, UK) attached to each of the microscopes and analyzed with the aid of INCA or AZtec software (both Oxford Instruments, Abingdon, UK).
Whenever an electron beam with sufficient kinetic energy hits the sample, electrons of the inner shell of an atom may be ejected, resulting in a gap in the electron structure, which is energetically unstable and therefore immediately filled by an electron from a higher atomic orbital. As a result of this process, an X-ray quantum is released whose energy is characteristic of the particular transition and of the emitting element. When these signals are detected by an EDS detector, they allow rapid and accurate determination of the major elements of a sample in a semi-quantitative manner, whereas minor or trace elements cannot be captured by using this method. Depending on the composition of the sample, higher voltages are required with increasing atomic number to produce characteristic X-rays, which must be taken into account during SEM analysis (1-30 kV), especially when imaging with low accelerating voltages, while it is generally not a critical issue during TEM analysis (200 kV). For further details on EDS the reader is referred to the textbook of Goldstein [156].

3.2.9 Determination of the Loss on Ignition (LOI)

The loss on ignition, corresponding to the proportion of volatile components in the starting materials, was determined using a STA 449 F3 Jupiter Thermo-Gravimetric Analyzer (Netzsch, Selb, Germany), while the measurements were evaluated applying the Proteus 80 software (Netzsch, Germany). For this purpose, oven dried samples (105 °C, 48 h) were heated to 1050 °C at a rate of 10 °C/min, while the final temperature was held for additional 120 min to ensure entire degassing of volatile components.

3.2.10 Particle Size Measurements

A combination of a Mastersizer 3000 and an Aero S dry powder disperser (both Malvern Panalytical, Malvern, UK) was used to determine the particle sizes in the starting materials and the ball-milled samples, generally allowing the determination of particle size distributions in the range of 0.1 µm to 1000 µm based on laser diffraction. During this type of measurement, a laser beam passes through a sample of dispersed particles while the angular change in the intensity of the scattered light is measured, with large particles scattering the light at small angles relative to the beam, while small particles scatter the light at large angles. Finally, the obtained scattering pattern is employed to calculate the size of the corresponding particles following the Mie theory of light scattering. The resulting particle size is typically expressed as a volume equivalent spherical diameter and summarized in d_{10}, d_{50} and d_{90} values, each of which indicates the percentage of the sample that is smaller than the corresponding value (e.g., d_{50} = 150 µm implies 50 % of the particles are smaller than 150 µm). For further details on particle-size measurements the reader is referred to the textbook of Stiess [161].

4 Results and Discussion

4.1 Characterization of the Feed Materials

Prior to leaching experiments, characterization of the source materials was mandatory to gain a chemical, structural and microscopic insight about the sample material. In particular the chemical inventory of the source materials on main and side elemental level are of importance for the validation of the leaching experiments, while corresponding structural and microscopic investigations are employed to characterize the phase composition of the samples and to identify impurities and impurity phases.

4.1.1 Chemical Investigations via ICP-OES

Chemical analysis of the four feed materials via ICP-OES measurements are summarized as oxide values in Table 4-1 indicating Li_2O contents of 4.52 wt% (glass-ceramic), 5.61 wt% (lepidolite), 7.32 wt% (spodumene), and 5.16 wt% (petalite) besides the main elements silicon and aluminum.
Please note, small amounts of BaO (1.18 wt%), TiO_2 (3.10 wt.%), ZnO (1.29 wt.%) and ZrO_2 (1.51 wt.%) were only present in the glass-ceramic samples, which cannot be classified as impurities. On the contrary, each of these elements fulfills a specific function during the manufacturing process or enables tailoring the microstructure and the characteristic properties of this material system, as already described in chapter 2.4.3. Being consistent with its molecular formula, the lepidolite sample also contained K_2O (12.3 wt%) as a major constituent, in combination with smaller amounts of Rb_2O (1.7 wt%), which has the potential to contribute as a value-added byproduct in lithium production. Furthermore, analytical results indicate the presence of lower amounts of other oxides such as of Fe_2O_3, MnO, CaO (see Table 4-1) in lepidolite, spodumene, and petalite samples, which are attributed to common impurities in natural rock-forming minerals. In particular, Na, which should be present in small amounts in all materials, is not reliably detectable due to the excess of Na_2O_2 used during sample digestion. In addition, F, which is relevant for lepidolite samples, cannot be determined with ICP-OES as this element is difficult to excite with this technique, an aspect that also extends to the entire group of halogens. Supplementary to ICP-OES measurements, the comparatively high LOI values of 3.0 % in lepidolite samples indicate the presence of volatile compounds such as F or OH.

Table 4-1. *Chemical composition of the feed materials based on ICP-OES measurements, recalculated into oxide values. The values in bold are discussed in the following section, while the Li_2O content is highlighted additionally in blue as it is most relevant to this study. Highlighted in green is the loss on ignition (LOI), which corresponds to the proportion of volatile components in the starting materials.*

	Glass-Ceramic [wt%]	**Lepidolite [wt%]**	**Spodumene [wt%]**	**Petalite [wt%]**
Al_2O_3	21.46	23.82	27.34	16.24
BaO	**1.18**	< 0.01	< 0.01	< 0.01
CaO	0.13	0.15	0.19	0,13
Fe_2O_3	0.23	0.14	0.41	0.14
K_2O	0.42	**12.30**	0.24	0.39
Li_2O	**4.52**	**5.61**	**7.32**	**5.16**
MgO	0.45	< 0.01	0.02	0.18
MnO	n.n.	0.66	0.13	n.n.
Rb_2O	< 0.01	**1.70**	< 0.01	< 0.01
SiO_2	56.26	52.35	64.46	71.09
SnO_2	0.13	0.02	< 0.01	< 0.01
TiO_2	**3.10**	0.05	0.02	< 0.01
ZnO	**1.29**	0,02	< 0.01	< 0.01
ZrO_2	**1.51**	0.06	0.07	0.06
LOI	0.3	**3.0**	0.4	0.5

4.1.2 Structural Characterization via PXRD

Structural investigations by PXRD on LAS glass-ceramic (see Figure 4-1 (a)) revealed the high-quartz phase with hexagonal space group $P6_222$ (PDF#98-007-3072) as the main phase, while tetragonal beta-spodumene (β-$LiAlSi_2O_6$, space group $P4_32_12$, PDF#98-002-6817) occurs as a minor phase, both of which are consistent with literature data [129]. In addition, a strongly broadened diffraction peak around 36 °2Θ was observed in the LAS sample, which cannot be clearly assigned to a specific phase with the aid of PXRD, whereby $ZrTiO_4$ (*Pbcn*; PDF# 98-015-3942) or ZrO_2 ($P4_2/nmc$; PDF#98-009-3028) are considered as possible candidates. Furthermore, PXRD measurements on the lithium mineral samples (see Figure 4-1 (b)-(d)) confirm the expected phases such as lepidolite (PDF#98-003-0784), spodumene (PDF#98-028-0109) and petalite (PDF#98-010-0348) in relatively pure samples, while cogenetic phases such as low-quartz (PDF#98-020-1354) or analcime (PDF#98-004-0451) play only a minor role. Even if the occurrence of analcime in petalite samples may be surprising at the first moment, this observation is well known in literature [162]. Overall, the recorded data generally agree well with the reference patterns, with the only exception being the lepidolite sample, where the 001 reflections occurring at 10.37, 20.77 and 31.35 °2Θ, corresponding to the 002, 004 and 006 planes, respectively, are more intense than in the references. This is associated with a slightly preferential texturing of the platelet-shaped mica lamellae during sample preparation, which is inevitably a challenge with this group of sheet silicates. In addition to the

phase analysis, the PXRD method was also chosen to estimate the crystallite size of the lithium-containing phases in the starting materials, whereby the broadening of the diffraction peaks was investigated by means of the Scherrer formula (equation 21). In the case of the LAS glass-ceramic, the main diffraction peak at 29.5 °2Θ corresponds to an estimated crystallite size of about 70 nm, being consistent with literature data where attempts are generally made to avoid crystallites above 100 nm during manufacturing to exclude scattering effects and ensure transparency of the glass-ceramic [135]. Estimates on mineral samples, on the other hand, did not yield any reasonable results, which is attributed to the comparatively large crystallite sizes of up to 500 µm, which clearly exceed the upper limitation of the Scherrer equation of around 200 nm.

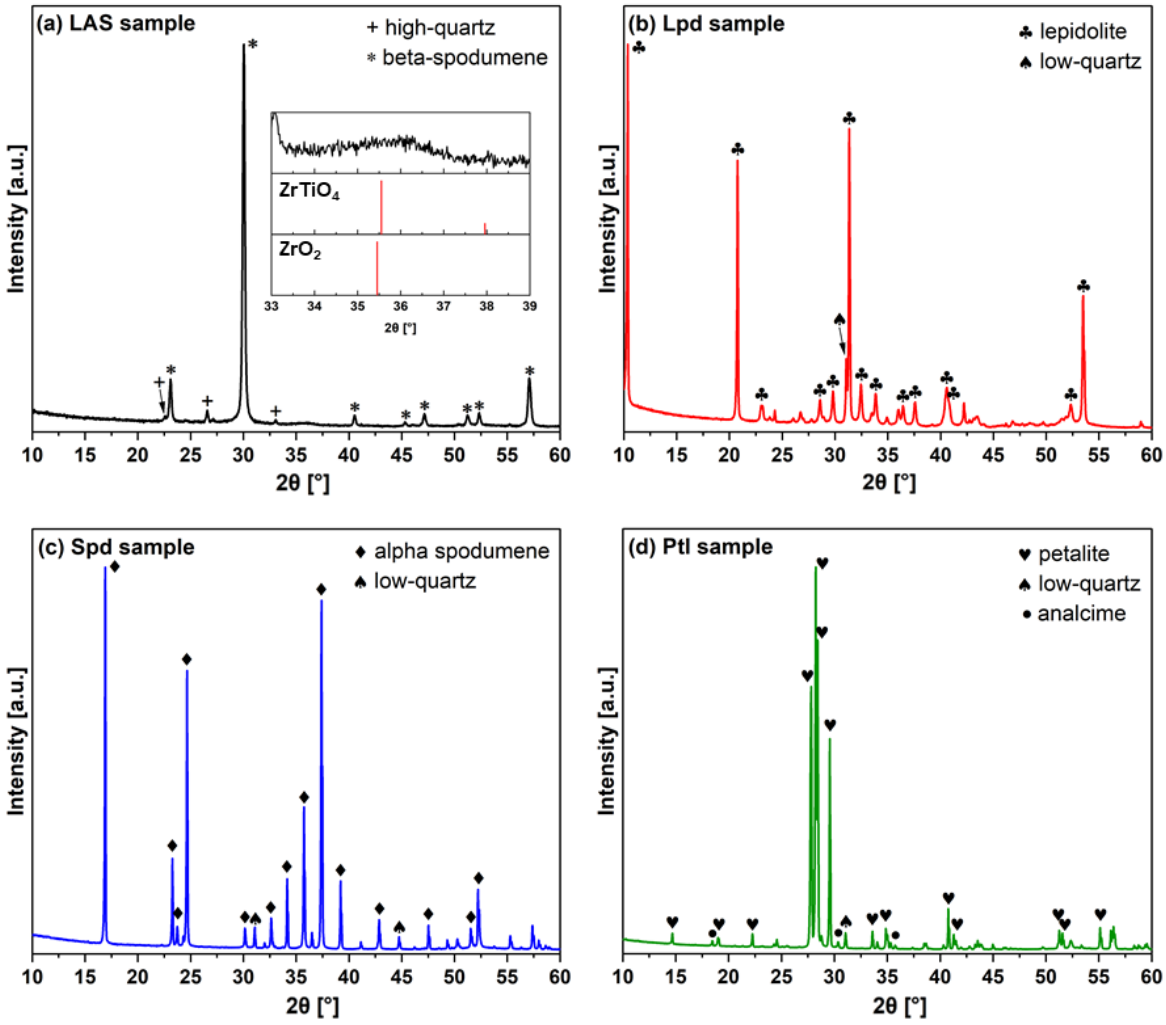

Figure 4-1. *Diffraction patterns of the investigated source materials revealing the presence of lithium-rich phases besides minor amounts of cogenetic phases or trace minerals. (a) LAS glass-ceramic (LAS), (b) lepidolite (Lpd), (c) spodumene (Spd) and (d) petalite (Ptl). Own work, reproduced from [23,24].*

4.1.3 Microscopic Investigations using OM, SEM and SEM-EDS

Even OM examinations at moderate magnifications (see Figure 4-2) reveal translucent sample particles, which clearly differ in terms of shape and morphology. Glass-ceramic particles are irregularly shaped without preferential orientation, while examinations on the mineral samples exhibiting thin platelets of lepidolite, slightly thicker plates of petalite and rod-shaped particles of spodumene.

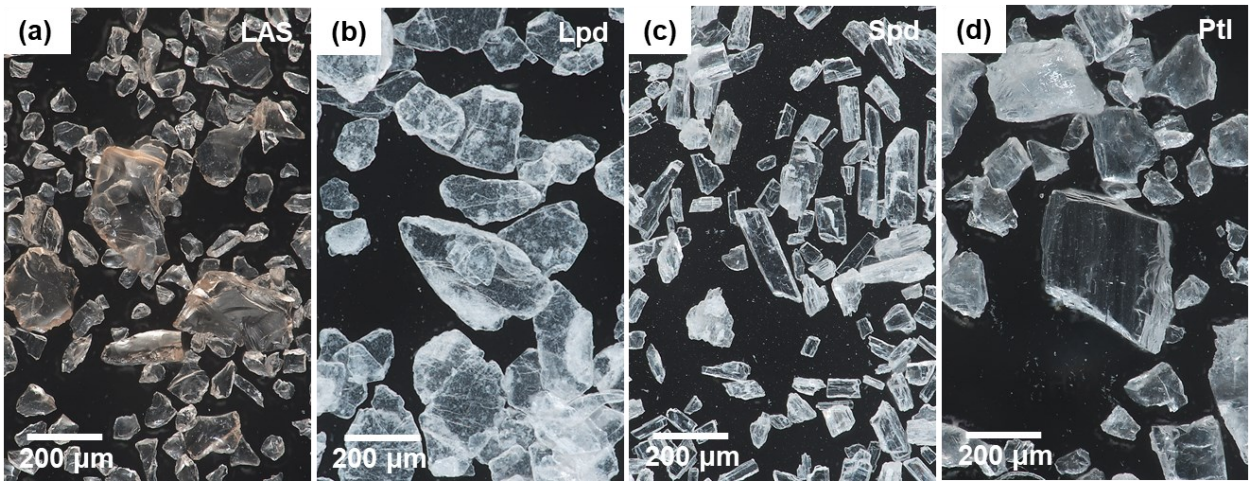

Figure 4-2. *Optical microscopy images of source material powders (≤ 500 µm) after pretreatment: (a) LAS glass- ceramic, (b) lepidolite, (c) spodumene and (d) petalite.*

Supplementary to OM, imaging via SEM-SE at slightly higher magnification confirmed the previous findings on particle morphology, which can be correlated with their specific crystallographic properties. According to Figure 4-3 (a) and (b), irregular particle shapes with conchoidal fractures were observed in the glass-ceramic sample, which is a characteristic feature occurring in very fine-grained to amorphous materials or minerals without pronounced cleavage. In contrast, mechanical pretreatment resulted in cleavage along specific crystallographic planes in all mineral samples, where the weakest bonds occur within their structures, leading to characteristically shaped cleavage lamellae. Thus, the perfect (001) cleavage resulted in the formation of thin lamellae in the lepidolite samples (see Figure 4-3 (d) and (e)), and slightly thicker platelets in petalite samples (see Figure 4-3 (g) and (h)), while cleaving along the same orientation. In contrast, the spodumene powder exhibited characteristic rod-like particles as can be seen in Figure 4-3 (j) and (k), which are the result of two cleavage systems along (110) and (1-10), intersecting at an angle of approximately 90 degrees. Aided by the semi-quantitative EDS measurements (see Figure 4-3 (c); (f); (i) and (l)), the major elements of the source materials such as Al, Si, and O were detected with the exception of Li, which generally cannot be detected with standard EDS detectors. Corresponding to its molecular formular, K and F signals are recorded in lepidolite specimens. Moreover, minor elements such as Ba, Ti, Zr, Na, Ca, Mg were exclusively confined to the LAS sample (see Figure 4-3 (c)), while the minor Cu and C signals, occurring in all specimens originated, from the sample coating. Finally, OM, SEM and SEM-EDS indicate homogeneous and pristine samples within the investigated scale without any altered sample parts, foreign particles or major impurity phases, which is consistent with the PXRD study, revealing only the expected lithium containing phases.

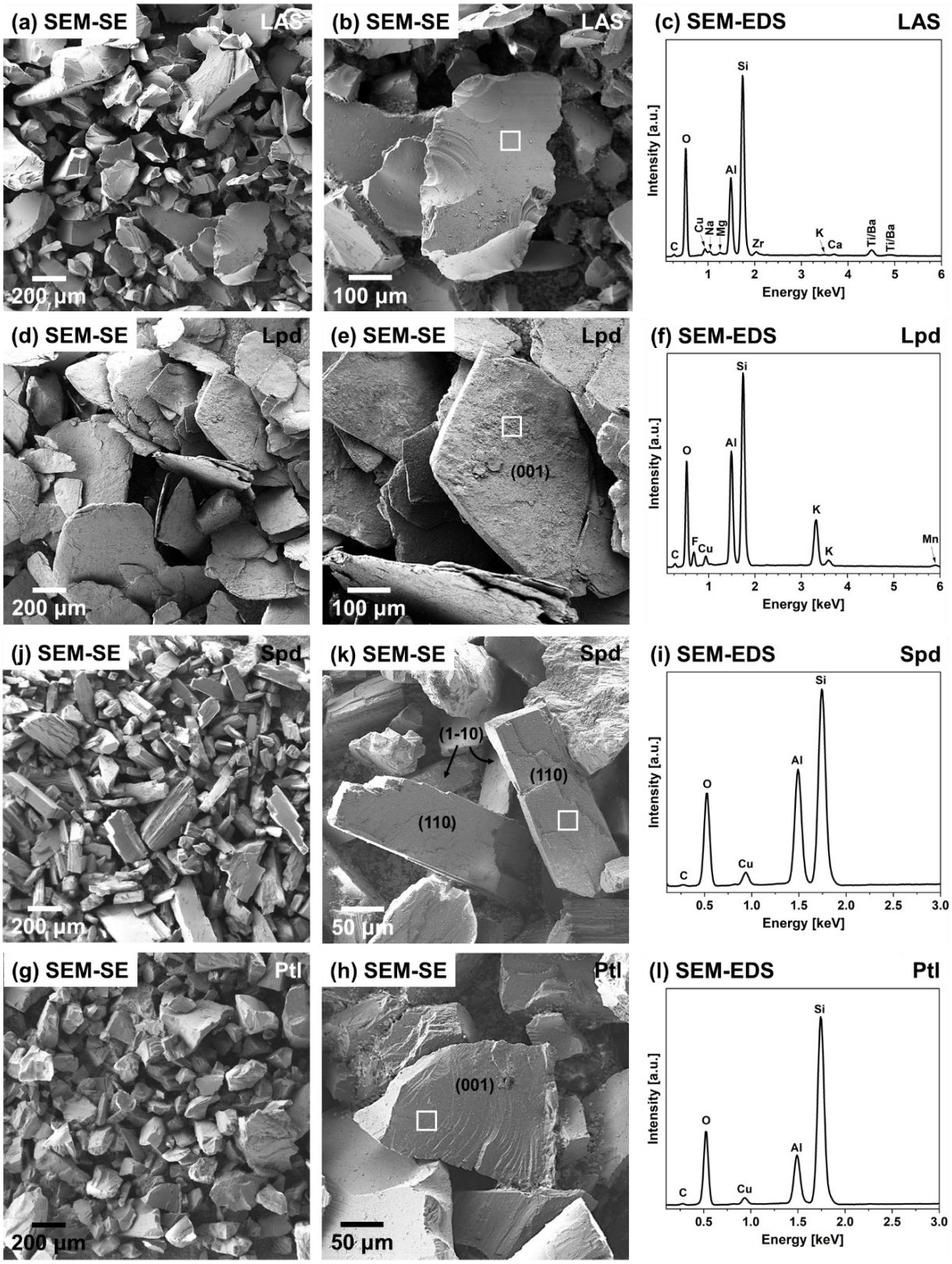

Figure 4-3. *SEM-SE micrographs at different magnifications with corresponding SEM-EDS measurements of selected areas of (a) to (c) LAS glass-ceramic (LAS), (d) to (e) lepidolite (Lpd), (g) to (i) spodumene (Spd) and (j) to (l) petalite (Ptl) samples, highlighting the most prominent cleavage planes and the areas where EDS data were acquired. Notably, small EDS signals of C and Cu originate from sample coating.*

4.1.4 TEM Investigation on LAS Glass-Ceramic Samples

Analytical investigations of lithium minerals resulted in homogeneous and monomineralic samples, which are comparatively coarse-grained due to their pegmatitic origin. Therefore, TEM investigations focused only on LAS glass-ceramic samples in order to resolve their microstructural features. TEM bright-field imaging (TEM-BF) revealed glassy samples containing two different types of crystallites (see Figure 4-4 (a) and (b)). Smaller nm-sized crystallites were present in high abundance and characterized by their euhedral, rod-shaped habit with a rectangular cross-section, while in contrast much larger ones of 50 to 70 nm in size and with a spherical shape were observed less frequently. With the aid of SAED and/or HRTEM imaging (see Figure 4-4 (c) and (d)) in conjunction with localized EDS measurements, the spherical crystallites could be identified as the hexagonal high-quartz phase (*P*$6_2$22*)*, while the rod-shaped crystallites are assigned to an orthorhombic $ZrTiO_4$ phase (*Pbcn)*.

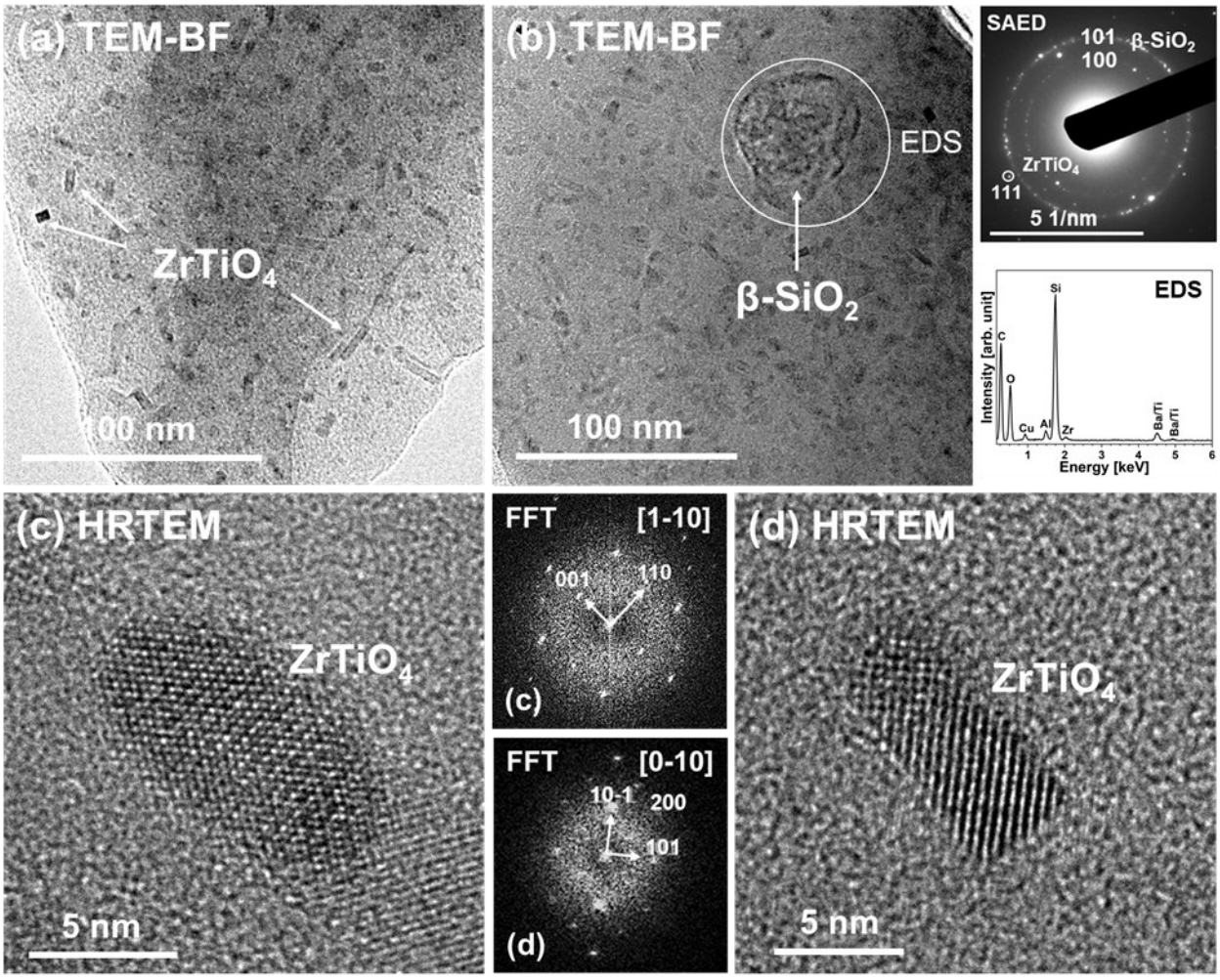

Figure 4-4. *TEM investigations on glass-ceramic samples. (a) and (b) represent TEM-BF micrographs with corresponding SAED and EDS measurements, revealing* β-SiO_2 (*P*$6_2$22) and $ZrTiO_4$ (*Pbcn*) crystallites *in a glassy matrix, while HRTEM images (c) and (d) reveal nanosized* $ZrTiO_4$ *crystallites in* [1-10] *and* [0-10] *orientation. Own work, reproduced from [163].*

In particular, the presence of high-quartz is in accordance with PXRD analyses, where it could already be identified as the predominant LAS phase, with a corresponding crystallite size of about 70 nm, according to estimates based on the Scherrer equation. In contrast to corresponding PXRD measurements (see inset in Figure 4-1 (a)), where a strongly broadened diffraction peak appeared due to the comparatively small crystallite size, the $ZrTiO_4$ phase could only be unambiguously identified via TEM in combination with SAED patterns and HR-TEM imaging. Moreover, the presence of orthorhombic $ZrTiO_4$ correlates well with the work of Kleebusch et al. [164], who recorded similar nanoscale crystallites and simultaneously provided the first evidence of epitaxial overgrowth of a LAS phase on $ZrTiO_4$ via TEM; a phenomena which was not observed in the present sample. At this point, it should be noted that high-quartz crystallites are quite sensitive to amorphization upon electron irradiation and were consequently difficult to image during TEM examination. $ZrTiO_4$ nanocrystals are much more robust to radiation damage, thus HR-TEM imaging revealed their actual geometric shape and size. In general, Ti and Zr oxides are known for their high physical and chemical stability, especially under alkaline conditions. Therefore, it is expected that they do not change significantly during mechanochemical treatments and also do not contribute to zeolite formation.

Short Summary - Characterization of the Feed Materials

- **Chemical Characterization**
  - ICP-OES analysis revealed Li_2O contents of 4.52; 5.16; 5.61 and 7.32 wt% for the glass-ceramic, petalite, lepidolite and spodumene samples, respectively, in addition to their main elements silicon and aluminum.
  - Especially the glass-ceramic sample had a more complex composition, including significant amounts of BaO, TiO_2, ZnO and ZrO_2, which are necessary to tailor the microstructure and characteristic properties of this material during the manufacturing.
- **Structural Investigations**
  - PXRD measurements indicate a high quartz-phase ($LiAlSi_2O_6$) as the main component in the glass-ceramic sample, while lepidolite, spodumene and petalite were identified as lithium-bearing phases in the mineral samples.
  - In addition, minor phases were present such as beta-spodumene (β-$LiAlSi_2O_6$) in the glass-ceramic specimen, or cogenetic phases including low-quartz or analcime in the petalite samples.
- **Microscopic Examinations**
  - OM and SEM both show distinct variations in particle morphology, suggesting irregularly shaped glass-ceramic particles without any preferred orientation, while investigations on the mineral samples revealed platelets of lepidolite or petalite and rod-shaped particles of spodumene, which is attributed to their specific crystallographic properties.
  - In addition, OM, SEM, and SEM-EDS indicate homogeneous and unaltered samples, without any interfering particles or major impurity phases, which is consistent with the earlier PXRD studies, revealing pure feed materials.
  - Finally, the microstructure of the LAS sample was examined using TEM, whereby, in addition to the already known high quartz phase, nano-sized $ZrTiO_4$ crystallites could be detected in a glassy matrix.

4.2 Mechanochemical Treatments of LAS Glass-Ceramics

The beneficial role of mechanochemical routes in the synthesis of various compounds, the solution of environmental problems or the recovery of metals from primary and secondary resources has already been demonstrated by various researchers in the past (see chapter 2.1). Most important for this work is the application of mechanochemistry in the hydrometallurgical context, where this approach is generally utilized to improve the reactivity and leaching kinetics of refractory phases, which usually require rather harsh leaching conditions such as autoclaving at high pressures and temperatures.
In the following chapter, the results of the mechanochemical treatments on LAS glass-ceramic samples at various parameters are presented, while focusing on the decomposition of the parent high-quartz phase in parallel to lithium enrichment within the leaching liquor and the formation of zeolite byproducts in the residues. Some of these results were published in [23]; while the entire achievements including further experimental and analytical investigations are discussed in the following.

4.2.1 Experimental Results at Various NaOH Concentrations and Reaction Times

In general, the reaction time and the concentration of the leaching agent can be considered as crucial parameters in hydrometallurgical leaching experiments. Therefore, the NaOH concentration was varied between 1 and 9 mol/L at reaction times of 30, 60 and 120 min during the mechanochemical treatments, to evaluate the effects of these fundamental parameters in the context of lithium extraction (see Figure 4-5 (a)) and phase decomposition (see Figure 4-5 (b) to (d)). During these studies, other experimental parameters such as rotational speed and the ball-to-powder ratio (BPR) were kept constant at 600 rpm and 50 g/g, respectively. During the first series of experiments, the samples were milled at different concentrations for 30 min each, with a generally low lithium recovery (< 38 %) and no clear trend that could be observed. In contrast, much higher yields were determined when the samples were treated for 60 or 120 min in alkaline solutions. Regarding the data for the 60 min experiments, a clear trend became visible, with an increased lithium extraction with rising concentration for the range of 1 mol/L (43.0 %) to a maximum reached at 7 mol/l (83.8 %). A further increase in concentration to 9 mol/L (81.8 %) did not contribute to an increased yield. Considering an extended reaction time of 120 min, the experiments show the lowest yields at 1 mol/L, while a plateau of promising lithium extraction values was reached for the concentration range from 3 to 9 mol/L, which reached its maximum at 9 mol/L (93.4 %). In addition to the chemical analysis of the leaching liquid, the temperature of the reactor was also assessed as an important factor, resulting in relatively uniform values of around 88 ± 5 °C, although the 30-min reaction time tended to give slightly lower temperatures.
Upon mechanochemical treatment, leaching residues were analyzed by PXRD to monitor structural changes such as the degradation of the lithium-containing high quartz-phase. In this regard, PXRD examinations of the 30-min samples treated with different NaOH concentrations (see Figure 4-5 (b)) confirmed the presence of the high-quartz phase as the starting material in all samples, while no evidences of other phases were observed. Similarly, the diffraction peaks of the high quartz-phase remained unchanged during 60 min (see Figure 4-5 (c)) of ball milling in combination with NaOH solutions of 1 and 3 mol/L, while the first significant changes in the diffraction patterns occurred at 5 mol/L, revealing the formation zeolite A (LTA; $Na_{95}(H_2O)_{39}[Si_{96}Al_{96}O_{384}]$) with cubic space group (*Pm*-3) besides the parent phase. In addition, a further increase in NaOH concentration to 7 or 9 mol/L is associated with the formation of hydrosodalite (SOD) with cubic space group *Im*-3*m* and zeolite N (LTN; $Na_{384}(H_2O)_{394}[Al_{384}Si_{384}O_{1536}]$) with space group *Fd*-3*m* in the residues, while in parallel the peaks of the parent high-quartz phase became significantly weaker.

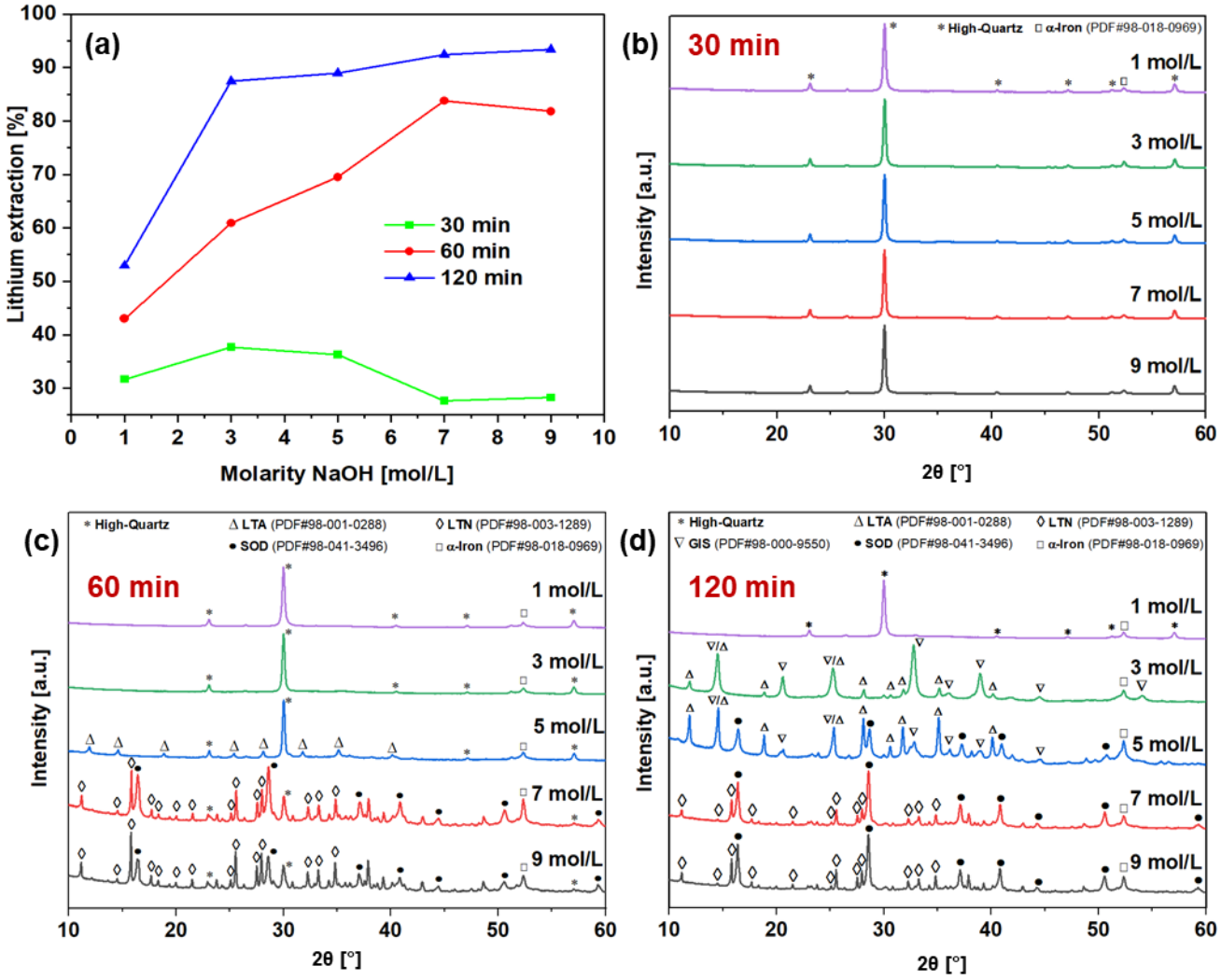

Figure 4-5. *(a) Effect of NaOH concentration and reaction time on the lithium extraction. Corresponding PXRD patterns of the leaching residues obtained after mechanochemical treatments for (b) 30 min; (c) 60 min and (d) 120 min at various NaOH concentrations in the range of 1 to 9 mol/L. During these investigations, the rotational speed and BPR were kept constant at 600 rpm and 50 g/g. Own work, reproduced from [23].*

Finally, diffraction patterns of leaching residues obtained after 120 min of milling were recorded (see Figure 4-5 (d)). Being consistent with the experiments performed for 30 and 60 min, prolonged treatment for 120 min at a concentration of 1 mol/L did not contribute to a degradation of the parent phase. Unexpectedly, this behavior changed abruptly when concentrations of 3 mol/L or higher were reached, leading to a complete transformation of the high-quartz phase into various zeolite frameworks. At a concentration of 3 mol/L, the PXRD reveals the presence of zeolite P (GIS; $Na_6(H_2O)_{12}[Si_{10}Al_6O_{32}]$) with tetragonal symmetry (space group $I4_1/amd$) as the main phase, accompanied by smaller amounts of LTA, while with a further increase to 5 mol/L LTA became dominant alongside small amounts of GIS and SOD. Upon reaching the highest concentrations of 7 and 9 mol/L, the diffraction patterns changed once again, with SOD becoming the main phase accompanied by small amounts of LTN, while the diffraction peaks of GIS and LTA disappeared completely. Repeating the experiments resulted in identical phase compositions, while only subtle differences in peak intensities were observed in the diffraction patterns, attributable to slightly different mass fractions of the zeolite phases within the analyzed specimens.
In summary, the zeolite species being present in the leaching residues are strongly dependent on the alkalinity of the solution, which is in general consistent with the results of hydrothermal zeolite synthesis [165,166]. In

this context, Subotić et al. [165] demonstrated the conversion of various frameworks such as GIS to LTA and LTA to SOD with an increase in NaOH concentration. Furthermore, he reported for the transformation from LTA to SOD a conversion mechanism involving the dissolution of the parent LTA phase in caustic media, and the formation of primary SOD particles from a supersaturated solution, growing with increased reaction time. A similar reaction was reported by Peng et al. [166] while studying desilication products of the Bayer process, revealing the occurrence of LTA at 2 mol/L, a mixture of LTA, SOD and LTN at 4 or 6 mol/L and mainly SOD with LTN at 8 mol/L NaOH. Moreover, the observed results with GIS-type frameworks being present at 3 mol/L and the formation of SOD at 5 mol/L could also be confirmed Lee et al. [122], who obtained these zeolites as byproducts during regular alkaline leaching of glass-ceramic samples (see also chapters 2.3.5).

In addition to the PXRD studies, the different zeolite frameworks obtained in the leaching residues as a function of NaOH concentration are shown in Figure 4-6, while structural details are summarized in Table 4-2. Accordingly, GIS and SOD have a comparatively straightforward structure, as they each consist of only one specific cage type, such as *gis* and *sod*, respectively, both of which are named after their parent phase. In contrast, the LTA and LTN structures are much more complex, consisting of three (*d4r, sod* and *lta*) or even four (*d6r, can, sod* and *lta*) different cage types. Nevertheless, the structures obtained show important similarities, such as the presence of *sod* cages as a structural unit in LTA, SOD and LTN zeolites.

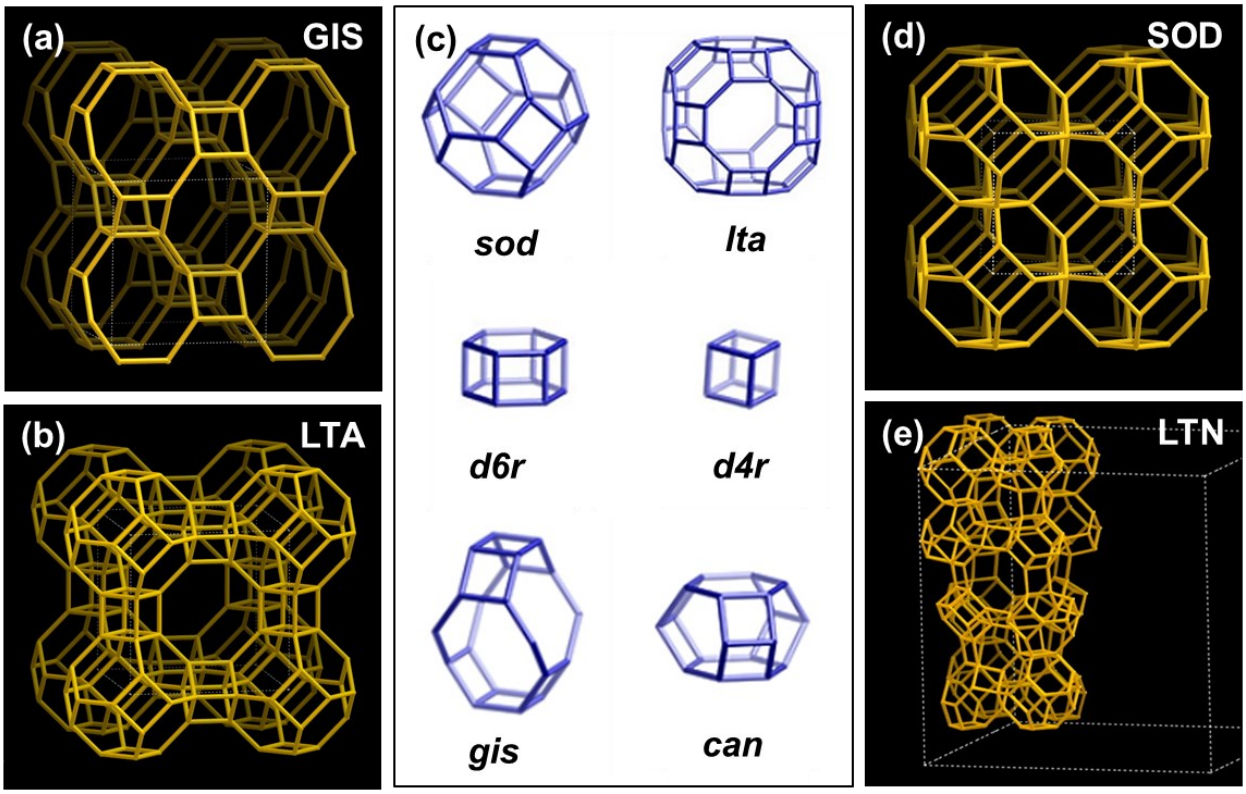

Figure 4-6. *Zeolite frameworks being present in leaching-residues such as (a) GIS, (b) LTA, (d) SOD, (e) LTN, while (c) reveals the building units of these structures. Note that the frameworks and building units are simplified representations of the structures focusing on the bonding of aluminum and silicon, while oxygen atoms and metal ions (e.g., Na^+) are not shown for better illustration. Therefore, the corners of the polyhedra represent a silicon or aluminum atom, while each polyhedron edge symbolizes a Si-O-Al bond. Figures reproduced from Baerlocher and McCusker [167].*

Table 4-2. *Structural details on relevant zeolite frameworks, obtained during mechanochemical treatments of LAS glass-ceramic samples. Data derived from [167].*

Framework	a (Å)	b (Å)	c (Å)	Space Group	Building Units
GIS	9.80	9.80	10.15	$I4_1/amd$	*gis*
LTA	11.91	11.91	11.91	*Pm*-3*m*	*d4r, sod, lta*
SOD	8.95	8.95	8.95	*Im*-3*m*	*sod*
LTN	35.62	35.62	35.62	*Fd*-3*m*	*d6r, can, sod, lta*

Besides the different types of zeolites occurring in the leaching residues, PXRD investigations also revealed traces of iron in the ball-milled samples, attributable to slight abrasion of the grinding balls during milling. However, due its insolubility at alkaline pH, iron remained in the residue and had no significant effect on the downstream processing of the leaching liquor.
While evaluating the mechanochemical treatments, the 60 min experiments using 7 mol/L NaOH, yielding in a rather high extraction yield of 83.8 %, can be considered as most effective, since a doubling of time to 120 min resulted only in a slightly increased yield of 92.4 %. However, when the zeolite formation is taken into account, the 120-min attempts were more favorable, since the entire feed material was converted into various zeolites, while the specific species mainly depends on the NaOH concentration.

4.2.2 Influences of Rotational Speed and Ball-to-Powder Ratio

In addition to NaOH concentration and reaction time, the influence of rotational speed and ball-to-powder ratio (BPR) on both (i) lithium extraction and (ii) zeolite formation were also investigated separately, while the vessel temperature was monitored accordingly as another important factor for mechanochemical reactions. For these studies, the most effective experiment from the previous section (chapter 4.2.1) was selected, which was conducted following a concentration, time, rpm and BPR of 7 mol/L, 60 min, 600 rpm and 50 g/g, respectively, with either the rotational speed or the BPR being systematically changed in certain ranges.
First, the influence of the rotational speed was investigated and evaluated. As can be clearly seen in Figure 4-7 (a), an increase in speed leads to an increase in vessel temperature, while ICP-OES measurements show a comparably low extraction yield of approximately 15 to 20 % when milling at 200 to 500 rpm. However, the Li extraction dramatically increased to 83.8 % at a rotational speed of 600 rpm, where the highest temperature of 89.5 °C was also measured. A similar trend can be observed in the PXRD patterns (Figure 4-7 (b)) of the corresponding leaching residues, where the diffraction peaks of the high-quartz phase remained unchanged at 200-500 rpm, while at 600 rpm the formation of SOD and LTN was detected, although a small amount of high-quartz still remained.

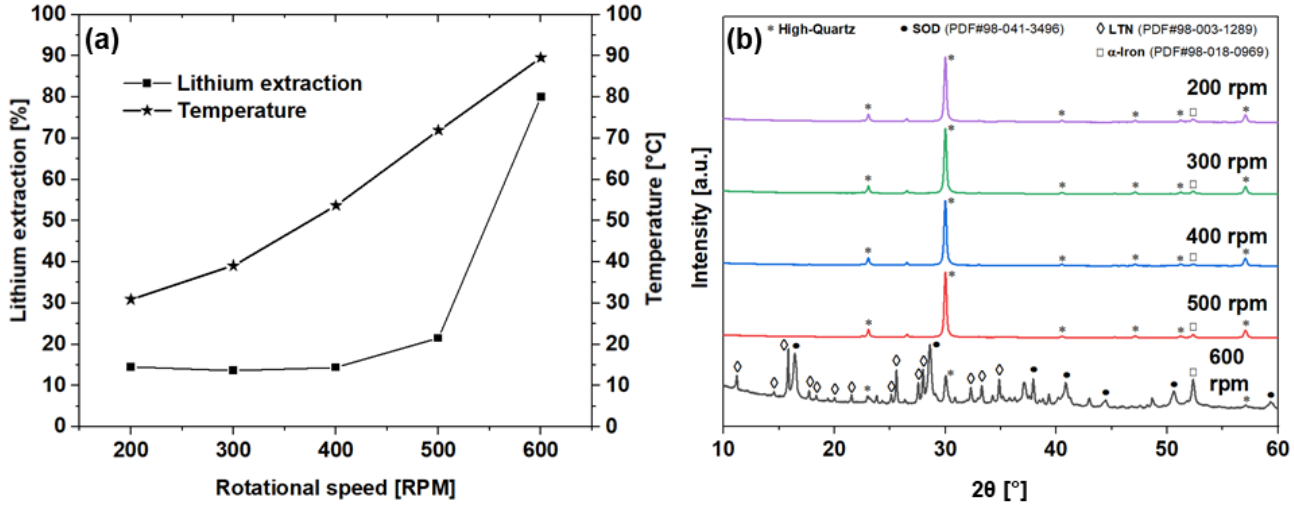

Figure 4-7. *(a) Effect of the rotational speed on the lithium extraction and the temperature during mechanochemical treatment. (b) Corresponding PXRD patterns of the leaching residues. Experiments were conducted for 60 min at different rotational speeds ranging from 200 to 600 rpm, while all other parameters were kept constant at 7 mol/L, 50 g/g, and 60 min. Own work, reproduced from* [23].

Secondly, the BPR was varied in a range from 20 to 50 g/g, while the other experimental parameters were retained. As indicated by Figure 4-8 (a) the yield of lithium extraction was rather low at BPR of 20 g/g with 17 %, reaching a vessel temperature of 62.8 °C. However, with an increase in BPR, a continuous increase in yield and temperature was observed, culminating in a significant lithium extraction of 83.8 % at a temperature of 89.5 °C, when the BPR was set to 50 g/g. In addition, the corresponding leaching residues were analyzed by PXRD (see (Figure 4-8 (b)), which confirmed the presence of the original high-quartz phase and no phase transformation at a BPR of 20 g/g. In contrast, at a BPR of 30 g/g, the first signs of zeolites appeared in the PXRD patterns, while with a further increase to 40 or 50 g/g, the diffraction peaks of SOD and LTN became more intense, which in turn correlates with the breakdown of the parent phase and the reorganization of the silicate crystal structure.

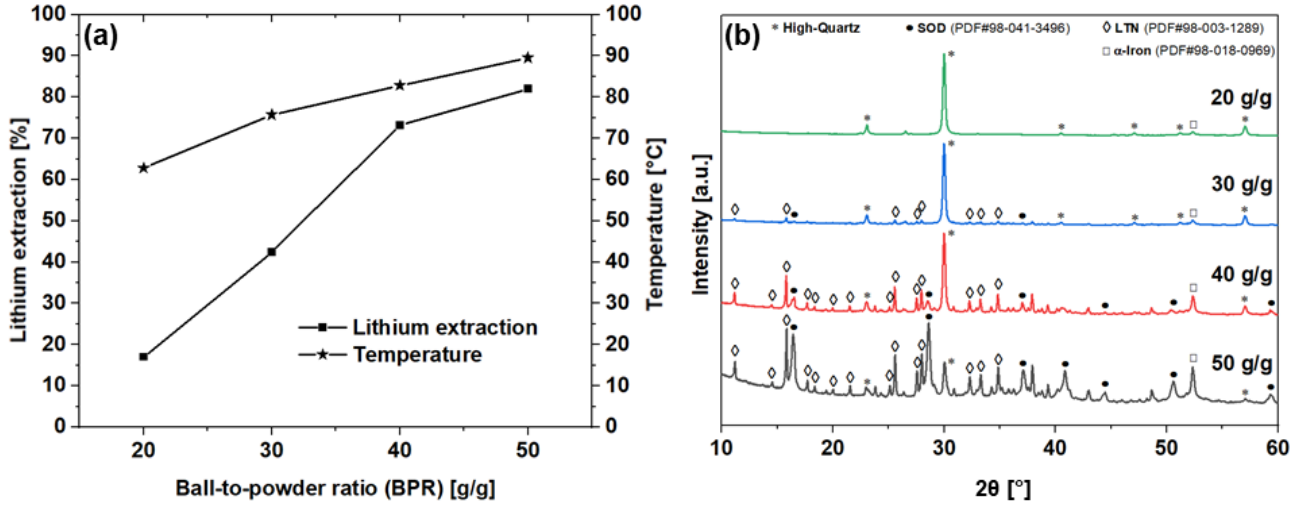

Figure 4-8. *(a) Effect of the ball-to-powder ratio (BPR) on the extraction rate and the temperature during mechanochemical treatment. (b) Corresponding PXRD patterns of the leaching residues. During this study the BPR was varied in the range of 20 to 50 g/g, while other parameters were retained at 7 mol/L, 600 rpm, and 60 min. Own work, reproduced from [23].*

To supplement the parameter range, more intensified ball milling experiments were carried out at a rotation speed of 650 rpm and a BPR of 60 g/g, with all other parameters kept constant. In terms of lithium extraction, slightly higher values of 88.6 % (650 rpm; 50 g/g) and 87.9 % (600 rpm; 60 g/g) were achieved, compared to 83.8 % (600 rpm; 50 g/g), while no significant variations were observed in the corresponding PXRD patterns of the leaching residues. Although the extraction results appear promising, increased wear of the grinding balls was observed under these rather harsh conditions, to be considered as a technical and economic disadvantage. For further discussion of wear during ball milling of lithium silicates, the reader is referred to the following chapter 4.3.6.

As confirmed by ICP-OES and PXRD measurements, increasing the rpm and BPR in conjunction with higher vessel temperatures are beneficial for both lithium extraction and zeolite formation, with most promising results obtained at 600 rpm and 50 g/g. At this stage, it was unclear whether temperature and/or intense milling were the main contributors to the observed effects; therefore, further experimental investigations such as intermittent milling (chapter 4.2.3), regular leaching (chapter 4.2.4), and reference experiments with ball-milling in water without NaOH (chapter 4.2.5) were performed to clarify these relationships

4.2.3 Intermittent Milling Experiments and the Role of Temperature

For isolating the effect of temperature on the mechanical treatment, intermittent trials were realized in which the samples were milled for 10 min followed by 10 min breaks to allow the vessel to cool. This process was repeated 12 times to achieve a total reaction time of 120 min, while maintaining the other experimental parameters. In this context, the temperature measurements show significantly lower values of 73 °C for the intermittent experiments, compared to 92 °C achieved when the samples were milled without any interruption. Contrary to expectations, the analytical studies show similar extraction rates of 90.2 % for the interrupted experiments, as compared to 92.4 % at standard conditions, while the parallel PXRD studies resulted in nearly identical diffraction patterns (see Figure 4-9), both indicating SOD and LTN as the main zeolite phases.

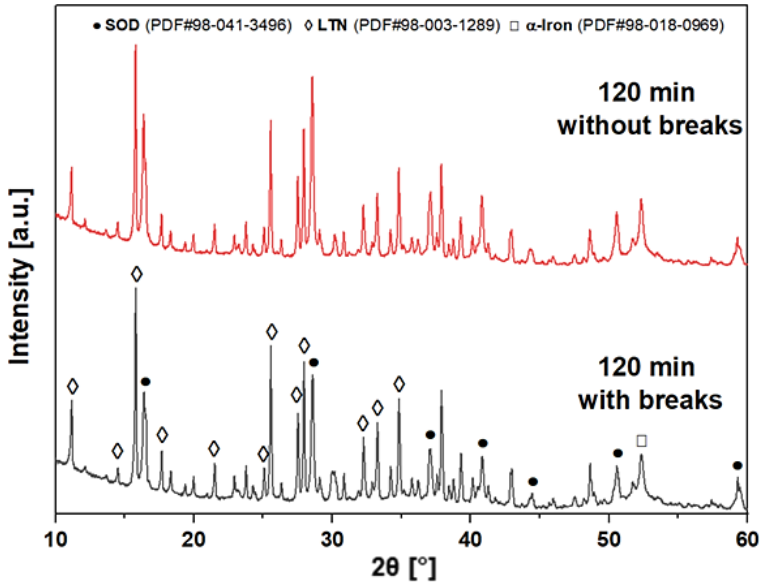

Figure 4-9. *Diffraction patterns (PXRD) of the leaching residues after mechanochemical treatment for 120 min without and with intermittence. During the intermittent experiments, 12 intervals were run, each consisting of 10 min of milling and a 10 min break for cooling, reaching a total milling time of 120 min. NaOH concentration, rotational speed and ball-to-powder ratio (BPR) are kept constant at 7 mol/L, 600 rpm, and 50:1 g/g. SOD and LTN stand for hydrosodalite and zeolite N, respectively. Own work, reproduced from [23].*

However, when comparing these diffraction patterns, subtle variations in the peak intensities were observed, attributable to slightly different mass fractions of the zeolite phases in the samples. Semiquantitative

calculations via the Reference Intensity Ratio (RIR) method revealed mass fractions of 30 % SOD and 67 % LTN in samples without breaks as well as 25 % SOD and 72 % LTN in samples with intervals, while a constant α-Iron content of about 3 % was recorded in both samples. In conclusion, the observations made during intermittent experiments indicate only a minor role of temperature, occurring as an unavoidable side effect of intensive milling.

4.2.4 Reference Experiments including Regular Leaching

To address the question of whether ball milling, which is typically associated with a pronounced reduction in particle size and partly amorphization of the crystal lattice, is essential for lithium extraction and/or zeolite synthesis, regular leaching experiments were performed. Therefore, the glass-ceramic powder was leached directly as received from the pretreatments (particle size < 500 µm), using identical parameters as those used in the mechanochemical treatments, i.e., the concentration of NaOH, time, temperature and liquid-solid-ratio were maintained at 7 mol/L, 120 min, 90 °C and 10:1 mL/g, while the suspension was stirred conventionally at 500 rpm without further intensive milling. In addition, identical experiments were carried out, but with a reaction time three times longer (for 360 min) to investigate the effects of prolonged reaction time during regular leaching. As expected, a rather low extraction yield of 8.1 % was obtained after 120 min, while significantly larger amounts of lithium (37.1 %) were extracted when the leaching time was extended to 360 min. Supporting PXRD measurements (Figure 4-10) of the corresponding leaching residues confirmed these results, as the high-quartz phase was still stable at 120 min, while after an extended treatment of 360 min the first signs of zeolites such as SOD and LTN appeared besides the parent phase in the diffraction patterns, which can be seen as an indication of the beginning degradation of the starting material. It can therefore be concluded that the leaching of lithium and the conversion of LAS glass-ceramics into zeolites generally takes place even without ball-milling, although at significantly lower conversion rates.

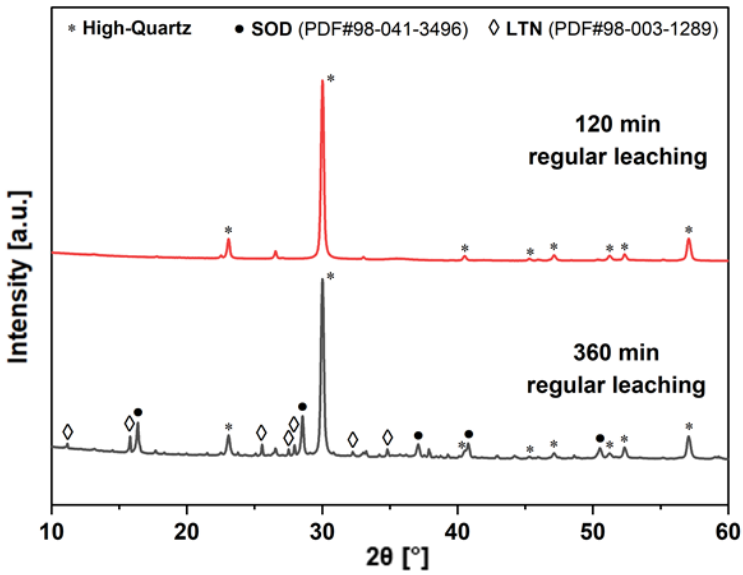

Figure 4-10. *PXRD patterns of the leach residues after regular leaching for 120 min and 360 min at 90 °C using 7 mol/L NaOH and s liquid-to-solid ratio (LSR) of 10 mL/g. Here, SOD and LTN are abbreviations for hydrosodalite and zeolite N, respectively. Only after a prolonged leaching time of 360 min the initial high quartz phase started to decompose. Own work, reproduced from [23].*

Since lithium recovery from LAS glass-ceramics has been sparsely addressed in the scientific literature (see Chapter 2.3.5), the obtained results can only be compared with the work of Lee et al. [122], who investigated a similar regular leaching approach at alkaline conditions. Comparing the leaching rates obtained in this work at 360 min (37.1 %) with those of Lee et al. (approx. 42 %), quite similar results were obtained in both approaches, when samples with similar particle sizes are considered. In addition to experiments at different NaOH

concentrations, Lee et al. also investigated different particle sizes, resulting in an extraction rate of about 70 % at optimal conditions, including a comparably long reaction time of 12 h and a fine grinding of the starting materials to a particle size of 53 µm. Unexpectedly, longer leaching up to 48 h did not lead to enhanced extraction due to the formation of core-shell particles in the leach residues (Figure 4-11), which consist of an unreacted LAS core and a zeolite P-shell (GIS framework) at 2 mol/L, as indicated by cross-sections of particles in corresponding SEM micrographs.
In particular, the formation of this type of zeolite shells, which hinder both further lithium extraction and the complete conversion of the starting material into zeolites, can be seen as a major disadvantage of regular leaching approaches. In contrast, the mechanochemical route, which combines ball-milling with simultaneous leaching, prevents the formation of these types of particles by removing reaction products on surfaces, resulting in complete conversion of the feedstock, according to the pseudo-fluid model, while the majority of the lithium passes into solution, with leaching rates of up to 93.4 % being achieved in a comparatively short time of 120 min.

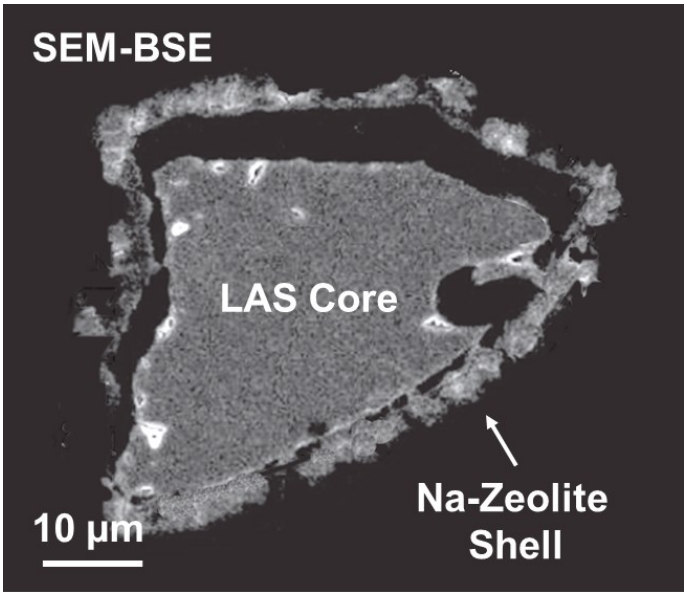

Figure 4-11. *SEM-BSE image of a particle cross-section obtained after regular leaching under optimal conditions including 12 hours reaction time at 2 mol/L NaOH. It indicates the presence of a core-shell particle consisting of a LAS core surrounded by a layer of Na-rich aluminosilicate, which has been identified as the GIS-type zeolite according to PXRD measurements on corresponding samples. Figure adapted and slightly modified from Lee et al. [122].*

4.2.5 Reference Experiments including Ball Milling in Water

Besides regular leaching, additional reference experiments were performed in which the LAS samples were ball-milled in water instead of NaOH solution to pursue changes in particle and crystallite size without chemical side reaction at similar experimental conditions.
For this purpose, the crystallite sizes were estimated via the Scherrer equation in conjunction with PXRD measurements (see Figure 4-12), while the corresponding aqueous solutions were monitored in parallel by ICP measurements. Concerning the broadening of the main diffraction peak of the high-quartz phase occurring at 29.5 °2θ, a trend of slightly decreasing crystallite sizes with an increase in milling time was observed, starting at 70 nm (feed material), followed by 60 nm (30 min), 55 nm (60 min) and 50 nm (120 min). Corresponding ICP analyses of the aqueous medium revealed lithium contents of up to 90 mg/L after 120 min of treatment, which corresponds to a negotiable lithium extraction of about 4 %. It is therefore assumed that crystallite size reduction in the glass-ceramic samples plays only a minor role in the overall mechanochemical route.

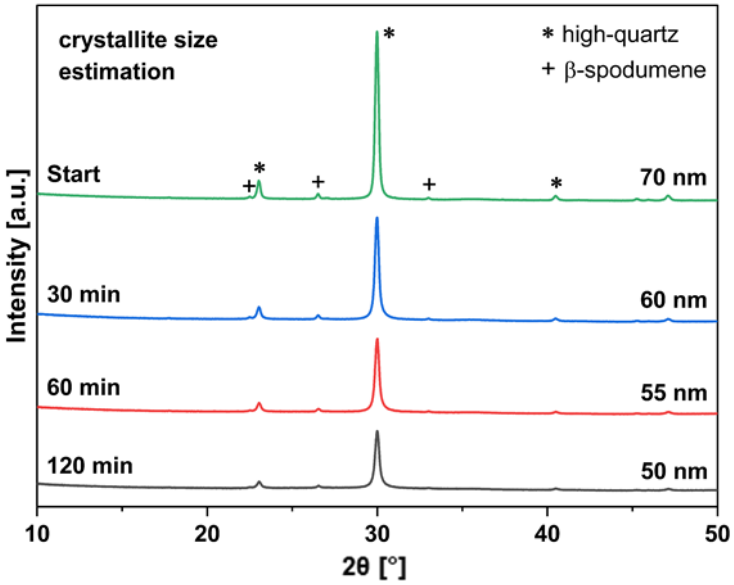

Figure 4-12. *PXRD patterns of the glass-ceramic starting material compared to samples ball-milled in water for 30; 60 and 120 min to obtain reference data without chemical side reaction. The broadening of the main diffraction peak at 29.5 °2Θ was selected to estimate variations in the crystallite size with the aid of the Scherrer equation.*

In contrast to the crystallite size estimates, laser diffraction (see Table 4-3) revealed a tremendous reduction in particle size within the first 30 min of planetary ball milling in water, resulting in a d_{50} value of 4.1 µm, considerably lower than 124.0 µm measured in the starting material. A further increase in milling time to 60 or 120 min did not lead to a significant reduction in particle size; in the 60-min sample even slightly larger particles of of 4.5 µm were observed, which are attributed to particle agglomeration during ball milling and/or sample drying. In conclusion, the highly effective particle size reduction observed in the reference experiments can also be expected during ball milling in NaOH solution and is therefore considered to be one of the main driving forces of the mechanochemical process.

Table 4-3. *Particle sizes of glass-ceramic samples in reference experiments, based on ball-milling in water instead of NaOH solution. Values were obtained from laser diffraction measurements.*

Time [min]	d_{10} [µm]	d_{50} [µm]	d_{90} [µm]
0	12.4	124.0	413.0
30	0.5	4.1	23.4
60	0.6	4.5	28.0
120	0.6	4.0	25.0

4.2.6 Structural Changes and Physicochemical Properties of Leaching Residues

For better comparison and to illustrate structural changes in the leaching residues as a function of reaction time, samples were selected that were treated with 7 mol/L NaOH under optimal conditions, including rotational speed of 600 rpm and BPR of 50 g/g while analyzing the solids via FT-IR and BET in addition to PXRD.
Regarding the PXRD studies, the data have already been presented and discussed in detail in the previous chapter 4.2.1. The result summarized in Figure 4-13 (a), reveal no significant changes in the diffraction patterns at 30 min. However, the formation of SOD and LTN zeolites were observed after prolonged ball milling for 60 min, while at 120 min the entire feed had been converted into these phases.

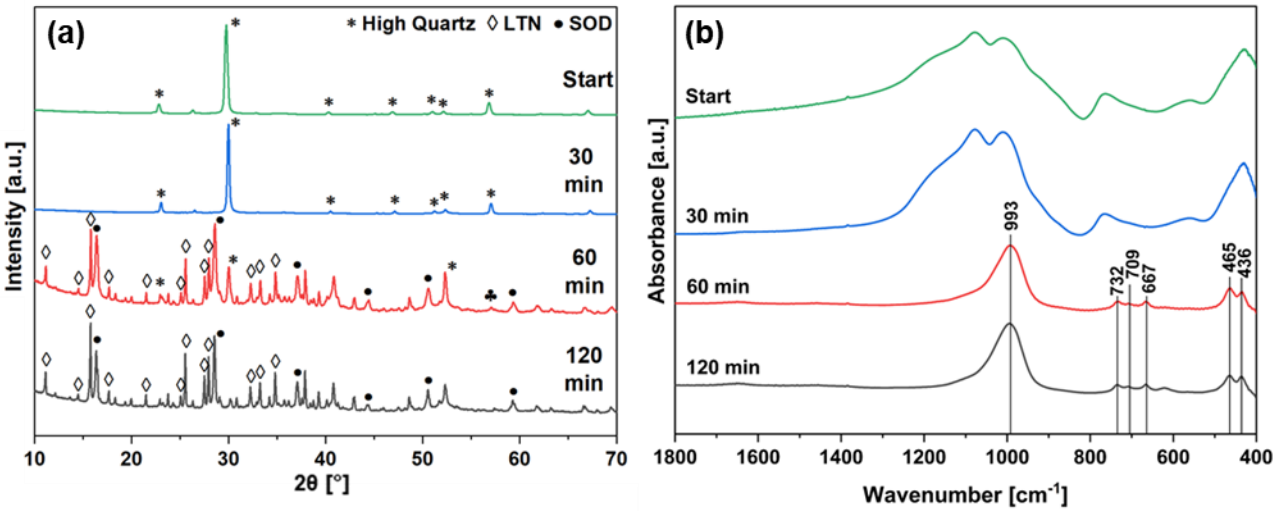

Figure 4-13. *(a) PXRD patterns and (b) FTIR spectra of the starting material compared to byproducts (leaching residues) obtained after 30; 60 and 120 min of ball-milling in alkaline solution. Experimental parameters such as concentration, rotational speed and BPR were retained at 7 mol/L, 600 rpm, 50:1 g/g, respectively. Own work, reproduced from [23,163].*

In particular, FT-IR spectroscopy was adopted complementary to PXRD measurements to evaluate changes in molecular bonding of aluminum and silicon during alkaline mechanochemical treatments. As illustrated in Figure 4-13 (b), the prominent peaks of the starting material located at 1077 and 1012 cm^{-1} remained unchanged in the 30-min sample, while they completely disappeared in the 60- and 120-min samples, which can be generally attributed to the reorganization of the molecular bonds. When comparing the spectra of the reaction products with literature data [168–171], the characteristic peaks observed at 993, 732, 709 and 667 cm^{-1}, can be attributed to Si-O-T (T = Al, Si) symmetric and asymmetric stretching vibrations of SOD, while the peaks observed at 465 and 436 cm^{-1} can be assigned to the bending of O-T-O (T = Al, Si) oxygen bridges of the same phase (see also Table 4-4). Moreover, FT-IR analysis confirms the overall tendency of the decomposition of the starting phase and parallel reorganization of the leaching residues into zeolites with increasing reaction time. In contrast to PXRD, FT-IR spectroscopy is unable to differentiate between SOD and LTN, as both structures are similar and consist of the identical building units.

Table 4-4. *Indexed absorption bands of hydrosodalite (SOD) shown in the FT-IR spectra (see Figure 4-13).*

Functional Group	Wavenumber [cm^{-1}]	Attribute	Reference
O-T-O	436	bending vibration	[170,171]
O-T-O	465	bending vibration	[170,171]
Si-O-T	667	symmetric stretching	[168,170]
Si-O-T	709	symmetric stretching	[168,170]
Si-O-T	732	symmetric stretching	[168,170]
Si-O-T	993	asymmetric stretching	[168,170]

Besides structural investigations, physicochemical properties of these leaching residues were investigated via N_2 adsorption/desorption, while BET analysis were chosen to calculate surface areas of the sample powders. As expected, the LAS feed material (particle size < 500 µm) exhibited a rather low surface area of 1.8 m^2/g, while with increasing duration of the mechanochemical treatment for 30, 60, or 120 min, significantly higher values

of 20.2, 25.2, or 29.8 m^2/g were determined (Table 4-5). The observation of increased N_2 adsorption capacity is related to the physical particle-size reduction due to intensive ball-milling (see also chapter 4.2.5), which is accompanied by an increase in the BET surface area. In addition to smaller particles, also the progressive chemical transition from a dense LAS glass-ceramic to a much more porous zeolite framework contributes to a higher adsorption capacity. Therefore, the highest BET value of 29.8 m^2/g was achieved with the longest experimental procedure (120 min), in which the entire feed material was converted into SOD and LTN zeolites. However, the obtained BET surface areas of the specimens were higher compared to similar studies by Esaifan et al., where values of 14.5 [105] or 20.5 m^2/g [172] were reached, when the SODs were prepared employing other low-cost starting materials such as low-grade kaolin or basalt powder, respectively. An explanation for this phenomenon can be seen in the different synthesis routes (mechanochemical vs. hydrothermal synthesis), which consequently led to a smaller particle size as a result of intensive ball milling during synthesis. In general, the comparatively large surface areas imply significant adsorption capacities for inorganic and organic pollutants, which was investigated separately in chapter 4.5 exemplarily for heavy metal ions in aqueous solution.

Table 4-5. *BET surface area of LAS glass-ceramic-based samples in dependency of reaction time and phase composition.*

Sample	BET Surface [m^2/g]	Main Phases
0 min	1.8	β-QTZ
30 min	20.2	β-QTZ
60 min	25.2	β-QTZ, SOD, LTN
120 min	29.8	SOD, LTN

4.2.7 SEM and TEM Investigations

Apart from PXRD and FT-IR, selected leaching residues obtained after mechanochemical treatment under optimal conditions (7 mol/L NaOH, 120 min reaction time) were further investigated by SEM and TEM. SEM-SE investigations (Figure 4-14 (a)) reveal euhedral crystals with pristine crystal faces, most probably with cubic or pseudo cubic symmetry. More detailed investigations using TEM (see Figure 4-14 (b)) generally confirmed the SEM results and, in conjunction with SAED and EDS, allowed to identify the zeolite LTN (*Fd*-3*m*), already known from earlier PXRD investigations as the main constituent of the sample.

Although the euhedral habit and pristine crystal faces of the zeolites were not expected in a ball-milled sample, the crystallization of LTN during mechanochemistry, which in this case includes ball-milling in NaOH solution, appears to be possible. Moreover, crystallization and formation of LTN during sample drying has also been discussed in the past, however a side study (not shown here) revealed identical samples concerning phase composition (PXRD) and crystal growth (SEM) despite different drying conditions, ranging from freeze-dried at -60 °C to oven-dried at 105 °C. Therefore, it can be concluded that the pristine crystallites were formed during the ball milling process at about 90 °C.

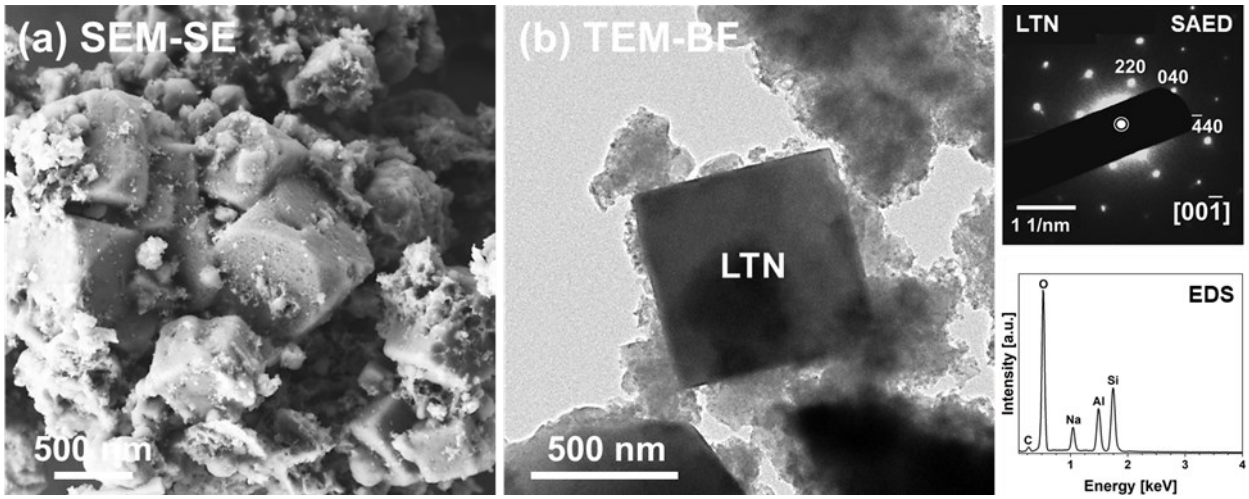

Figure 4-14. *(a) SEM and (b) TEM micrographs including localized EDS measurements of leaching residues obtained at optimum conditions (7 mol/L NaOH, 120 min reaction time), revealing the presence of euhedral crystals of LTN, which was identified via SAED in conjunction with EDS. Own work, reproduced from [163].*

Short Summary - Mechanochemical Treatments of LAS Glass-Ceramics

When summarizing the experimental results of the previous chapter, the high efficiency of the chosen mechanochemical route was most remarkable, as a lithium extraction of up 93.4 % and a complete conversion of the LAS glass-ceramic into zeolite phases were achieved under optimal parameters in a comparatively short time.

- **Mechanochemistry**
  - These investigations reveal the crucial role of reaction time, rotational speed and the BPR for lithium extraction and zeolite formation, while the most promising result were obtained at 120 min, 600 rpm and 50 g/g.
  - Important to note is the role of the NaOH, which is less important for the lithium extraction since promising results were achieved for a broad range of 3 to 9 mol/L.
  - In contrast, the NaOH concentration was determined as a crucial parameter during zeolite formation, leading to the predominant formation of GIS- and LTA-type frameworks at 3 and 5 mol/L and SOD and LTN at higher concentrations of 7 and 9 mol/L.
  - Intermittent experiments reveal a minor role of the temperature, occurring as an unavoidable side effect of intensive milling.
  - BET data on leaching residues reveal surface areas of up to 29.8 m^2/g, which can be attributed to the physical particle size reduction and to the formation of porous framework zeolites.
- **Reference Experiments**
  - Regular leaching with 7 mol/L NaOH resulted in a low extraction yield, while prolonged attempts for 3 hours resulted in a slightly higher rate of 37.1 %, with the first signs of SOD and LTN.
  - It can therefore be concluded that the leaching and zeolite formation generally takes place even without ball-milling, although at significantly lower rates.
  - Ball-milling in water under comparable conditions resulted in a slight decrease in crystallite sizes from 70 to 50 nm, while particle size analysis indicated a significant decrease from 413.0 to 23.4 µm after 30 min of ball-milling; no further changes were observed for the 60- and 120-min samples.

In summary, the beneficial role of ball milling must be emphasized when considering all of the experimental and analytical results. Accordingly, the grinding process during alkaline leaching leads to a reduction in particle size, the creation of new surfaces and the removal of reaction products such as zeolites from surfaces, which enables the almost complete extraction of lithium and an entire conversion of the starting material into framework silicates, according to the pseudo-fluid model, within a relatively short time.

4.3 Mechanochemical Treatment of Primary Lithium Minerals

The high efficiency of the chosen mechanochemical route in terms of lithium extraction and zeolite formation has already been demonstrated in the preceding chapter 4.2, focusing on LAS glass-ceramics as source material. Moreover, the transferability of this promising approach to naturally occurring lithium minerals such as lepidolite, spodumene and petalite was investigated. The alkaline decomposition of these minerals has already been investigated by several authors, typically using highly alkaline conditions in combination with autoclaves operating at high temperatures and pressures. Furthermore, mechanical activation of lepidolite and spodumene in air or water has also been investigated as a pre-treatment method prior to regular acidic leaching. Although some of these approaches have been known for decades, a mechanochemical route combining both ball milling with alkaline leaching was still lacking, which also triggered the research of this work. Several findings of these investigations were already published in [24]; however all results are discussed in detail in the following sections.

4.3.1 Lithium Recovery at Favorable Experimental Conditions

Ball milling experiments were carried out to examine whether the favorable experimental parameters of the glass-ceramic study are also advantageous for the naturally occurring lithium silicate minerals lepidolite, spodumene and petalite. These investigations involved varying the NaOH concentration between 7 and 9 mol/L and different reaction times of 30, 60 and 120 min to determine their impact on the lithium extraction rate and the formation of zeolite phases. For this purpose, other experimental influences such as rotation speed, ball-to-powder ratio, liquid-to-solid ratio, sample volume and ball size were kept constant at 600 rpm, 50 g/g, 10 ml/g, 10 g and 10 mm, respectively. To validate the leaching experiments, an extraction rate, which represents the fraction of lithium that has passed into solution, was calculated based on the ICP-OES measurements according to equation (19). The overall results of these studies are summarized in Figure 4-15, highlighting significant variations in extracted lithium among the three minerals assessed under the same experimental conditions.

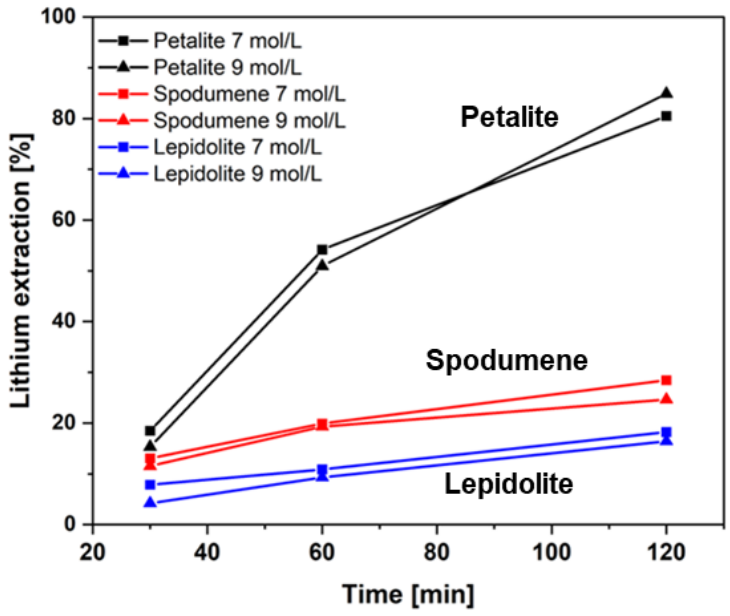

Figure 4-15. *Recovery rates for lithium extracted from the minerals petalite, lepidolite, and spodumene at different reaction times using 7 or 9 mol/L sodium hydroxide solution. Own work, reproduced from [24].*

Generally, the recovery was lowest when lepidolite was employed, although the recovery rate increased slightly with reaction time, reaching a maximum of 18.2 % at 120 min using 7 mol/L NaOH. A similar trend was observed

for spodumene, although a slightly higher recovery rate of 28.4 % was attained with the same experimental settings. The application of petalite surprisingly resulted in significantly higher leaching rates when compared to the attempts with lepidolite and spodumene. Although only a slightly higher rate was achieved at 30 min, this changed considerably at reaction times of 60 and 120 min, with recovery rates of 54.1 and 84.9 %. For the influence of the concentration on the Li-extraction no clear tendency was recognized, as there were only slight deviations between the tests with 7 and 9 mol/L, regardless the sample material.

4.3.2 Structural Changes and Physicochemical Properties of Leaching Residues

In addition to ICP-OES focusing on liquid samples, the corresponding leaching residues were evaluated by means of PXRD, FT-IR, SEM and BET to reveal structural, morphological and physicochemical changes due to ball milling in alkaline media.

To monitor the degradation of the lithium-containing phases as an effect of the mechanochemical treatment, PXRD was chosen to determine possible changes in the crystal structure. The diffraction patterns obtained are shown in Figure 4-16 and Figure 4-17 whereby the focus is only on the results at 7 mol/L NaOH, as there were only subtle variations between the two sodium hydroxide concentrations examined.

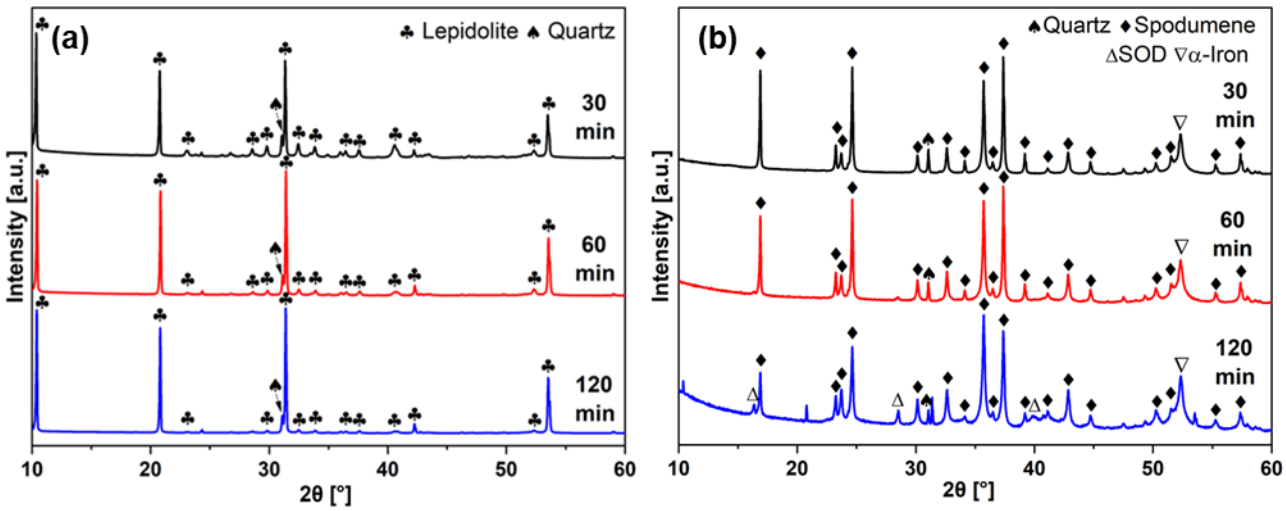

Figure 4-16. *PXRD patterns of the leaching residues based on lepidolite (a) and spodumene (b) after mechanochemical treatment using 7 mol/L NaOH solution at different reaction times. Own work, reproduced from [24].*

As can be clearly seen in Figure 4-16 (a), no significant changes such as the formation of new phases can be observed in the lepidolite samples during the ball milling experiments carried out for up to 120 min, thereby confirming the stability of this phase under the chosen parameters. Similarly, no notable changes in the diffraction patterns were observed for spodumene (see Figure 4-16 (b)) milled in alkaline media for 30 or 60 min. However, this changed when the reaction time was extended to 120 min, when the first indications of hydrosodalite (SOD) appeared as a reaction product, considered to be the first sign of decomposition of the mother phase.

When the petalite samples were subjected to PXRD shown in Figure 4-17 (a), the formation of hydrosodalite was evident after only 60 min of treatment, while the corresponding diffraction peaks became considerably more intense with extending reaction times up to 120 min. Therefore, it can be concluded, that intensive ball milling in alkaline media led to a progressive decomposition, restructuring and conversion of the petalite phase into a zeolite framework, whereby a considerable proportion of lithium of up to 84.9 % was concentrated in the

solution at 120 min. On closer inspection of the diffraction pattern, small remnants of petalite were still present even after 120 min, indicating an incomplete transformation of the feedstock. In addition, traces of quartz and analcime were present, attributable to inhomogeneities in the natural starting material, as they were already recognized prior to the mechanochemical treatments (see Figure 4-1 (d)).

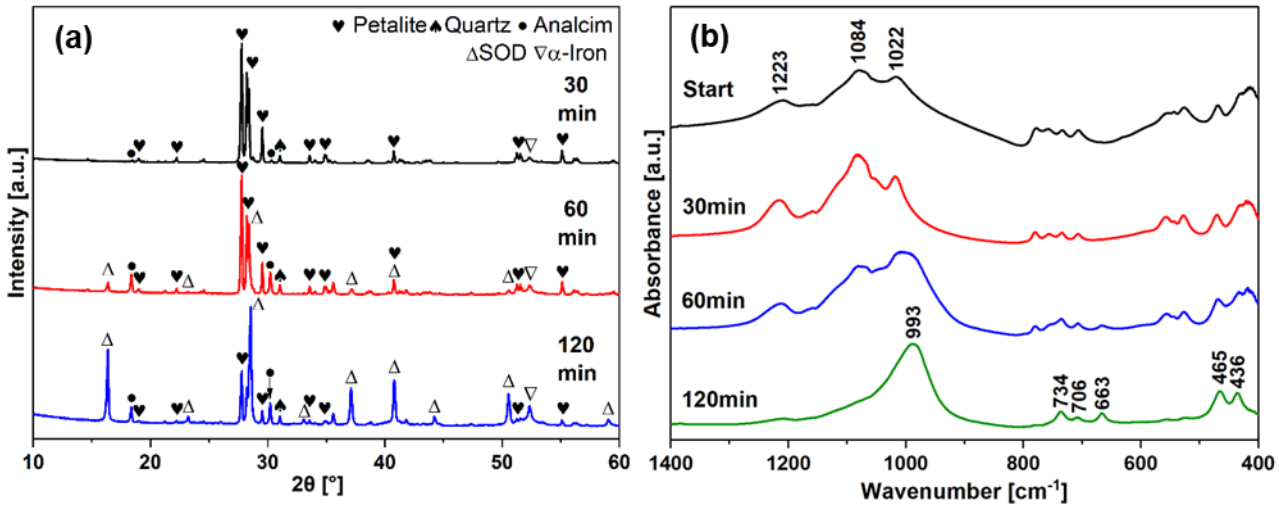

***Figure 4-17**. (a) PXRD patterns and (b) FT-IR spectra of petalite based leaching residues after mechanochemical treatment using 7 mol/L NaOH solution at different reaction times. Own work, reproduced from [24].*

Regardless of the source material, a slight decrease in the intensity of the main diffraction peaks was observed in the lepidolite, spodumene and petalite samples, which can be attributed to a reduction in crystallite size as a result of the intense ball milling process. In addition to the phases already identified, a diffraction peak around 52.3 °2θ was observed in petalite and spodumene samples, indicating the presence of minor amount of alpha iron, attributable to a certain wear of the grinding balls caused by the comparable abrasive silicates. As a result of distinct variations in Mohs hardness (see Table 2-2), the alpha-iron peak was missing in the lepidolite samples with the lowest hardness and most pronounced in the spodumene specimens with the highest hardness of 6.5-7.5, leading to a comparably severe wear of the grinding equipment during the milling experiments. However, the iron content in the leaching residues had no effect on the downstream processing of the leaching liquor, since iron is insoluble at high pH values.

Structural changes, as revealed by PXRD measurements, require changes in the molecular bonding of aluminum and silicon. Therefore, FT-IR spectroscopy was chosen as a complementary method to monitor the treatment of petalite samples with 7 mol/L NaOH solution at constant milling parameters for different times. The results are illustrated in Figure 4-17 (b), where no relevant variations in the FT-IR spectra were recorded in the 30-min sample compared to the starting material before grinding. With an increase in the reaction time to 60 min, the first changes occur in the 1000 cm^{-1} range, while the characteristic stretching vibrations of petalite at 1223, 1084 and 1022 cm^{-1} disappeared after 120 min, indicating a structural reorganization of the molecular bonds. Additionally, the newly formed peaks could be assigned to a sodalite phase, which is characterized by its distinct Si-O-T (T = Al, Si) stretching and bending vibrations at 993, 734, 706 and 663 cm^{-1} besides the bending of the oxygen bridges at 465 and 436 cm^{-1}. Overall, the FTIR spectra acquired for petalite- and hydrosodalite-rich samples are in good agreement with literature data (see Table 4-4) and further support the PXRD results, both of which indicate a decomposition of the petalite structure and a conversion to a sodalite framework with progressive ball milling in alkaline solution.

The microstructural investigations by SEM including EDS measurements focused on the petalite-based leaching residue after 120 min to determine the size, morphology, distribution and local chemistry of the crystallites. The SEM-SE images in Figure 4-18 (a) and (b) reveal the presence of intergrown isometric crystals with a size of about 200 to 800 nm, characterized by a pronounced dodecahedral habit and chemically composed mainly of Na, Al, Si and O according to semi-quantitative SEM-EDS analysis.

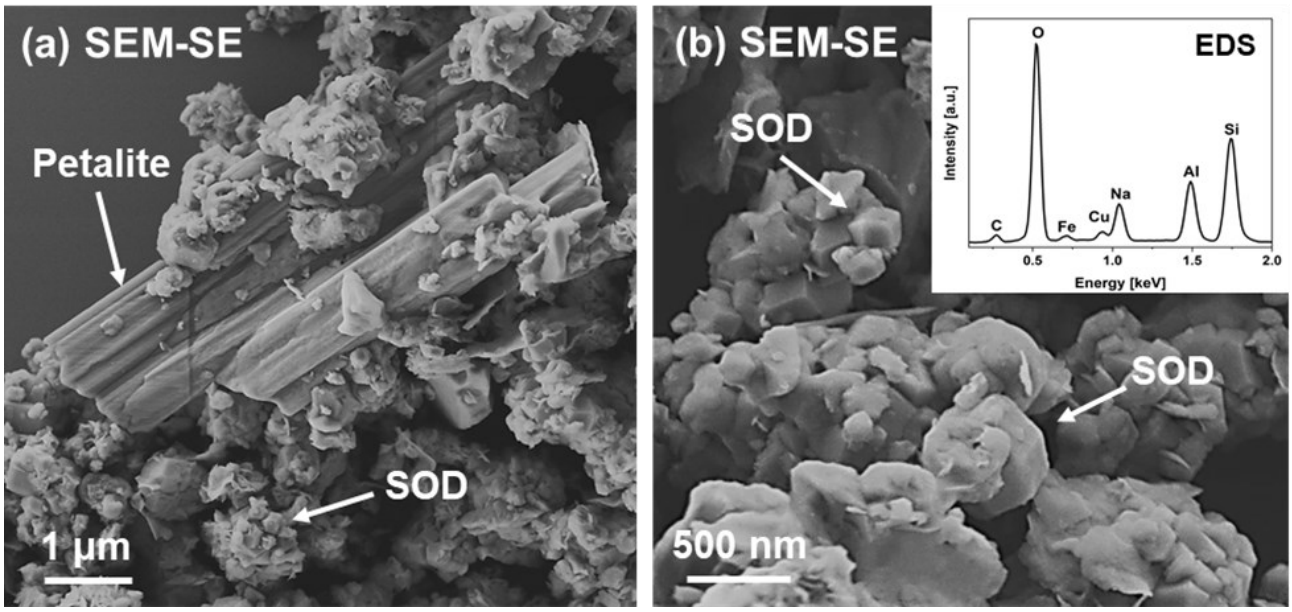

Figure 4-18. *SEM-SE micrographs of petalite based leaching residues obtained under optimal conditions (7 mol/L NaOH, 120 min ball milling). In (a) a remnant of an unreacted petalite cleavage lamella surrounded by hydrosodalite crystals is revealed, while (b) exhibits intergrown isometric hydrosodalite (SOD) crystals with a distinct dodecahedral habit. Corresponding SEM-EDS measurements (b) confirmed Na, Al, Si, and O as the main components of sodalite, while small signals of Fe and Cu originate from iron-rich fragments or sample coating. Own work, reproduced from [24].*

Being consistent with the PXRD measurements, SEM-SE imaging in association with SEM-EDS identified platelet-shaped iron-rich fragments and remnants of unreacted petalite in tiny cleavage lamellae (see Figure 4-18 (a)), however rarely observed. In particular, the morphological and chemical characteristics of these crystallites correspond well with hydrosodalite, which has already been determined as the dominant phase via PXRD and FT-IR measurements. Although the occurrence of pristine hydrosodalite crystals with euhedral habit and sharp edges was unexpected for a ball-milled sample, similar results were obtained for LTN based zeolites in chapter 4.2.7. Therefore, both cases suggest a comparatively undisturbed crystal growth during the ball milling process in alkaline media at elevated temperatures.

Changes in specific surface area caused by mechanochemical treatments on petalite samples were monitored by BET measurements (see Table 4-6) using the same samples characterized above by PXRD and FT-IR (Figure 4-17 (a) and (b)). Starting from a comparatively low BET surface area of 1.3 m^2/g in the feed material, significantly higher values of 10.3, 11.9 and 18.5 m^2/g were obtained with increasing reaction times of 30, 60 or 120 min. One explanation for the observed trend of increasing N_2 adsorption capacity with time is the reduction in particle size associated with an increase in surface area, which is particularly valid for the 30- and 60-min samples, where only minor variations were observed in PXRD and FT-IR studies. Another reason, particularly evident for the 120-min sample, is the transformation into a more porous zeolite framework, which additionally contributes to a larger surface area.

Table 4-6. *BET surface area of petalite-based samples depending on reaction time and phase composition.*

Sample	BET Surface [m^2/g]	Main Phases
0 min	1.3	PTL
30 min	10.3	PTL
60 min	11.9	PTL, SOD
120 min	18.5	SOD, PTL

When comparing the BET results obtained here with those of the glass-ceramic study, slightly different specific surface areas were observed, such as 18.5 m^2/g for petalite-based zeolites compared to 29.8 m^2/g for the glass-ceramic-based ones. The most probable explanation for the lower BET surface area of the mineral sample is attributable to the incomplete conversion of the starting material into framework silicates, as complementary methods such as PXRD (see Figure 4-17 (a)) or SEM (see Figure 4-18 (a)) revealed remnants of petalite, having a significantly lower specific surface. In addition, deviations in particle size also affect the N_2 adsorption/desorption capacity, as finer particles generally have a higher specific surface area. Specifically, this tendency was observed in reference tests with d_{50} particle sizes of 4.1 µm (glass-ceramic) vs. 10.8 µm (petalite) after 30 min of ball milling, which explains these deviations without the formation of zeolites.

4.3.3 Reference Experiments

In consistency with the study on LAS glass-ceramics, samples of lithium minerals were also involved into reference experiments based on regular leaching and ball milling in water. During regular leaching, the suspension was stirred at 500 rpm instead of being intensively ball milled, while other parameters such as NaOH concentration, time, temperature and LSR were kept constant at 7 mol/L, 120 min, 90 °C and 10:1 mL/g respectively. As expected, the proportions of lithium passing into solution were significantly lower compared to the mechanochemical tests, resulting in a limited extraction yield of 1.4 % (lepidolite), 4.0 % (spodumene) and 3.4 % (petalite). The trend of low lithium extraction was additionally confirmed by PXRD measurements on the corresponding leaching residues (data not shown), which indicated no significant changes, such as the decomposition of the parent phases.

Ball milling in water was adopted to obtain data on crystallite and particle sizes. Therefore, identical experimental parameters as in mechanochemical trials were applied, utilizing water instead of NaOH solution to avoid chemical side reactions during ball milling.

The corresponding PXRD patterns are shown in Figure 4-19, where the main diffraction peaks of lepidolite (31.361 °2θ), spodumene (37.352 °2θ) and petalite (28.237 °2θ) reveal a significant broadening, generally attributable to a decrease in crystallite size with an increase in milling time. To estimate the crystallite size, the Scherrer equation was employed, which indicated comparatively large crystallites in the starting materials and in the lepidolite sample, which clearly exceed the upper limit of the equation of around 200 nm. This observation is generally consistent with supplementary SEM investigations (see Figure 4-3), which showed large µm-sized crystals in the starting materials. Aiding the Scherrer equation resulted in a trend of decreasing crystallite sizes with time for spodumene and petalite samples. Both starting from µm-sized crystals in the feed, ball milling resulted in significant smaller crystallites of 190 nm (30 min), 140 nm (60 min) and 110 nm (120 min) in spodumene samples, while petalite specimens tended to slightly larger crystallites of 160 nm (60 min) or 150 nm (120 min). This trend towards decreasing crystallite sizes is particularly pronounced in the mineral samples, as

the initial crystallites in the µm range are comparatively large relative to those of the glass-ceramic feed material with a crystallite size as small as 70 nm in the beginning.

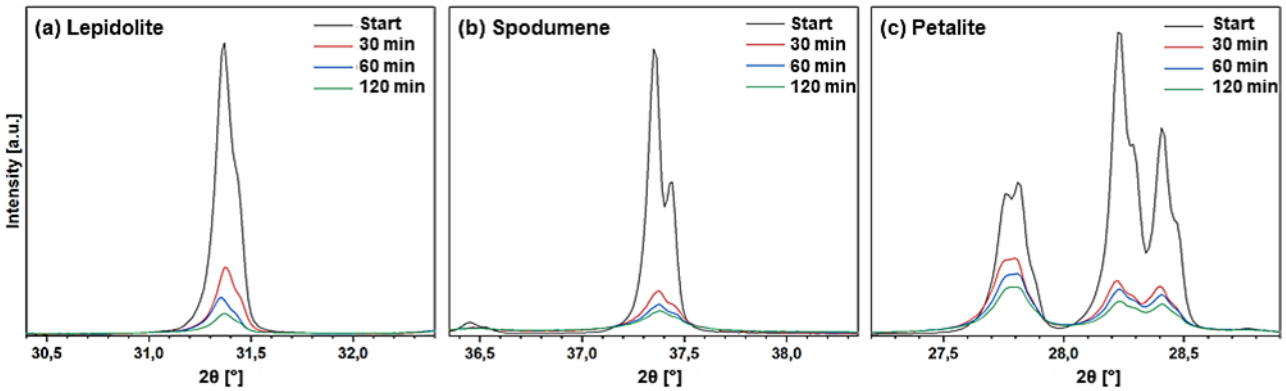

Figure 4-19. *Diffraction patterns (PXRD) of reference samples, obtained by ball milling of (a) lepidolite, (b) spodumene and (c) petalite specimens in water for different times. All samples revealed a broadening of main diffraction peaks, which was further applied for crystallite size estimation via the Scherer equation.*

In parallel, laser diffraction measurements (see Figure 4-20) show a significant reduction in d_{50} particle size for all samples within the first 30 min of ball milling, while further increasing the time to 60 or 120 min did not significantly contribute to smaller particles; a trend already observed during the LAS reference study (see chapter 4.2.5). Focusing on petalite, the initial d_{50} value of 153 µm decreased substantially to 10.8 µm after 30 min, while prolonged treatment for 60 min (9.3 µm) or 120 min (6.4 µm) resulted in only very minor changes.

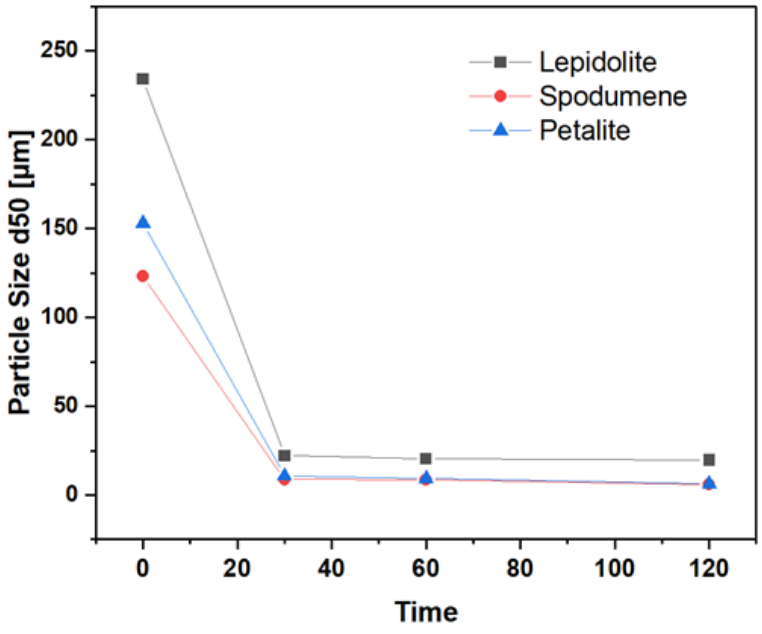

Figure 4-20. *Particle sizes (d_{50}) of reference samples, which were ball milled for various times in water. Notably these values were acquired via laser diffraction measurements on dry dispersed samples.*

In addition to analyzing the crystallite and particle sizes, the corresponding water samples were monitored using ICP-OES measurements, which indicated a negligible loss of lithium in all samples. The highest value was achieved for petalite, with up to 143 mg/L Li released into the water, representing an extraction yield of approximately 5.9 %. Although the reference data based on regular leaching and ball milling in water indicated uniform trends for lepidolite, spodumene and petalite, substantial discrepancies in lithium extraction and zeolite formation were identified during mechanochemical leaching (see chapter 4.3.1). Therefore, other

considerations need to be addressed to provide an explanation for the increased reactivity of petalite, as for example the specific crystal structures.

4.3.4 Influence of Different Crystal Structures on the Leachability of Lithium

The evaluation of the experimental results using ICP-OES, PXRD and FT-IR measurements demonstrated an effective lithium extraction is only achievable if the parent phase is successfully decomposed by intensive mechanical and/or chemical forces. Within the selected parameter range, however, this was only achieved for petalite samples, while the experiments with lepidolite and spodumene generally turned out less promising. Therefore, the crystallographic properties of lepidolite, spodumene and petalite were further analyzed in detail in order to find a conclusive explanation for the differences in leachability and reactivity. A closer look at the crystal structure at the unit cell level (see Figure 4-21) shows that lepidolite and spodumene have densely packed structures. In comparison, petalite reveal a more open three-dimensional framework structure, which is generally favorable for achieving high rates in leaching processes.

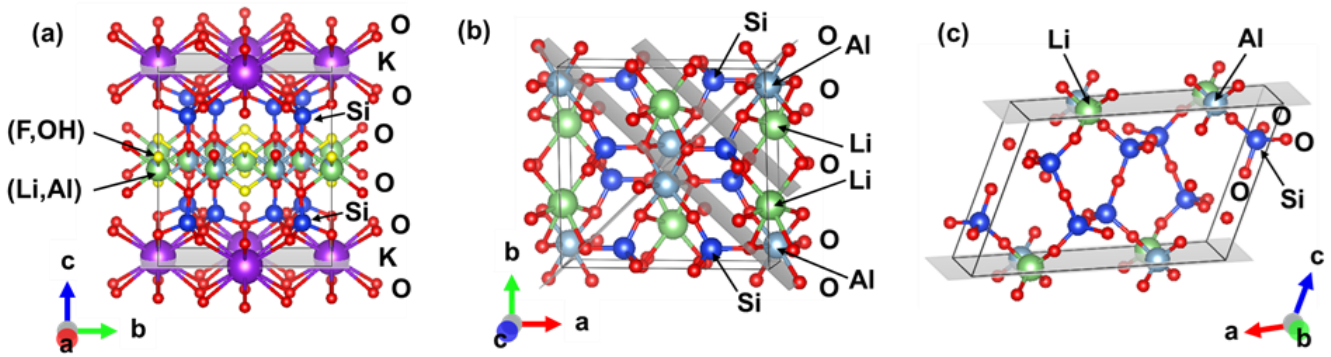

Figure 4-21. *Idealized crystal structures on the unite cell level of the investigated minerals (a) lepidolite; (b) spodumene and (c) petalite. The grayish colored areas indicate the most important cleavage planes within the structures, while the orientation of the unit cell is given next to each structure. Note that the figures were created using VESTA 3 [134] employing atomic radii.*

In addition to a lower packing density within the unit cell, the coordination of Li^+ and Al^{3+} ions in petalite are tetrahedral rather than octahedral as in lepidolite or spodumene [92,93]. Owing to the structural properties, differences in physical and optical properties have been observed, such as a lower refractive index and a lower birefringence, when petalite is compared to lepidolite or spodumene (see Table 2-2) [88–90]. These observations were further supported by atomic packing calculations by Welsch et al. [173], who calculated ionic porosities for α-spodumene and petalite according to equation (26), where V_l correlates to the total volume of all cations and anions per formula unit and V_c represents the total volume of the unit cell.

$$Z = \left(1 - \frac{V_l}{V_c}\right) \cdot 100 \qquad (26)$$

Accordingly, an ionic porosity of Z ≈ 43.5 was recorded for densely packed α-spodumene, while petalite samples showed a much higher value of Z ≈ 57.8, indicating a more open crystal structure, generally favorable for the movement of ions, such as Li^+ during leaching experiments. In addition, the value determined for petalite resembles the ionic porosity of α-quartz (Z ≈ 59.9) [174], which is known to be one of the most open silicate

structures. In addition to ionic porosity, Effenberger et al. [175] successfully substituted lithium with hydrogen by a rather harsh treatment involving concentrated H_2SO_4 at 300 °C for 90 h to prepare Li/H-exchanged petalite ($HAlSi_4O_{10}$) for structural examinations. These findings reveal a cation exchange capacity within the petalite crystal structure, which also contributes to the increased leachability of this mineral compared to lepidolite or spodumene.

In addition to packing and bonding within the elementary cell, which have already been identified as critical parameters for the release of lithium, a further contribution can be seen in the activation of cleavage planes within the mineral samples through intensive ball milling during the mechanochemical treatment. Within the layered silicate structure of lepidolite (see Figure 4-21 (a)), comparably strong bonds of Si-O and Al-O appear within the tetrahedral layer, which is in addition strongly bound to the octahedral layer. Therefore, perfect cleavage in lepidolite is restricted to the zone between the layer stacks perpendicular to (001), where the relatively large K^+ cations are located for charge balance, while the comparatively small Li^+ cations are bound to the octahedral layer, where it replaces part of the Al^{3+} [73]. Therefore, when lepidolite samples are ball-milled, delamination along the 001-cleavage plane is expected where the K sites are located. Consequently, leading to the predominantly K^+ leaching, while Li^+ cations stay captured in the octahedral layer. A trend, which was confirmed by experimental data, revealing a comparatively high leaching rate for K of 32.0 %, while at the same time only 18.2 % of Li passed into solution.

In contrast, spodumene (see Figure 4-21 (b)) exhibits an inosilicate structure consisting of parallel chains of [SiO_4]-tetrahedra and [AlO_6]-octahedra, both connected by corners and running in c-direction, while the gaps in the structure are filled with Li^+ cations [73]. Moreover, spodumene exhibits two perfect cleavages along the (110) and (1-10) directions, which intersect at an angle of 87 ° [73]. During the mechanochemical treatment, the activation of both cleavage systems is expected, leading to the disruption of several bonds. However, this effect has only a minor impact on the release of lithium, which is comparably challenging to leach as it is 6-fold coordinated in the spodumene structure. Furthermore, this assumption was confirmed by analytical data, which led to a maximum extraction rate of 28.4 % even under the most intensive operating conditions.

Petalite's crystal structure (see Figure 4-21 (c)) is discussed controversial, as on the one hand it is a three-dimensional framework of TO_4-tetrahedra (with T = Li; Al or Si), which are connected to each other via corners by sharing an oxygen atom [91,176]. On the other hand, due to the perfect arrangement of cations at certain crystallographic positions, petalite can also be classified as a layered silicate consisting of folded [Si_4O_{10}]-layers perpendicular to (001) connected by LiO_4- and AlO_4-tetrahedra [91,176]. Of particular importance is the tetrahedral coordination of Al^{3+} and Li^+ in the petalite structure [92], which distinguishes it from lepidolite and spodumene. In addition, the weakest bonds in the structure are expected to be exactly parallel to these layers and perpendicular to (001), resulting in perfect cleavage along this orientation. Similarly, to the other lithium minerals, it can also be assumed that petalite undergoes preferential cleavage along the weakest points during ball milling, which leads to the continuous formation of new sample surfaces with Li sites. Therefore, it can be summarized that the lower lithium coordination, which leads to a more open framework, in combination with the cleavage along the lithium sites during ball milling explains the higher reactivity of petalite, which leads to a high extraction yield of 84.9 % in addition to the formation of zeolites under optimal conditions.

4.3.5 Discussion of the Results in the Context of the Literature

In summary, the results obtained in this chapter demonstrate the applicability of the alkaline mechanochemical route for petalite samples, with reasonable results being attained at comparably mild NaOH concentrations of 7 mol/L. In general, these results are in agreement with the investigations on the glass-ceramic samples in chapter 4.2, although a complete conversion of the starting material into framework silicates and a slightly higher leaching rate (93.4 vs. 84.9 %) was achieved there at 120 min.
Furthermore, the extraction yield obtained for petalite can compete with autoclaving approaches using significantly higher concentrated caustic solutions of 14 to 16 mol/L NaOH in combination with CaO at an elevated temperature of 240 to 280 °C, where leaching rates of 89-94 % for lithium were achieved [104]. Furthermore, as a result of the decomposition of the mother phase, a sodium-calcium hydro silicate (Na_2O-2CaO-2SiO_2-2H_2O) was found to be formed as a byproduct in the sediments. In particular, the high caustic consumption must be assessed critically for economic and technical reasons, as up to 560 to 640 g/L NaOH was required here [104], which is at least twice as high as in the mechanochemical process, where 280 g/L NaOH was employed. Besides lithium, the compared processes also differ in their byproducts, being present in the leaching residues. For instance, Ivanenko and Pavlenko [104] obtained a sodium-calcium hydro-silicate, presumably having applications in the cement industry, while the mechanochemical residues consist of Na-rich zeolites, having a variety of applications due to their special properties in molecular sieving or selective adsorption.
In contrast to petalite, considerably less promising results were obtained for lepidolite and spodumene in the selected parameter range at comparably moderate NaOH concentrations of 7 to 9 mol/L. An explanation for this behavior was given in chapter 4.3.4, highlighting significant structural differences within the investigated minerals, such as the coordination of lithium or the activation of cleavage planes with lithium sites during ball milling. Particularly for lepidolite or α-spodumene, alkaline decomposition by high-pressure hydrothermal autoclaving is considered more promising, as it achieves higher leaching rates of more than 90 %, but requires higher temperatures of about 250 °C and strongly alkaline conditions with 400 to 760 g/L NaOH, sometimes with the addition of CaO to further improve leachability [21,22,103]. An outlook for further mechanochemical investigations on lepidolite or spodumene could therefore focus on significantly higher NaOH concentrations or thermally pretreated samples, as both are expected to improve the reactivity of these silicates.

4.3.6 Wear of the Milling Balls during Mechanochemical Experiments

Since analytical investigations via ICP-OES, PXRD and SEM measurements revealed traces or minor amounts of iron in most of the leaching residues as an unavoidable side effect of milling, the wear of the grinding balls was monitored experimentally by means of weighting before and after the trials.
Therefore, the LAS glass-ceramic powder (investigated in chapter 4.2) as well as the lithium minerals lepidolite, spodumene and petalite were evaluated, using identical experimental parameters such as 7 mol/l NaOH, a rotation speed of 600 rpm, grinding balls of 10 mm and a BPR of 50 g/g, corresponding to 500 g balls per 10 g powder. The corresponding results, calculated as wear per hour [g/h], are summarized in Table 4-7, revealing clear differences in the wear of the stainless-steel grinding balls. Generally, it is expected, that the wear during planetary ball milling rises with increasing operating time, rotational speed and ball filling level [177,178]. As these parameters were kept constant during this investigation, their contribution can be considered negligible, while the wear can be directly attributed to the abrasiveness of the sample material.

Table 4-7. *Wear of the stainless-steel grinding balls [g/h] determined during the mechanochemical treatment of various samples in comparison to their Mohs hardness. These values were experimentally acquired at identical milling parameters involving the use of 7 mol/l NaOH, rotational speed of 600 rpm, milling balls of 10 mm and a BPR of 50 g/g, corresponding to the use of 500 g balls per 10 g sample. Highlighted in red is the spodumene sample, which caused severe wear during the ball milling experiments.*

Sample	Wear of the milling balls [g/h]	Mohs hardness
LAS glass-ceramic	0.3	≈ 6
Lepidolite	0.2	2.5-3.5
Spodumene	1.2	6.5-7.5
Petalite	0.4	6.0-6.5

Compared to the total amount of grinding balls of 500 g, the wear of lepidolite (0.2 g/h), LAS glass-ceramic (0.3 g/h) and petalite (0.4 g/h) were moderate, while a significantly higher value of 1.2 g/h was determined for spodumene. As an explanation, the variations in wear using natural mineral powders derived from coarse-grained pegmatite ores can be correlated to their Mohs hardness (see Table 4-7) ranging from 2.5-3.5 (lepidolite) to 6.0-6.5 (petalite) and 6.5-7.5 (spodumene). Although the differences in hardness between petalite and spodumene appear to be small, it is important to note that the Mohs hardness scale is logarithmic and therefore implies distinct differences in hardness between these two minerals. In contrast, the low wear of the LAS glass-ceramic with a Mohs hardness of 6 is the result of the partially amorphous fabric with nanoscale crystallites of high quartz and $ZrTiO_4$.

A closer look at the literature revealed that wear is only sparsely addressed by authors investigating ball milling of lithium minerals. The only exception was found by Vieceli et al. [14], who observed a color change from purple to gray in disk-milled lepidolite samples at prolonged time, attributable to a certain degree of wear, as traces of Fe, Ni and Cr were detected during subsequent SEM-EDS analysis. In addition, studies by the same author [96] on mechanical activation by disk milling on various lithium minerals resulted in several diffraction patterns, in all of which an unspecified peak occurred, which is clearly correlated to iron as a consequence of wear.

In general, the wear and abrasion of the milling equipment have to be considered critically for economic and technical reasons. Especially since the wear can contaminate the zeolite byproduct obtained by alkaline mechanochemistry, as in this study. When ball milling is employed as a pretreatment of lithium ores prior to acid leaching, the wear affects the downstream steps immensely, as iron preferentially dissolves at low pH values and therefore additional purification steps become necessary. Although it was not examined in this study, milling balls made of ceramics such as Al_2O_3 or ZrO_2 could be considered as an alternative to stainless-steel, as both materials have excellent mechanical properties and are known to be chemically resistant.

Short Summary - Mechanochemical Treatment of Primary Lithium Minerals

In this chapter, the transferability of the mechanochemical route developed in chapter 4.2 for the treatment of LAS glass-ceramics to the three most common lithium silicate minerals lepidolite, spodumene and petalite was investigated. The findings from these experimental investigations were as follows:

- **Mechanochemistry**
  - During these investigations, significant variations in extraction were revealed for lepidolite (18.2 %), spodumene (28.4 %) and petalite (84.9 %) at the most promising experimental parameters.
  - Complementary investigations involving PXRD and FT-IR measurements showed the decomposition of petalite and its transformation into sodalite with prolonged milling in alkaline solutions, while no significant changes were observed in lepidolite and spodumene samples within the chosen range of parameters.
  - Attributable to the particle size reduction and the formation of porous framework silicates, an increased BET surface of up to 18.5 m^2/g were measured in petalite-based samples.
- **Reference Experiments**
  - Regular leaching with 7 mol/L NaOH indicated generally low leaching rates (< 5 %) for all samples, while the initial phases remained unchanged.
  - Ball milling in water revealed similar trends in crystallite and particle sizes, in particular for spodumene and petalite samples, while lepidolite tended to slightly larger particles.
- **Discussions on Crystal Structures**
  - A closer look at the crystal structures resulted in densely-packed structures for lepidolite and spodumene, while petalite consists of a more open framework, due to a tetrahedral instead of octahedral coordination of lithium and aluminum.
  - Moreover, the activation of cleavage planes along the lithium site during ball milling is also being discussed for petalite samples, strongly promoting the lithium leaching at moderate NaOH concentrations.

4.4 Hydrometallurgical Procedures on Enriched Solutions

The mechanochemical treatment of primary and secondary lithium sources, e.g., LAS glass-ceramics and petalite mineral samples, resulted in enriched solutions, as considerable amounts of lithium were extracted. For better illustration of the extraction process, the reaction proceeding during the mechanochemical treatment of the glass-ceramic sample is summarized exemplarily in equation (27), which indicates the transformation of the LAS phase (denoted by $LiAl[Si_2O_6]$) into hydrosodalite ($Na_8[Al_6Si_6O_{24}](OH)_2 \cdot 2H_2O$), while in parallel lithium and parts of the silicon ions pass into solution. Similarly, the petalite-based leaching process can be formulated according to equation (28), leading to the identical products.

$$6\ LiAl[Si_2O_6]_{(s)} + 8\ NaOH_{(aq)} + 14\ H_2O_{(l)} \rightarrow Na_8[Al_6Si_6O_{24}]\ (OH)_2 \cdot 2\ H_2O_{(s)} + 6\ LiOH_{(aq)} + 6\ Si(OH)_{4\ (aq)} \quad (27)$$

$$6\ LiAl[Si_4O_{10}]_{(s)} + 8\ NaOH_{(aq)} + 38\ H_2O_{(l)} \rightarrow\ Na_8[Al_6Si_6O_{24}]\ (OH)_2 \cdot 2\ H_2O_{(s)} + 6\ LiOH_{(aq)} + 18\ Si(OH)_{4\ (aq)} \quad (28)$$

During this procedure the leaching of silicon (represented by $Si(OH)_4$ in equation (27) and (28)) can be considered as an unavoidable side effect of using NaOH as a leaching agent. As high silicon contents in solutions pose challenges, hydrometallurgical procedures involve the desilication of the solution, being essential for the subsequent precipitation of a pure lithium compound. The alkaline solutions obtained during lithium extraction from glass-ceramic and petalite samples are comparable regarding their main components and present the same challenges, e.g., the high silicon content and the low Li-Na ratio. In the following sections, only the treatment of petalite-based samples is discussed in more detail, as the conversion of Li_3PO_4 into $LiOH \cdot H_2O$ was also investigated there, besides desilication and precipitation. In addition, the overall results for both LAS- and petalite-based solutions are briefly discussed in section 4.4.4.

4.4.1 Desilication Experiments of NaOH Solutions

Desilication became mandatory as an intermediate step, since the rather high silicon contents in leachates, generally facilitates the formation of byproducts during downstream processing. Therefore, CaO was considered a cost-effective and efficient reagent for the removal of silica from alkaline solutions. Particularly, as an earlier study by Wolf 2022 [140] highlighted several advantages of using CaO, such as a shorter reaction time, a higher desilication rate and the formation of calcium silicate byproducts, which further contribute to a holistic approach. In accordance to Xing et al. [138], who investigated desilication of similar caustic solutions, a constant temperature of 95 °C was applied, while the reaction time and the $CaO:SiO_2$ ratio were varied to investigate their influence on the desilication of the solution. Despite varying $CaO:SiO_2$ ratios from 0.6 to 1.4, the experimental results, illustrated in Figure 4-22, showed a uniform trend of significant silica removal within the first 30 min, while a prolonged time leads only to a slightly increased desilication rate, reaching a plateau at about 60 min. With respect to the CaO consumption and removal efficiency, the $CaO:SiO_2$ ratio of 0.8 is clearly favorable, as 94.6 % of the Si was already being removed after 60 min, while a slightly higher value of 95.1 %

was attained after 90 min. In addition to the high desilication rate, the selectivity of the purification approach with CaO should also be highlighted, as mainly silicon (37.8 g/L before vs. 1.9 g/L after desilication) and aluminum (0.8 vs. 0.1 g/L) were being removed, while the lithium content of the solution remained approximately constant at 2.5 g/L.

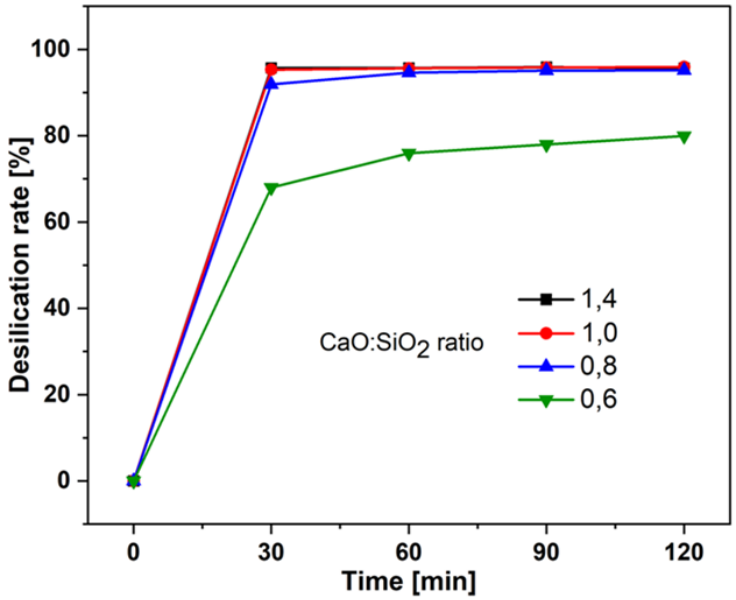

Figure 4-22. *Desilication of the Li-enriched solution became mandatory as an intermediate step prior to the precipitation of a lithium compound. Therefore, the desilication behavior of petalite-based solutions were studied at various CaO-SiO_2 ratios ranging from 0.6 to 1.4. Own work, reproduced from [24].*

Corresponding PXRD measurements on the desilication products (see Figure 4-23 (a)) reveal the predominant formation of torbermorite ($Ca_5Si_6O_{16}(OH)_2 \cdot 4H_2O$; PDF#98-008-7690) according to equation (29). Supplementary, calcite ($CaCO_3$, PDF#98-015-8248) is being present, which may have formed during sample drying (85 °C for 48 h) by the reaction of residual $Ca(OH)_2$ with atmospheric CO_2. When torbermorite samples are calcined additionally at significantly higher temperature of 900 °C for 30 min, its conversion into wollastonite ($Ca[SiO_3]$; PDF#98-020-1537) was observed in see Figure 4-23 (b) according to equation (30). In particular, wollastonite is characterized by a high melting point and a fibrous to acicular structure, which leads to numerous technical applications [179]. Therefore, this Ca-silicate byproduct is highly advantageous as it valorizes the entire route and also contributes to the holistic approach.

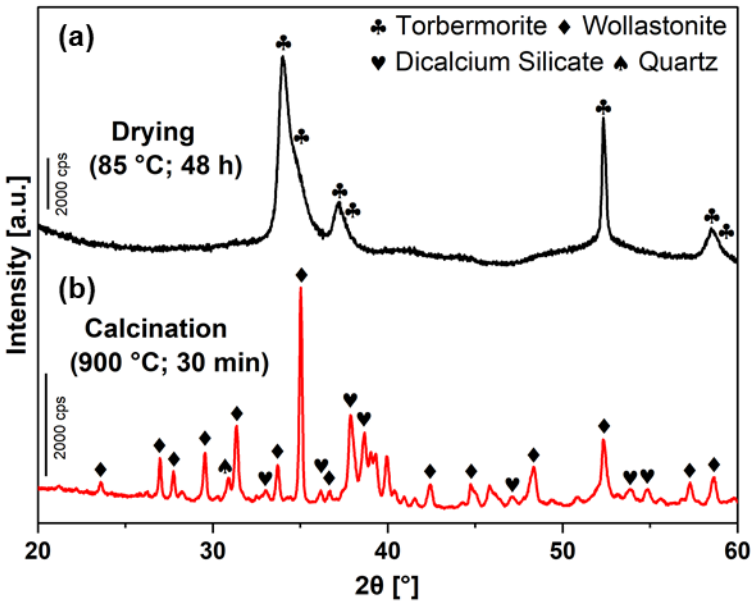

Figure 4-23*. PXRD patterns of desilication products. (a) reveals the predominant formation of torbermorite ($Ca_5Si_6O_{16}(OH)_2 \cdot 4H_2O$), while (b) indicates the conversion of sample (a) into wollastonite ($Ca[SiO_3]$) via calcination at 900 °C for 30 min. Own work, reproduced from [24].*

$$6\,Si(OH)_{4\,(aq)} + 5\,CaO_{(s)} \rightarrow Ca_5Si_6O_{16}(OH)_2 \cdot 4\,H_2O \downarrow + 7\,H_2O_{\,(aq)} \quad (29)$$

$$Ca_5Si_6O_{16}(OH)_2 \cdot 4\,H_2O_{(s)} \rightarrow 5\,Ca[SiO_3]_{(s)} + 5\,H_2O \uparrow + SiO_{2(s)} \quad (30)$$

4.4.2 Precipitation of Lithium as Li_3PO_4

The amount of lithium in the leaching liquor after leaching and desilication procedure (approx. 2.4 g/L) was still below the lower limitation for precipitation as Li_2CO_3, which requires a content of 10 g/L or more. Therefore, the precipitation of lithium as phosphate was favored, in particular since the remarkably low solubility of Li_3PO_4 (0.3 g/L) and the comparatively high solubility of Na_3PO_4 (108 g/L) allows the separation of Li^+ cations in the presence of excess Na^+ cations, as found in the NaOH solutions. In order to precipitate lithium as phosphate according to equation (17), small amounts of H_3PO_4 were added to the leachate, while the influence of different P:Li ratios ranging between 1.0:3.0 and 1.8:3.0 on the lithium recovery and phase composition were examined via ICP-OES and PXRD measurements. The analytical results, shown in Table 4-8, reveal a clear trend of increased recovery with higher amounts of H_3PO_4, with a maximum is being reached at 1.8:3.0 with 91.1 %.

Table 4-8. *Lithium recovery and obtained products using different P:Li ratios. Notably, the recoveries were calculated based ICP-OES investigations on liquid samples, while the phases present in the solids were determined via PXRD. In addition, the optimum ratio which enabled the precipitation of a Li_3PO_4 single phase is highlighted in blue.*

P:Li ratio	Li recovery [%]	Product
1.8:3.0	91.1	Li_3PO_4; Li_2NaPO_4
1.6:3.0	86.9	Li_3PO_4; Li_2NaPO_4
1.4:3.0	81.2	Li_3PO_4; Li_2NaPO_4
1.2:3.0	72.9	Li_3PO_4
1.0:3.0	76.7	Li_3PO_4; Li_2NaPO_4

However, complementary PXRD patterns (see Figure 4-24) reveal the presence of a mixed Li-Na phosphate with orthorhombic nalipoite structure (Li_2NaPO_4, space group *Pnma*) besides Li_3PO_4 at P:Li ratios of 1.4:3.0 to 1.8:3.0, indicating partial precipitation of Na in the form of a mixed phosphate. In contrast, a selective precipitation of a single phase (Li_3PO_4) was exclusively achieved at a ratio of 1.2:3.0; however, with the lowest Li-recovery percentage of 72.9 %, as shown in Table 4-8. Further investigations involved ICP-OES measurements on the single-phase sample, revealing its high purity of 98 %, while only minor contaminants such as Na and Si were present.

In general, the formation of mixed Na-Li phosphates is clearly attributable to the unfavorable low lithium-sodium ratio in the leach liquor, which has already been discussed as a challenge by various authors [23,140]. Although nalipoite-type phosphates (Li_2NaPO_4) are being considered as potential solid electrolytes in advanced lithium batteries [180], Li_3PO_4 is the preferred phase during precipitation, as it can be utilized in various ways; e.g. as a precursor for the synthesis of Li-Fe phosphate cathode materials or lithium-based compounds such as carbonates or hydroxides [142,181,182]. Therefore, the P:Li ratio of 1.2:3.0 is preferable, even if the precipitation yield of 72.9 % is comparatively low. In general, the yield is considered less critical here, as the

solution still has a high pH value, enabling its reuse for further leaching operations after adjustment with fresh NaOH, providing the great advantage of keeping unprecipitated lithium in a closed loop.

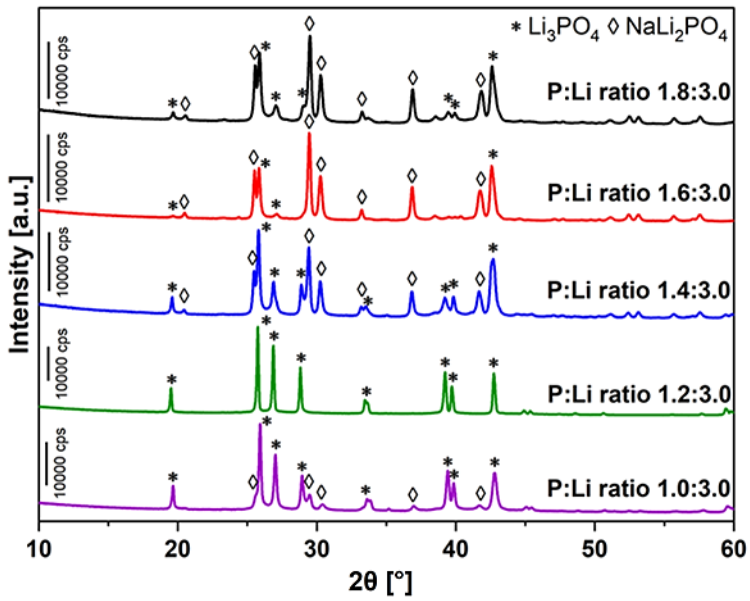

Figure 4-24. *PXRD patterns of lithium phosphates obtained after precipitation with H_3PO_4 using various P:Li ratios ranging from 1.0:3.0 to 1.8:3.0. Own work, reproduced from [24].*

Since the reuse of the alkaline solutions after phosphate precipitation was not considered in this study, reference is made to Song et al. [103], who successfully investigated the circulation of similar NaOH solutions during autoclave leaching of α-spodumene. This circulation involved the adjustment of the concentration by the addition of small amounts of fresh NaOH prior to the reuse of the solution in a secondary leaching step, resulting in stable digestion and precipitation efficiencies of 90 and 66 %, respectively, within ten consecutive cycles. Several similarities regarding the starting material and the leaching agents suggest that the promising approach of Song et al. is transferable to the solutions obtained in this work by the mechanochemical treatment of the glass-ceramic or petalite samples.

4.4.3 Transformation of Li_3PO_4 into $LiOH{\cdot}H_2O$

Subsequent to precipitation, the conversion of Li_3PO_4 into $LiOH{\cdot}H_2O$ was investigated as this compound is currently in high demand for LIB applications. Therefore, $Ca(OH)_2$ was applied due to its ability to act as a phosphate collector according to equation (18). Utilizing PXRD measurements (see Figure 4-25 (a)), this reaction was confirmed by detecting hydroxyapatite ($Ca_5(PO_4)_3OH$; PDF#98-008-1442) as the predominant phase in the precipitates next to smaller amounts of unconverted $Ca(OH)_2$ (PDF#98-007-3467). During this procedure, the lithium hydroxide initially remained in solution, while the consecutive crystallization led to the formation of $LiOH{\cdot}H_2O$ (PDF#98-003-5155), as evidenced by the corresponding PXRD pattern (see Figure 4-25 (b)).
In addition to the intended product ($LiOH{\cdot}H_2O$), small diffraction peaks of $Na_2CO_3{\cdot}H_2O$ (PDF#98-000-6293) were present, attributable to remnants of NaOH converting into $Na_2CO_3{\cdot}H_2O$ during drying. Further examination of the purity of the product by ICP-OES revealed minor impurities of Na and Ca, resulting in an overall high purity of 99 %. However, this value should be viewed with a certain degree of caution, as a carbonate species was detected in the PXRD analysis, but carbon cannot be determined with ICP-OES, so the actual purity is probably slightly lower than calculated.

Especially due to the high affinity of alkali metals for CO_2, an inert atmosphere is required during the crystallization process as well as during the analytical studies to avoid the formation of Li_2CO_3 during this final step. Besides the intend lithium hydroxide, apatite is considered a value-added byproduct in this route as it is one of the most frequently utilized sources for fertilizers [183].

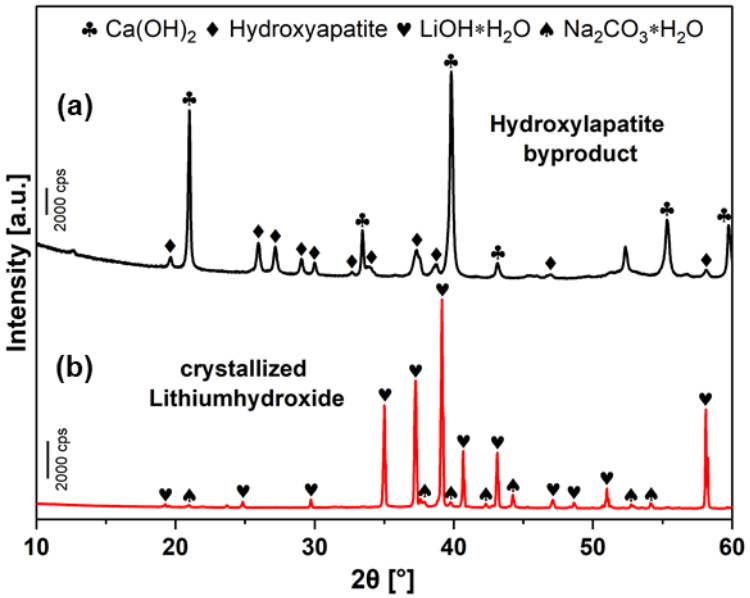

Figure 4-25. *PXRD patterns of products obtained during transformation of precipitated Li_3PO_4. (a) hydroxylapatite byproduct and (b) intended lithium hydroxide obtained after crystallization of the solution. Own work, reproduced from [24].*

4.4.4 Discussion of the Overall Results

In general, the alkaline solutions obtained during the leaching experiments based on the glass-ceramic or petalite samples are comparable in terms of their main constituents, as evidenced by similar lithium concentrations of 2.6 g/L (LAS) and 2.5 g/L (petalite), respectively. Significant differences are limited to the silicon content, as 14.8 and 37.8 g/L were present in the LAS- and petalite-based solutions, respectively, which requires different quantities of CaO during the downstream desilication process. Despite these differences, the desilication of the solutions gave uniform results, as in both cases a silicon removal of about 95 % was achieved at an optimum $CaO:SiO_2$ ratio of 0.8, while torbermorite was present as the main phase in the precipitates. In addition, precipitation with H_3PO_4 also provided comparable results, as a Li_3PO_4 single phase was obtained at an optimal P:Li ratio of 1.2:3.0 (petalite) or 1.4:3.0 (LAS). In terms of quality, the precipitated Li_3PO_4 reached a purity of > 98 % in both approaches, based on ICP-OES measurements. It is important to note that traces of carbon, which would be attributable to the formation of carbonates, are not taken into account in this type of analysis. As expected, the sample based on the glass-ceramic showed a wider range of impurities due to a more complex composition of the starting material, where Zn (0.6 wt%) is the main impurity apart from lower amounts of Na and Si, which are also present in the petalite-based phosphate. Although the comparatively low levels of impurities found in the precipitates are promising, further improvements are required to obtain battery-grade compounds, which would typically require a purity of 99.9 % or higher. As the final step, the conversion of Li_3PO_4 into $LiOH{\cdot}H_2O$ was exclusively studied for petalite-based samples, but it is assumed that this step is also achievable with the LAS-based sample.

Short Summary - Hydrometallurgical Procedures on Enriched Solutions

This chapter addressed the hydrometallurgical treatment of the enriched solutions, which became necessary to transfer the extracted lithium from the liquid stage into a solid compound. Since the alkaline solutions obtained from the glass-ceramic and petalite samples are comparable in terms of their main constituents and have the same challenges to overcome, the downstream processing was similar and involved desilication prior to the precipitation of Li_3PO_4, which was further converted to $LiOH \cdot H_2O$. The findings from these procedures were as follows:

- **Desilication of the NaOH solution**
  - Caused by the treatment with CaO, about 95 % of the silica was removed from the solution, resulting in the formation of torbermorite ($Ca_5Si_6O_{16}(OH)_2 \cdot 4H_2O$) in the precipitates.
  - Further valorization of this byproduct involved calcination, leading to wollastonite ($Ca[SiO_3]$), which has numerous applications due to its unique properties.
  - Desilication using CaO resulted in a high selectivity, as mainly silicon was removed, while the lithium content of the solution remained unchanged.
- **Precipitation of Li_3PO_4**
  - Selective precipitation of Li_3PO_4 was exclusively achieved at a P:Li ratio of 1.2:3.0, while at higher rations Li_2NaPO_4 was additionally present.
- **Transformation of Li_3PO_4 into $LiOH \cdot H_2O$**
  - Conversion of Li_3PO_4 into $LiOH \cdot H_2O$ was achieved via a treatment with $Ca(OH)_2$ resulting in the formation of hydroxyapatite ($Ca_5(PO_4)_3OH$) as a value-added byproduct.
  - Precipitated lithium salts achieved promising purities, but further improvements are required to obtain battery-grade products.

4.5 Adsorption Studies on Zeolite Byproducts

Taking into account the special properties in molecular sieving and selective adsorption, one of the classical applications of zeolites in the environmental sector is the removal of pollutants from aqueous solutions. Therefore, the adsorption behavior of the synthesized zeolite byproducts was evaluated using synthetic wastewater samples containing the divalent heavy metal ions Pb^{2+}, Cu^{2+}, Zn^{2+} and Ni^{2+}, calculating a removal efficiency for each experiment based on ICP-OES measurements as a function of zeolite dosage. On the one hand a SOD/LTN mixture, originating from mechanochemical treatment of LAS glass-ceramics, was investigated as potential adsorbent (see Figure 4-26 (a)), while on the other hand a pure SOD sample was chosen (see Figure 4-26 (b)), based on petalite as a zeolite precursor.

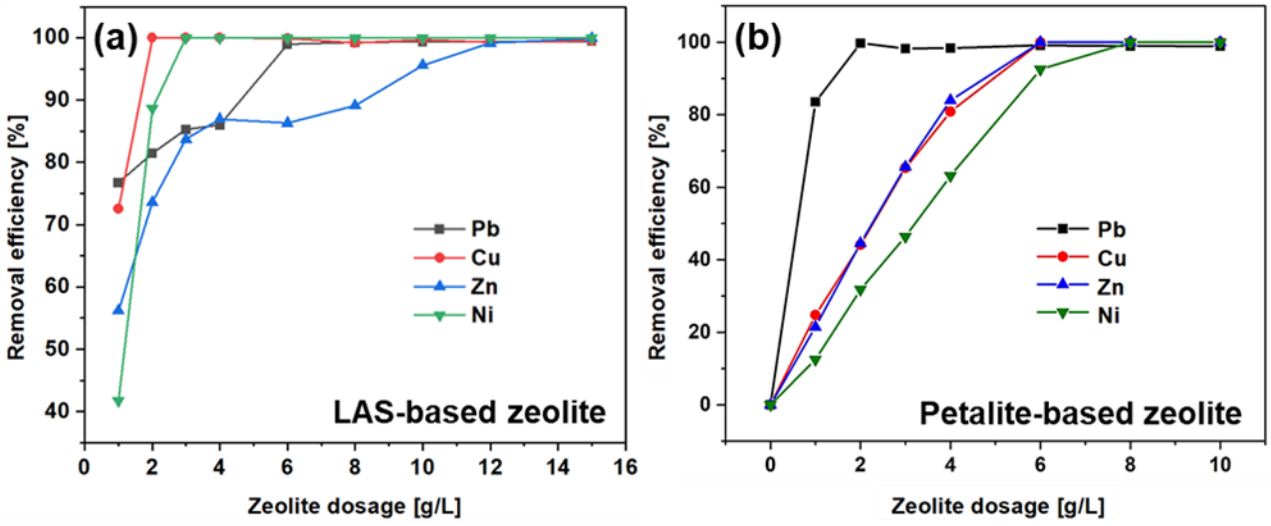

Figure 4-26. *Removal efficiency as a function of zeolite dosage (g/L) in synthetic wastewater solutions containing the heavy metal ions Pb^{2+}, Cu^{2+}, Zn^{2+} and Ni^{2+}. Here, (a) concerns the application of a SOD/LTN mixture derived from LAS glass-ceramics, while (b) shows the result obtained when SOD based on petalite was investigated.*

When the two differently composed zeolite samples were applied to the wastewater contaminated with heavy metals (100 mg/l each), a significant increase in removal efficiency was observed with rising dosage in general, as predicted. By comparing the experimental results for both series small difference became obvious, which can be attributable to the different mineral compositions of the samples (SOD/LTN mixture vs. pure SOD), since the experimental setup for adsorption studies were completely identical. Regarding the adsorption of the synthesized SOD/LTN mixture, excellent performance is shown for copper and nickel, achieving complete adsorption with only a minor amount of sorbent of 2 or 3 g/L, respectively. In contrast, to accomplish complete adsorption of lead and zinc, substantially higher dosages of 5 g/L or 12 g/L were required, although 85.3 % of the lead and 83.7 % of the zinc were adsorbed at 3 g/L. However, the pure SOD sample obtained from petalite after mechanochemical treatment, reveal an excellent sorption of Pb^{2+} with 99.7 % at 2 g/L, while much higher dosages of at least 6 or 8 g/L were required to reach almost complete adsorption of Cu^{2+}, Zn^{2+}, or Ni^{2+}, respectively.

When the results of Necke et al. 2022 [23] and 2023 [24] were compared with similar studies conducted by Esaifan et al. [105] or He et al. [143] (see Table 4-9) all of which used SOD or related zeolites at the identical dosage of 6 g/L, it became obvious that the sorption of Cu^{2+} and Pb^{2+} was generally favored compared to other

heavy metal ions, resulting in high removal efficiencies between 90 and 100 %. In particular, this phenomenon can be attributed to different ionic radii regulating the movement of the ions in the pores and channels of the zeolites. Consequently, a sorption in the order Pb^{2+} (4.01 Å) > Ni^{2+} (4.04 Å) > Cu^{2+} (4.19 Å) > Zn^{2+} (4.3 Å) would be expected based on hydrated ionic radii of the metal ions [105,143,144]. Since Ni^{2+} ions did not follow this trend, an explanation for the rather high adsorption has been found in the initial pH of the wastewater, which was considered by He et al. [143] as an essential parameter. He et al. investigated in a side study the sorption behavior of heavy metal ions as a function of pH, indicating the full adsorption potential of nickel at pH 6, although the majority of the experiments were performed at pH 5.0, where 65 % adsorption was reached at a dosage of 6 g/L. In conclusion, the initial pH value of the solutions of 5.8, which is slightly higher than 5.0 [143] or 5.5 [105], became an important factor in achieving the excellent sorption of nickel of 92 % for the petalite derived SOD sample or 100 % for the LAS based SOD/LTN mixture.

Table 4-9. *Summary of relevant adsorptions studies, including zeolite precursors, zeolite phases and a comparison of removal efficiencies [%] for divalent heavy metal ions in wastewater solutions at a zeolite dosage of 6 g/L. The own results are highlighted in blue.*

Reference	Zeolite Precusors	Zeolite Phases	Initial pH	Pb^{2+} [%]	Cu^{2+} [%]	Ni^{2+} [%]	Zn^{2+} [%]
He et al. 2016 [143]	fly ash	unspecified	5.0	100	95	65	-
Esaifan et al. 2019 [105]	kaolin	SOD/ cancrinite	5.5	99	90	54	62
Necke et al. 2022 [23]	LAS glass-ceramic	SOD/LTN	5.8	99	100	100	86
Necke et al. 2023 [24]	petalite	SOD	5.8	99	100	92	100

When discussing the adsorption results, the different synthesis routes of the zeolites also require consideration. In contrast to the hydrothermal synthesis of He et al. [143] and Esaifan et al. [105], the mechanochemical approach in this work generally led to a lower particle size associated with a higher specific surface area, which is generally advantageous for achieving a high sorption performance. Further comparison of the different approaches reveals significant differences in the starting material used, for example fly ash [143], low-grade kaolin [105], LAS glass-ceramics [23] or petalite [24], leading to the formation of different zeolite phases during synthesis, such as an unspecified zeolite [143], SOD/cancrinite [105], SOD/LTN [23] or pure SOD [24]. Due to the chemical and structural variations, it can be assumed that each of these zeolite phases has slightly different sized pores and channels within their structure, which provides an additional explanation for the different sorption rates during the heavy metal uptake. In this context, it should be mentioned that this type of adsorption mode does not occur at the particle surface, contrary it is the result of a cation exchange (e.g., Pb^{2+} for 2 Na^{+}) within the zeolite structure.

Although promising removal effects were attained during the sorption experiments, it should be noted that these experiments were performed under idealized bench-scale conditions, including comparable small-scale experiments and single metal solutions as a synthetic wastewater equivalent at defined pH value. Therefore, the absolute removal efficiencies should be considered with a certain degree of caution, as real wastewater samples are usually chemically more complex by containing a number of heavy metal cations in addition to common elements such as Ca or Mg. Since all of these cations interact and compete with each other during sorption experiments, further experiments are required to evaluate the sorption behavior of zeolite samples,

which accrue as a by-product during mechanochemical lithium extraction. It is also to be expected that typical wastewaters such as acid mine drainage have a lower pH value than the aqueous solution investigated, which impedes the transferability of the results, particularly in the case of nickel.

5 Conclusions and Outlook

For this study, end-of-life LAS glass-ceramics and naturally occurring lithium silicate minerals such as lepidolite, spodumene and petalite were selected as source materials for alkaline mechanochemical studies, focusing on lithium extraction without thermal pretreatments. This approach is part of a holistic concept (exemplarily shown for LAS glass-ceramics in Figure 5-1), trying to utilize the whole chemical inventory of the source materials leading to value-added byproducts such as Na-sodium zeolites, Ca-silicates or Ca-phosphates on the pathway to a pure lithium compound like Li_3PO_4 or $LiOH \cdot H_2O$ for re-use in LIB or other industrial applications.

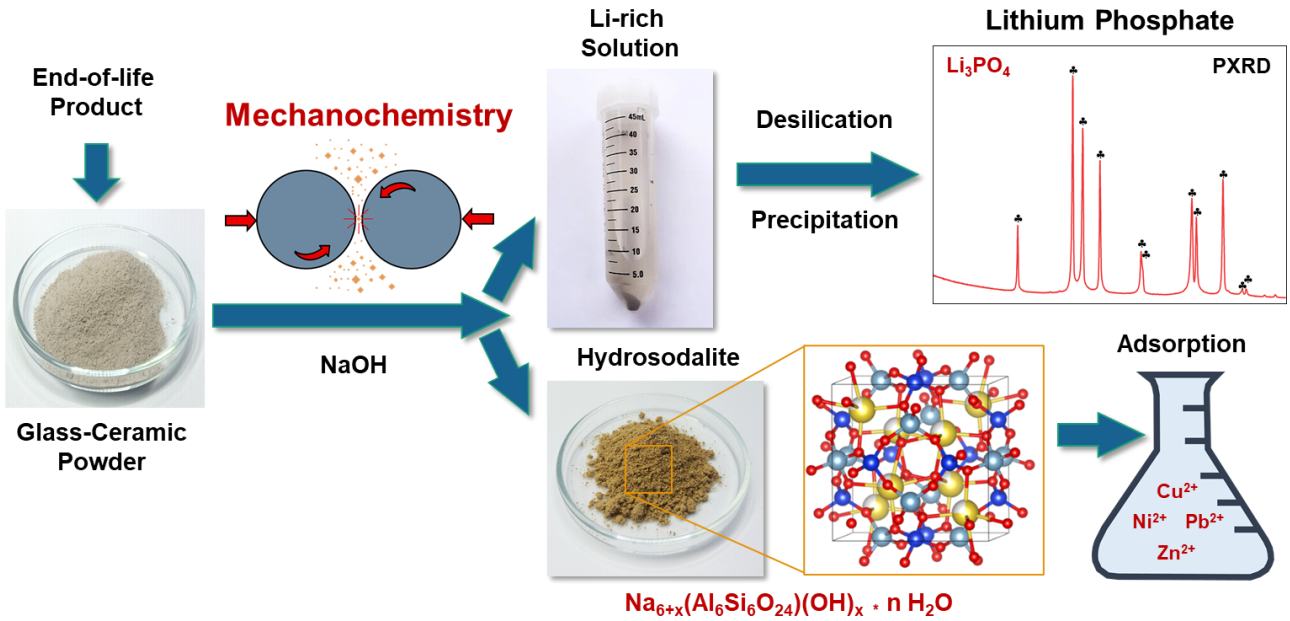

Figure 5-1. *Graphical summary of the holistic approach adopted to LAS glass-ceramics, which involved a mechanochemical treatment as a key component, converting the feed material into a hydrosodalite zeolite, while lithium was significantly leached into the solutions. In addition, downstream processing of the NaOH solution included desilication prior to precipitation of Li_3PO_4, while the zeolite by-product was potentially considered as an adsorbent for heavy metal ions from aqueous solutions.*

During the mechanochemical investigations, various experimental parameters namely NaOH concentration, rotational speed, milling time, and ball-to-powder ratio were varied, to examine their influence on lithium extraction and zeolite formation. The mechanochemical treatment of LAS samples revealed a decomposition of the lithium-containing β-quartz phase under alkaline conditions, while lithium significantly accumulates in the leaching liquor at optimal experimental parameters, such as the rotational speed and the ball-to-powder ratio of 600 rpm and 50:1 g/g. In particular, considering the high extraction yield (83.8 %) and a relatively short reaction time (60 min), the corresponding experiment at 7 mol/L NaOH proved to be most effective, as extended processing at a total time of 120 min resulted only in a slightly higher yield of 92.4 %. From the perspective of zeolite formation, however, a reaction time of 120 min is more favorable, since here the entire feed was converted into different zeolite frameworks depending on the NaOH concentration, resulting in the formation

of GIS- and LTA-type species at 3 to 5 mol/L or SOD- and LTN-type species at 7 or 9 mol/L. In summary, LAS glass-ceramics can be considered a promising starting material for lithium recovery and zeolite synthesis in combination with alkaline mechanochemical treatments, which enables the successful conversion of the reactants using comparable moderate NaOH concentrations at reasonable reaction times. In addition to the innovative experimental approach, it was shown in this work, that LAS glass-ceramic are characterized by several advantageous properties, including low lithium coordination, a relatively open framework structure and small crystallite sizes of < 100 nm in the starting material, which ensure increased reactivity.

In the second part of the work the insights gained from the investigations on LAS glass-ceramics were transferred to the three most common lithium silicate minerals lepidolite, spodumene and petalite, as shown in Figure 5-2. As indicated by the experimental results, petalite is much more compatible to the alkaline mechanochemical route compared to spodumene or lepidolite, leading to a considerable lithium extraction of 84.9 % alongside an almost complete conversion to sodalite after 120 min of ball milling in 7 mol/L NaOH solution.

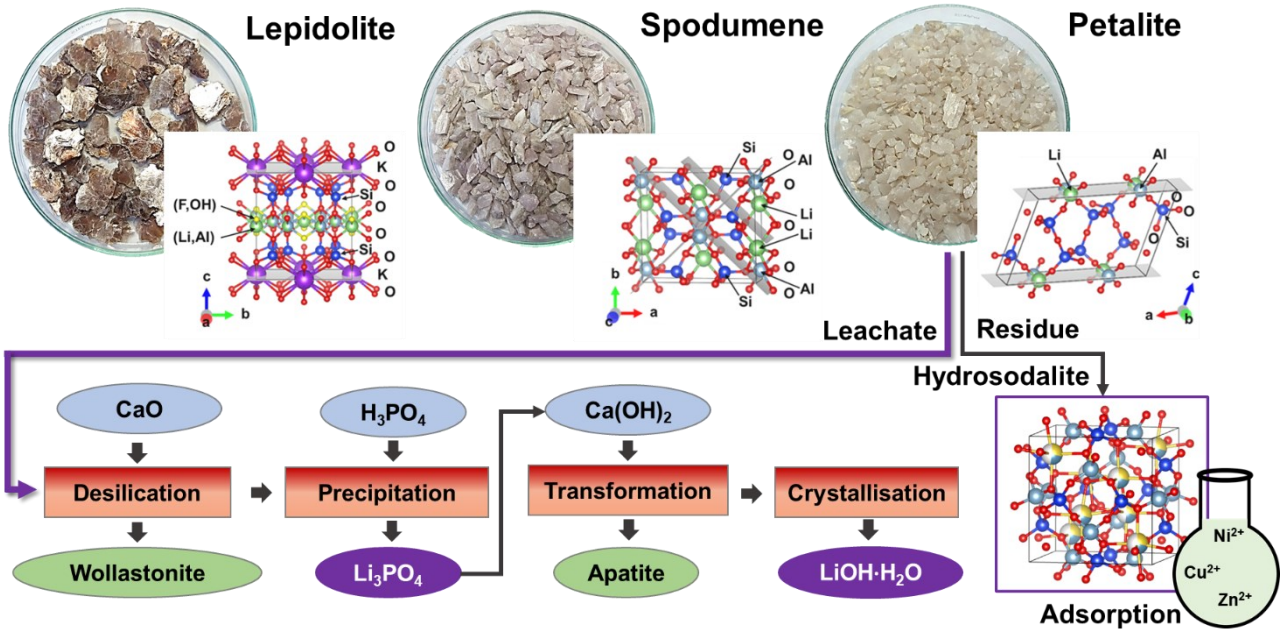

Figure 5-2. *Graphical summary of the mechanochemical treatments of the lithium silicate minerals lepidolite, spodumene and petalite. These investigations revealed petalite to be much more suitable for this approach, as the lower coordination of lithium and the activation of cleavage planes along specific crystallographic lithium sites during ball milling significantly enhance the leaching. The downstream processing of the enriched solution involved several operations to obtain $LiOH{\cdot}H_2O$ as a final product. During these intermediate steps, particular attention was paid to obtain value-added byproducts such as wollastonite or apatite, contributing to the holistic approach.*

Moreover, an explanation for the higher reactivity under mechanochemical conditions could be related to specific features of the crystal structure of petalite. In particular, the less dense atomic packing, which leads to a tetrahedral instead of octahedral coordination of lithium, and the pronounced activation of the 001 cleavage planes along the lithium sites during ball milling are particularly relevant for the enhanced leaching.
During the mechanochemical experiments, some of the silicon passed into solution as an unavoidable side effect of alkaline leaching, requiring desilication as an intermediate step prior to lithium precipitation. CaO proved to be an effective agent, resulting in 96.3 % silica removal in LAS samples at a $CaO:SiO_2$ ratio of 1.4, whereas in the petalite based liquors a lower $CaO:SiO_2$ ratio of 0.8 already resulted in 94.6 % silica removal, while the lithium

content of the solution was not significantly affected in either case. Additional, PXRD measurements of the responding precipitates revealed Ca-silicate phases such as torbermorite after drying or wollastonite after calcination, which can be classified both as value-added byproducts. After purification of the solution by desilication, lithium was precipitated by adding H_3PO_4 to the solution, which permitted the formation of Li_3PO_4 with a high purity of > 98 % at a P:Li ratio of 1.4:3.0 (LAS) or 1.2:3.0 (Ptl) with a precipitation yield of about 73 %. As a final step, Li_3PO_4 was further treated with $Ca(OH)_2$, resulting in the precipitation of Ca-phosphate and $LiOH{\cdot}H_2O$, which can be crystallized to a pure phase.

Byproducts, obtained as leaching residues during mechanochemical experiments of LAS or petalite samples consist mainly of sodalite and/or LTN zeolites, which in addition exhibit relatively high specific surface areas up to 29.8 m^2/g, determined via BET measurements. Therefore, these zeolites were investigated in a side study as potential adsorbents for heavy metal ions in wastewater samples, revealing excellent sorption efficiencies for the heavy metal ions Cu^{2+} (100 %), Pb^{2+} (> 99 %), Ni^{2+} (> 92 %) and Zn^{2+} (> 86%) at a zeolite dosage of 6 g/L at pH 6. Although the applicability of zeolite byproducts in adsorption experiments has already been successfully demonstrated in this study, further investigations are required to evaluate the entire potential of these materials. In particular, since the present studies were conducted at idealized bench-scale conditions with single element solutions containing Pb^{2+}, Cu^{2+}, Ni^{2+}, Zn^{2+} cations, further experiments should include more realistic wastewater samples including more complex chemical composition. In addition to heavy metals in aqueous solution, further adsorption studies may also involve organic pollutants, as the synthesized zeolite species are generally able to absorb these as well.

In the present work, the general applicability of the mechanochemical route for the production of lithium salts on the basis of LAS glass-ceramics or petalite was demonstrated on a laboratory scale. Further steps should therefore include the optimization of the experimental parameters via Design of Experiment (DoE) and the upscaling of the extraction step, requiring the use of an attritor mill instead of a planetary mill in order to process sample quantities in the kg range. Besides processing larger quantities, an upscaling process would enable economic and ecological considerations and a validation of the route in comparison to established processes. Challenging aspects of the current route are the comparatively low extraction yields for lepidolite (18.2 %) and spodumene (28.4 %), caused by their comparable dense crystal structures including 6-fold coordination of lithium. To overcome this drawback, more intensive treatments are required, which potentially involves thermal pretreatments, higher NaOH concentrations, a longer reaction time or a higher ball-to-powder ratio. Moreover, the high abrasivity of spodumene during ball milling has to be considered critically, leading to severe wear of the grinding equipment. In addition, the reuse of the alkaline liquid after precipitation for further extraction experiments must be further investigated and optimized, since the current yield during precipitation of about 73 % implies a loss of 27 % of the lithium, since the precipitation out of NaOH solutions are known to be challenging. Alternatively, multiple use of the leach needs to be explored to enrich the lithium to around 10 g/L, which would allow the direct precipitation of Li_2CO_3 instead of Li_3PO_4, which can generally be precipitated more effectively and gives a more versatile compound for further applications.

6 References

1. Berzelius, J. Ein neues mineralisches Alkali und ein neues Metall. In *Journal für Chemie und Physik*; Schweigger, J., Ed., 1817; pp 44–48.
2. Deberitz, J.; Boche, G. Lithium und seine Verbindungen - Industrielle, medizinische und wissenschaftliche Bedeutung. *Chemie in unserer Zeit* **2003**, *37*, 258–266, doi:10.1002/ciuz.200300264.
3. Swain, B. Recovery and recycling of lithium: A review. *Separation and Purification Technology* **2017**, *172*, 388–403, doi:10.1016/j.seppur.2016.08.031.
4. U.S. Geological Survey. *Mineral commodity summaries*, 2023, ISBN 978-1-4113-4504-1.
5. Kesler, S.E.; Gruber, P.W.; Medina, P.A.; Keoleian, G.A.; Everson, M.P.; Wallington, T.J. Global lithium resources: Relative importance of pegmatite, brine and other deposits. *Ore Geology Reviews* **2012**, *48*, 55–69, doi:10.1016/j.oregeorev.2012.05.006.
6. Fröhlich, P.; Lorenz, T.; Martin, G.; Brett, B.; Bertau, M. Wertmetalle - Gewinnungsverfahren, aktuelle Trends und Recyclingstrategien. *Angew. Chem.* **2017**, *129*, 2586–2624, doi:10.1002/ange.201605417.
7. Weidenkaff, A. Little precious lithium? *MRS Bull.* **2019**, *44*, 917, doi:10.1557/mrs.2019.296.
8. Marscheider-Weidemann, F.; Langkau, S.; Baur, S.-J.; Billaud, M.; Deubzer, O.; Eberling, E.; Erdmann, L.; Haendel, M.; Krail, M.; Loibl, A.; et al. *Rohstoffe für Zukunftstechnologien 2021;* Bundesanstalt für Geowissenschaften und Rohstoffe (BGR), Deutsche Rohstoffagentur (DERA): Berlin, 2021.
9. Pannhorst, W. Overview. In *Low Thermal Expansion Glass Ceramics*; Bach, H., Krause, D., Eds.; Springer: Berlin, 2005; pp 1–12, ISBN 978-3-540-28245-7.
10. Pannhorst, W. The Scientific Basis: Glass Ceramics Based on Lithium-Alumino-Silicate Solid Solution Crystals. In *Low Thermal Expansion Glass Ceramics*; Bach, H., Krause, D., Eds.; Springer: Berlin, 2005; pp 39–50, ISBN 978-3-540-28245-7.
11. Kern, M.; Siepenkothen, H.J. *Feldversuch Ceranfeld-Recycling: Marktrecherche und Feldversuch zum Recycling von Kochmulden mit Glaskeramik (unpublished study);* Witzenhausen Institut and Schott AG, 2014.
12. Li, H.; Eksteen, J.; Kuang, G. Recovery of lithium from mineral resources: State-of-the-art and perspectives – A review. *Hydrometallurgy* **2019**, *189*, 105129, doi:10.1016/j.hydromet.2019.105129.
13. Salakjani, N.K.; Singh, P.; Nikoloski, A.N. Mineralogical transformations of spodumene concentrate from Greenbushes, Western Australia. Part 1: Conventional heating. *Minerals Engineering* **2016**, *98*, 71–79, doi:10.1016/j.mineng.2016.07.018.
14. Vieceli, N.; Nogueira, C.A.; Pereira, M.F.; Dias, A.P.S.; Durão, F.O.; Guimarães, C.; Margarido, F. Effects of mechanical activation on lithium extraction from a lepidolite ore concentrate. *Minerals Engineering* **2017**, *102*, 1–14, doi:10.1016/j.mineng.2016.12.001.
15. Salakjani, N.K.; Singh, P.; Nikoloski, A.N. Production of Lithium – A Literature Review Part 1: Pretreatment of Spodumene. *Mineral Processing and Extractive Metallurgy Review* **2020**, *41*, 335–348, doi:10.1080/08827508.2019.1643343.
16. Peltosaari, O.; Tanskanen, P.; Heikkinen, E.-P.; Fabritius, T. α→γ→β-phase transformation of spodumene with hybrid microwave and conventional furnaces. *Minerals Engineering* **2015**, *82*, 54–60, doi:10.1016/j.mineng.2015.04.012.
17. Vieceli, N.; Nogueira, C.A.; Pereira, M.F.C.; Durão, F.O.; Guimarães, C.; Margarido, F. Optimization of an innovative approach involving mechanical activation and acid digestion for the extraction of lithium from lepidolite. *Int J Miner Metall Mater* **2018**, *25*, 11–19, doi:10.1007/s12613-018-1541-7.
18. Kotsupalo, N.P.; Menzheres, L.T.; Ryabtsev, A.D.; Boldyrev, V.V. Mechanical activation of α-spodumene for further processing into lithium compounds. *Theor Found Chem Eng* **2010**, *44*, 503–507, doi:10.1134/S0040579510040251.

19. Gasalla, H.J.; Aglietti, E.F.; Lopez, J.; Pereira, E. Changes in physicochemical properties of α-spodumene by mechanochemical treatment. *Materials Chemistry and Physics* **1987**, *17*, 379–389, doi:10.1016/0254-0584(87)90088-5.
20. Han, G.; Gu, D.; Lin, G.; Cui, Q.; Wang, H. Recovery of lithium from a synthetic solution using spodumene leach residue. *Hydrometallurgy* **2018**, *177*, 109–115, doi:10.1016/j.hydromet.2018.01.004.
21. Lv, Y.; Xing, P.; Ma, B.; Liu, Y.; Wang, C.; Zhang, W.; Chen, Y. Efficient Extraction of Lithium and Rubidium from Polylithionite via Alkaline Leaching Combined with Solvent Extraction and Precipitation. *ACS Sustainable Chem. Eng.* **2020**, *8*, 14462–14470, doi:10.1021/acssuschemeng.0c04437.
22. Xing, P.; Wang, C.; Zeng, L.; Ma, B.; Wang, L.; Chen, Y.; Yang, C. Lithium Extraction and Hydroxysodalite Zeolite Synthesis by Hydrothermal Conversion of α-Spodumene. *ACS Sustainable Chem. Eng.* **2019**, *7*, 9498–9505, doi:10.1021/acssuschemeng.9b00923.
23. Necke, T.; Wolf, D.M.; Bachmann, A.-L.; Berberich, K.; Kleebe, H.-J.; Weidenkaff, A. Mechanochemical Lithium Extraction and Zeolite Synthesis from End-of-Life Glass–Ceramics. *ACS Sustainable Chem. Eng.* **2022**, *10*, 10849–10857, doi:10.1021/acssuschemeng.2c02342.
24. Necke, T.; Stein, J.; Kleebe, H.-J.; Balke-Grünewald, B. Lithium Extraction and Zeolite Synthesis via Mechanochemical Treatment of the Silicate Minerals Lepidolite, Spodumene, and Petalite. *Minerals* **2023**, *13*, 1030, doi:10.3390/min13081030.
25. Baláž, P. *Mechanochemistry in nanoscience and minerals engineering;* Springer: Berlin, Heidelberg, 2008, ISBN 978-3-540-74854-0.
26. Heinicke, G. *Tribochemistry;* Akademie-Verlag: Berlin, 1984.
27. *The IUPAC Compendium of Chemical Terminology;* Gold, V., Ed.; International Union of Pure and Applied Chemistry (IUPAC): Research Triangle Park, NC, 2019.
28. Butyagin, P.Y. Structural Disorder and Mechanochemical Reactions in Solids. *Russ. Chem. Rev.* **1984**, *53*, 1025–1038, doi:10.1070/RC1984v053n11ABEH003138.
29. Baláž, P.; Achimovičová, M.; Baláž, M.; Billik, P.; Cherkezova-Zheleva, Z.; Criado, J.M.; Delogu, F.; Dutková, E.; Gaffet, E.; Gotor, F.J.; et al. Hallmarks of mechanochemistry: from nanoparticles to technology. *Chem. Soc. Rev.* **2013**, *42*, 7571–7637, doi:10.1039/c3cs35468g.
30. Kajdas, C. General Approach to Mechanochemistry and Its Relation to Tribochemistry. In *Tribology in Engineering*; Pihtili, H., Ed.; IntechOpen: Rijeka, Croatia, 2013, ISBN 978-953-51-1126-9.
31. Borchardt, L.; Grätz, S. Reaktoren für spezielle technischchemische Prozesse: Tribochemische Reaktoren. In *Handbuch Chemische Reaktoren*: *Grundlagen und Anwendungen der Chemischen Reaktionstechnik*; Reschetilowski, W., Ed.; Springer Spektrum: Wiesbaden, 2019; pp 1–28, ISBN 978-3-662-56444-8.
32. Takacs, L. Quicksilver from cinnabar: The first documented mechanochemical reaction? *JOM* **2000**, *52*, 12–13, doi:10.1007/s11837-000-0106-0.
33. Maini, L.; Marchini, M.; Gandolfi, M.; Raggetti, L.; Martelli, M. Quicksilver and Quick-thinking: Insight into the Alchemy of Mercury: A new interdisciplinary research to discover the chemical reality of ancient alchemical recipes (Preprint). *ChemRxiv* **2021**, doi:10.26434/chemrxiv-2021-4qn68-v2.
34. Takacs, L. M. Carey Lea, The Father of Mechanochemistry. *Bull. Hist. Chem.,* **2003**, *28*, 26–34.
35. Anastas, P.T.; Warner, J.C. *Green chemistry*: *Theory and practice;* Oxford University Press: Oxford, 2000, ISBN 0198506988.
36. Ardila-Fierro, K.J.; Hernández, J.G. Sustainability Assessment of Mechanochemistry by Using the Twelve Principles of Green Chemistry. *ChemSusChem* **2021**, *14*, 2145–2162, doi:10.1002/cssc.202100478.
37. Bowden, F.P., Yoffe, Y.D., Yoffe, A.D. *Initiation and Growth of Explosion in Liquids and Solids;* Cambridge University Press: Cambridge, 1952.
38. Bowden, F.P., Tabor, D. *The Friction and Lubrication of Solids;* Clarendon Press: Oxford, 1958.
39. Weichert, R.; Schönert, K. On the temperature rise at the tip of a fast running crack. *Journal of the Mechanics and Physics of Solids* **1974**, *22*, 127–133, doi:10.1016/0022-5096(74)90018-0.
40. Thiessen, P.A., Meyer, K., Heinicke, G. *Grundlagen der Tribochemie;* Akademie-Verlag: Berlin, 1967.
41. Ma, X.; Yuan, W.; Bell, S.E.J.; James, S.L. Better understanding of mechanochemical reactions: Raman monitoring reveals surprisingly simple 'pseudo-fluid' model for a ball milling reaction. *Chem. Commun. (Camb)* **2014**, *50*, 1585–1587, doi:10.1039/c3cc47898j.

42. Fischer, F. *Mechanochemie: Charakterisierung und Synthese von Cokristallen (Dissertation);* Humboldt-Universität zu Berlin, Mathematisch-Naturwissenschaftliche Fakultät, 2016.
43. Necke, T.; Bachmann, A.-L.; Bokelmann, K.; Homm, G.; Weidenkaff, A.; Kleebe, H.-J. Mechanochemistry. Sustainable extraction and recovery of metals: The case of lithium silicate minerals. *Poster Presentation at International Conference on Resource Chemistry (ICRC)* **2021**.
44. James, S.L.; Adams, C.J.; Bolm, C.; Braga, D.; Collier, P.; Friščić, T.; Grepioni, F.; Harris, K.D.M.; Hyett, G.; Jones, W.; et al. Mechanochemistry: opportunities for new and cleaner synthesis. *Chem. Soc. Rev.* **2012**, *41*, 413–447, doi:10.1039/c1cs15171a.
45. Jones, W.; Eddleston, M.D. Introductory lecture: Mechanochemistry, a versatile synthesis strategy for new materials. *Faraday Discuss.* **2014**, *170*, 9–34, doi:10.1039/C4FD00162A.
46. Guo, X.; Xiang, D.; Duan, G.; Mou, P. A review of mechanochemistry applications in waste management. *Waste Manag.* **2010**, *30*, 4–10, doi:10.1016/j.wasman.2009.08.017.
47. Tan, Q.; Li, J. Recycling metals from wastes: a novel application of mechanochemistry. *Environ. Sci. Technol.* **2015**, *49*, 5849–5861, doi:10.1021/es506016w.
48. Kipp, S.; Šepelák, V.; Becker, K.D. Mechanochemie: Chemie mit dem Hammer. *Chemie in unserer Zeit* **2005**, *39*, 384–392, doi:10.1002/ciuz.200500355.
49. Ou, Z.; Li, J.; Wang, Z. Application of mechanochemistry to metal recovery from second-hand resources: a technical overview. *Environ. Sci. Process. Impacts* **2015**, *17*, 1522–1530, doi:10.1039/c5em00211g.
50. Sandström, Å. Mechanochemical Treatment in Metallurgy : An overview. *Conference in Minerals Engineering: 02/02/2016 - 03/02/2016* **2016**.
51. Zelikman, A.N., Voldman, G.M., Beljajevskaja, L.V. *Theory of Hydrometallurgical Processes (in Russian).;* Metallurgija: Moscow, 1975.
52. Baláž, P.; Aláčová, A.; Achimovičová, M.; Ficeriová, J.; Godočíková, E. Mechanochemistry in hydrometallurgy of sulphide minerals. *Hydrometallurgy* **2005**, *77*, 9–17, doi:10.1016/j.hydromet.2004.09.009.
53. Mulenshi, J.; Chelgani, S.C.; Rosenkranz, J. Mechanochemical Treatment of Historical Tungsten Tailings: Leaching While Grinding for Tungsten Extraction Using NaOH. *Sustainability* **2021**, *13*, 3258, doi:10.3390/su13063258.
54. Khajavi, S.; Jansen, J.C.; Kapteijn, F. Production of ultra pure water by desalination of seawater using a hydroxy sodalite membrane. *Journal of Membrane Science* **2010**, *356*, 52–57, doi:10.1016/j.memsci.2010.03.026.
55. Kazemimoghadam, M. Preparation of Nanopore Hydroxysodalite Zeolite Membranes by Dry Gel Method. *J Applied Chem. Sci.* **2018**, *5*, 424–429, doi:10.22341/jacs.on.00501p424.
56. Golbad, S.; Khoshnoud, P.; Abu-Zahra, N. Hydrothermal synthesis of hydroxy sodalite from fly ash for the removal of lead ions from water. *Int. J. Environ. Sci. Technol.* **2017**, *14*, 135–142, doi:10.1007/s13762-016-1133-x.
57. Alizadeh Arasi, M.; Salem, A.; Salem, S. Nano-porous hydrosodalite fabrication via hydrothermal modification of processed kaolin by boehmite: Aluminum source effect on physico-chemical characteristics of product. *Advanced Powder Technology* **2020**, *31*, 2379–2384, doi:10.1016/j.apt.2020.04.001.
58. Rainer, D.N.; Morris, R.E. New avenues for mechanochemistry in zeolite science. *Dalton Trans.* **2021**, *50*, 8995–9009, doi:10.1039/d1dt01440d.
59. Majano, G.; Borchardt, L.; Mitchell, S.; Valtchev, V.; Pérez-Ramírez, J. Rediscovering zeolite mechanochemistry – A pathway beyond current synthesis and modification boundaries. *Microporous and Mesoporous Materials* **2014**, *194*, 106–114, doi:10.1016/j.micromeso.2014.04.006.
60. Morris, R.E.; James, S.L. Solventless synthesis of zeolites. *Angew. Chem. Int. Ed Engl.* **2013**, *52*, 2163–2165, doi:10.1002/anie.201209002.
61. Nada, M.H.; Larsen, S.C.; Gillan, E.G. Mechanochemically-assisted solvent-free and template-free synthesis of zeolites ZSM-5 and mordenite. *Nanoscale Adv.* **2019**, *1*, 3918–3928, doi:10.1039/C9NA00399A.
62. Prokof'ev, V.Y.; Gordina, N.E.; Zhidkova, A.B.; Efremov, A.M. Mechanochemical synthesis of granulated LTA zeolite from metakaolin. *J Mater Sci* **2012**, *47*, 5385–5392, doi:10.1007/s10853-012-6421-3.

63. Ren, L.; Wu, Q.; Yang, C.; Zhu, L.; Li, C.; Zhang, P.; Zhang, H.; Meng, X.; Xiao, F.-S. Solvent-free synthesis of zeolites from solid raw materials. *J. Am. Chem. Soc.* **2012**, *134*, 15173–15176, doi:10.1021/ja3044954.
64. Wu, Q.; Meng, X.; Gao, X.; Xiao, F.-S. Solvent-Free Synthesis of Zeolites: Mechanism and Utility. *Acc. Chem. Res.* **2018**, *51*, 1396–1403, doi:10.1021/acs.accounts.8b00057.
65. d'Andrada, J.B. Kurze Angabe der Eigenschaften und Kennzeichen einiger neuen Fossilien aus Schweden und Norwegen nebst einigen chemischen Bemerkungen über dieselben. *Allgemeines Journal der Chemie* **1800**, *4*, 28–39.
66. Weeks, M.E.; Larson, M.E. J.A. Arfwedson and his services to chemistry. *Journal of Chemical Education* **1937**, *14*, 403–407, doi:10.1021/ed014p403.
67. Holleman, A.F.; Wiberg E.; Wiberg, N. *Grundlagen und Hauptgruppenelemente: Band 1: Grundlagen und Hauptgruppenelemente*, 103rd ed.; De Gruyter, 2016, ISBN 9783110495850.
68. Wietelmann, U.; Bauer, R.J. Lithium and Lithium Compounds, doi:10.1002/14356007.a15_393.
69. Gmelin, C.G. Analyse des Petalits und Untersuchung der chemischen Verhältnisse des Lithons. *Ann. Phys.* **1819**, *62*, 399–421.
70. Neufeldt, S. *Chronologie Chemie*: *Entdecker und Entdeckungen*, 3. Auflage; Wiley-VCH: Weinheim, 2016, ISBN 3527662839.
71. Tidwell, T.T. Wilhelm Schlenks Leben und Werk - Aufstieg und Fall eines brillanten Wissenschaftlers. *Angew. Chem.* **2001**, *113*, 343–349, doi:10.1002/1521-3757(20010119)113:2<343:AID-ANGE343>3.0.CO;2-R.
72. Kamienski, C.W.; McDonald, D.P.; Stark, M.W.; Papcun, J.R. Lithium and Lithium Compounds. In *Kirk-Othmer Encyclopedia of Chemical Technology*; John Wiley & Sons, I., Ed.; Wiley, 2000, ISBN 9780471484943.
73. Okrusch, M.; Matthes, S. *Mineralogie*: *Eine Einführung in die spezielle Mineralogie, Petrologie und Lagerstättenkunde*, 9.th ed.; Springer Gabler: Wiesbaden, 2014, ISBN 9783642346590.
74. mindat.org. The mineralogy of Lithium. Available online: https://www.mindat.org/element/Lithium (accessed on 9 January 2023).
75. Schmidt, M. *Rohstoffrisikobewertung Lithium;* Bundesanstalt für Geowissenschaften und Rohstoffe (BGR), Deutsche Rohstoffagentur (DERA): Berlin, 2017.
76. Garrett, D.E. *Handbook of lithium and natural calcium chloride;* Elsevier, 2004, ISBN 0080472907.
77. Schaller, W.T. Mineralogic Notes - Series 3 **1916**, *USGS Bulletin*, 138–139.
78. Partington G.A. Greenbushes tin, tantalum and lithium deposit. In *Australian Ore deposits*; Phillips, G.N., Ed.; Australian Institute of Mining and Metallurgy Monography: Melbourne, 2017; pp 339–342.
79. Brown, T. Mineral Commodity Profile - Lithium. Available online: https://www.bgs.ac.uk/news/mineral-profile-lithium/ (accessed on 11 April 2024).
80. Ighalo, J.O.; Amaku, J.F.; Olisah, C.; Adeola, A.O.; Iwuozor, K.O.; Akpomie, K.G.; Conradie, J.; Adegoke, K.A.; Oyedotun, K.O. Utilisation of adsorption as a resource recovery technique for lithium in geothermal water. *Journal of Molecular Liquids* **2022**, *365*, 120107, doi:10.1016/j.molliq.2022.120107.
81. Park, J.; Sato, H.; Nishihama, S.; Yoshizuka, K. Lithium Recovery from Geothermal Water by Combined Adsorption Methods. *Solvent Extraction and Ion Exchange* **2012**, *30*, 398–404, doi:10.1080/07366299.2012.687165.
82. Meshram, P.; Pandey, B.D.; Mankhand, T.R. Extraction of lithium from primary and secondary sources by pre-treatment, leaching and separation: A comprehensive review. *Hydrometallurgy* **2014**, *150*, 192–208, doi:10.1016/j.hydromet.2014.10.012.
83. Stewart, D.B. Petrogenesis of lithium-rich pegmatites. *American Mineralogist* **1978**, *63*, 970–980.
84. Simmons, W.B. Gem-bearing pegmatites. In *The geology of gem deposits*; Groat, L.A., Ed.; Mineralogical Association of Canada: Québec, 2007; pp 169–206, ISBN 978-0-921294-37-5.
85. London, D. Experimental phase equilibria in the system $LiAlSiO_4$–SiO_2–H_2O: a petrogenetic grid for lithium-rich pegmatites. *American Mineralogist* **1984**, *69*, 995–1004.
86. French, B.M.; Jezek, P.A.; Appleman, D.E. Virgilite; a new lithium aluminum silicate mineral from the Macusani glass, Peru. *American Mineralogist* **1978**, *63*, 461–465.
87. Fritzsch, E. Minerals of the ETTA Pegmatite: Black Hills, South Dakota. *Rocks & Minerals* **1992**, *67*, 380–388, doi:10.1080/00357529.1992.9926507.

88. mindat.org. Lepidolite - Entry in the database. Available online: https://www.mindat.org/min-2380.html (accessed on 19 February 2024).
89. mindat.org. Spodumene - Entry in the database. Available online: https://www.mindat.org/min-3733.html (accessed on 19 February 2024).
90. mindat.org. Petalite - Entry in the database. Available online: https://www.mindat.org/min-3171.html (accessed on 19 February 2024).
91. Haussühl, E.; Schreuer, J.; Winkler, B.; Haussühl, S.; Bayarjargal, L.; Milman, V. Structure-property relations and thermodynamic properties of monoclinic petalite, $LiAlSi_4O_{10}$. *J. Phys.: Condens. Matter* **2012**, *24*, 345402, doi:10.1088/0953-8984/24/34/345402.
92. Zemann-Hedlik, A.; Zemann, J. Die Kristallstruktur von Petalit, $LiAlSi_4O_{10}$. *Acta Cryst* **1955**, *8*, 781–787, doi:10.1107/S0365110X55002405.
93. Černý, P.; London, D. Crystal chemistry and stability of petalite. *TMPM Tschermaks Petr. Mitt.* **1983**, *31*, 81–96, doi:10.1007/BF01084763.
94. Tadesse, B.; Makuei, F.; Albijanic, B.; Dyer, L. The beneficiation of lithium minerals from hard rock ores: A review. *Minerals Engineering* **2019**, *131*, 170–184, doi:10.1016/j.mineng.2018.11.023.
95. Sitando, O.; Crouse, P.L. Processing of a Zimbabwean petalite to obtain lithium carbonate. *International Journal of Mineral Processing* **2012**, *102-103*, 45–50, doi:10.1016/j.minpro.2011.09.014.
96. Vieceli, N.C.; Gonçalves Nogueira, C.A.; Ramos da Cruz Magarido, F.M.; Costa Pereira, M.F.; de Oliveira Durão, F.; Alonso da Costa Guimarães, C.A. Patent - WO2017200408A1: Process of lithium extraction from ores and concentrates by mechanical activation and reaction with sulphuric acid **2017**.
97. Qiu, S.; Zhu, Y.; Jiang, Y.; Liu, C.; Yu, J. Kinetics and Mechanism of Lithium Extraction from α-Spodumene in Potassium Hydroxide Solution. *Ind. Eng. Chem. Res.* **2022**, *61*, 15103–15113, doi:10.1021/acs.iecr.2c02019.
98. Xiao, M.; Wang, S.; Zhang, Q.; Zhang, J. Leaching mechanism of the spodumene sulphuric acid process. *Rare Metals* **1997**, 37–45.
99. Kuang, G.; Chen, Z.B.; Guo, H.; Li, M.H. Lithium Extraction Mechanism from α-Spodumene by Fluorine Chemical Method. *AMR* **2012**, *524-527*, 2011–2016, doi:10.4028/www.scientific.net/AMR.524-527.2011.
100. Rosales, G.D.; Del Ruiz, M.C.; Rodriguez, M.H. Novel process for the extraction of lithium from β-spodumene by leaching with HF. *Hydrometallurgy* **2014**, *147-148*, 1–6, doi:10.1016/j.hydromet.2014.04.009.
101. Guo, H.; Kuang, G.; Wang, H.; Yu, H.; Zhao, X. Investigation of Enhanced Leaching of Lithium from α-Spodumene Using Hydrofluoric and Sulfuric Acid. *Minerals* **2017**, *7*, 205, doi:10.3390/min7110205.
102. Griffith, C.S.; Griffin, A.C.; Roper, A.; Skalski, A. Development of SiLeach® Technology for the Extraction of Lithium Silicate Minerals. In *Extraction 2018. The Minerals, Metals & Materials Series.*: *Proceedings of the First Global Conference on Extractive Metallurgy*; Davis, B.R., et al., Eds.; Springer, 2018; pp 2235–2245.
103. Song, Y.; Zhao, T.; He, L.; Zhao, Z.; Liu, X. A promising approach for directly extracting lithium from α-spodumene by alkaline digestion and precipitation as phosphate. *Hydrometallurgy* **2019**, *189*, 105141, doi:10.1016/j.hydromet.2019.105141.
104. Ivanenko, O.; Pavlenko, T. Hydrothermal Extraction of Lithium Compounds from Petalite $Li[AlSi_4O_{10}]$. *Ukr. Chem. Journ.* **2021**, *87*, 45–54, doi:10.33609/2708-129X.87.11.2021.45-54.
105. Esaifan, M.; Warr, L.N.; Grathoff, G.; Meyer, T.; Schafmeister, M.-T.; Kruth, A.; Testrich, H. Synthesis of Hydroxy-Sodalite/Cancrinite Zeolites from Calcite-Bearing Kaolin for the Removal of Heavy Metal Ions in Aqueous Media. *Minerals* **2019**, *9*, 484, doi:10.3390/min9080484.
106. Nabavi, M.S.; Mohammadi, T.; Kazemimoghadam, M. Hydrothermal synthesis of hydroxy sodalite zeolite membrane: Separation of H_2/CH_4. *Ceramics International* **2014**, *40*, 5889–5896, doi:10.1016/j.ceramint.2013.11.033.
107. Yan, Q.; Li, X.; Wang, Z.; Wu, X.; Guo, H.; Hu, Q.; Peng, W.; Wang, J. Extraction of valuable metals from lepidolite. *Hydrometallurgy* **2012**, *117-118*, 116–118, doi:10.1016/j.hydromet.2012.02.004.
108. Kuang, G.; Liu, Y.; Li, H.; Xing, S.; Li, F.; Guo, H. Extraction of lithium from β-spodumene using sodium sulfate solution. *Hydrometallurgy* **2018**, *177*, 49–56, doi:10.1016/j.hydromet.2018.02.015.
109. Archambault, M.; Olivier, C.A. Carbonatization Roast of Lithium-bearing Ores. *US Patent 3380802A* **1968**.

110. Chen, Y.; Tian, Q.; Chen, B.; Shi, X.; Liao, T. Preparation of lithium carbonate from spodumene by a sodium carbonate autoclave process. *Hydrometallurgy* **2011**, *109*, 43–46, doi:10.1016/j.hydromet.2011.05.006.
111. Tiihonen, M.; Haavanlammi, L.; Kinnunen, S.; Kolehmainen, E. Outotec lithium hydroxide process - a novel direct leach process for the production of battery grade lithium hydroxide monohydrate form calcined spodumene. *Lithium Processing Conference*: *ALTA 2019, 18-25 May Perth, Australia: 24th annual conference proceedings*; ALTA Metallurgical Services: Melbourne, 2019, ISBN 9780994642592.
112. Barbosa, L.I.; Valente, N.G.; González, J.A. Kinetic study on the chlorination of β-spodumene for lithium extraction with Cl_2 gas. *Thermochimica Acta* **2013**, *557*, 61–67, doi:10.1016/j.tca.2013.01.033.
113. Barbosa, L.I.; González, J.A.; Del Ruiz, M.C. Extraction of lithium from β-spodumene using chlorination roasting with calcium chloride. *Thermochimica Acta* **2015**, *605*, 63–67, doi:10.1016/j.tca.2015.02.009.
114. Barbosa, L.I.; Valente, G.; Orosco, R.P.; González, J.A. Lithium extraction from β-spodumene through chlorination with chlorine gas. *Minerals Engineering* **2014**, *56*, 29–34, doi:10.1016/j.mineng.2013.10.026.
115. Yan, Q.; Li, X.; Wang, Z.; Wang, J.; Guo, H.; Hu, Q.; Peng, W.; Wu, X. Extraction of lithium from lepidolite using chlorination roasting–water leaching process. *Transactions of Nonferrous Metals Society of China* **2012**, *22*, 1753–1759, doi:10.1016/S1003-6326(11)61383-6.
116. Martin, G.; Schneider, A.; Bertau, M. Lithiumgewinnung aus heimischen Rohstoffen. *Chemie in unserer Zeit* **2018**, *52*, 298–312, doi:10.1002/ciuz.201800827.
117. Mende, R.; Kaiser, D.; Pavón, S.; Bertau, M. The COOL Process: A Holistic Approach Towards Lithium Recycling. *Waste Biomass Valor* **2023**, *14*, 3027–3042, doi:10.1007/s12649-023-02043-5.
118. Schneider, A.; Schmidt, H.; Meven, M.; Brendler, E.; Kirchner, J.; Martin, G.; Bertau, M.; Voigt, W. Lithium extraction from the mineral zinnwaldite: Part I: Effect of thermal treatment on properties and structure of zinnwaldite. *Minerals Engineering* **2017**, *111*, 55–67, doi:10.1016/j.mineng.2017.05.006.
119. Martin, G.; Schneider, A.; Voigt, W.; Bertau, M. Lithium extraction from the mineral zinnwaldite: Part II: Lithium carbonate recovery by direct carbonation of sintered zinnwaldite concentrate. *Minerals Engineering* **2017**, *110*, 75–81, doi:10.1016/j.mineng.2017.04.009.
120. Kim, Y.; Han, Y.; Kim, S.; Jeon, H.-S. Green extraction of lithium from waste lithium aluminosilicate glass-ceramics using a water leaching process. *Process Safety and Environmental Protection* **2021**, *148*, 765–774, doi:10.1016/j.psep.2021.02.001.
121. Lee, D.; Joo, S.-H.; Shin, D.J.; Shin, S.M. Recovery of Li from lithium aluminum silicate (LAS) glass-ceramics after heat treatment at 1000 °C and Ca salt-assisted water leaching in two stages before and after calcination at 600 °C. *Hydrometallurgy* **2022**, *211*, 105876, doi:10.1016/j.hydromet.2022.105876.
122. Lee, D.; Joo, S.-H.; Shin, D.J.; Shin, S.M. Evaluation of leaching characteristic and kinetic study of lithium from lithium aluminum silicate glass-ceramics by NaOH. *Journal of Environmental Sciences* **2021**, *107*, 98–110, doi:10.1016/j.jes.2021.02.001.
123. Ramström, O. *Scientific Background on the Nobel Prize in Chemistry 2019 - Lithium-ion batteries;* The Royal Swedish Academy of Sciences: Stockholm, 2019.
124. Goodenough, J.B.; Park, K.-S. The Li-ion rechargeable battery: A Perspective. *J. Am. Chem. Soc.* **2013**, *135*, 1167–1176, doi:10.1021/ja3091438.
125. Vuorilehto, K. Materialien und Funktion. In *Handbuch Lithium-Ionen-Batterien*; Korthauer, R., Ed.; Springer Vieweg: Berlin, Heidelberg, 2013; pp 21–29, ISBN 978-3-642-30652-5.
126. Zhang, Z.; Zhang S. S. Challenges of Key Materials for Rechargeable Batteries. In *Rechargeable Batteries*: *Materials, Technologies and New Trends*; Zhang, Z., Zhang, S.S., Eds.; Springer International Publishing AG: Cham, 2015; pp 1–24, ISBN 9783319154589.
127. Nitta, N.; Wu, F.; Lee, J.T.; Yushin, G. Li-ion battery materials: present and future. *Materials Today* **2015**, *18*, 252–264, doi:10.1016/j.mattod.2014.10.040.
128. Lutpi, H.A.; Mohamad, H.; Abdullah, T.K.; Ismail, H. Effect of isothermal treatment on the structural, microstructure, and physio-mechanical properties of Li_2O-Al_2O_3-SiO_2 glass–ceramic. *J Aust Ceram Soc* **2022**, *58*, 9–20, doi:10.1007/s41779-021-00662-6.
129. Müller, G. The Scientific Basis: Structure, Composition, Stability, and Thermal Expansion of High-Quartz and Keatite-Type Alumino-Silicates. In *Low Thermal Expansion Glass Ceramics*; Bach, H., Krause, D., Eds.; Springer: Berlin, 2005; pp 13–25, ISBN 978-3-540-28245-7.

130. Hummel, F.A. Thermal Expansion Properties of Some Synthetic Lithia Minerals. *J American Ceramic Society* **1951**, *34*, 235–239, doi:10.1111/j.1151-2916.1951.tb11646.x.
131. Smoke, E.J. Ceramic Compositions Having Negative Linear Thermal Expansion. *J American Ceramic Society* **1951**, *34*, 87–90, doi:10.1111/j.1151-2916.1951.tb13491.x.
132. Buerger, M.J. The stuffed derivatives of the silica structures. *American Mineralogist* **1954**, *39*, 600–614.
133. Xu, H.; Heaney, P.J.; Beall, G.H. Phase transitions induced by solid solution in stuffed derivatives of quartz: A powder synchrotron XRD study of the $LiAlSiO_4$ -SiO_2 join. *American Mineralogist* **2000**, *85*, 971–979, doi:10.2138/am-2000-0711.
134. Momma, K.; Izumi, F. VESTA 3 for three-dimensional visualization of crystal, volumetric and morphology data. *J Appl Crystallogr* **2011**, *44*, 1272–1276, doi:10.1107/S0021889811038970.
135. Götz, H.; Kosmas, I.; Naß, P.; Rodek, E.W.; Schild, H.; Schmidbauer, W.; Schröder, F.; Siebers, F.; Taplan, M.; Weinberg, W. Glass Ceramics for Household Appliances: Development and Production of Glass Ceramic Cooktop Panels. In *Low Thermal Expansion Glass Ceramics*; Bach, H., Krause, D., Eds.; Springer: Berlin, 2005; pp 81–103, ISBN 978-3-540-28245-7.
136. Schiffner, U. The Scientific Basis: Nucleation in Parent Glasses for Lithia Alumino-Silicate Glass Ceramics. In *Low Thermal Expansion Glass Ceramics*; Bach, H., Krause, D., Eds.; Springer: Berlin, 2005; pp 25–39, ISBN 978-3-540-28245-7.
137. Willhauk, E.; Harikantha, R. Glass Ceramics for Household Appliances: Cooking Systems with Ceran: High-Tech Appliances for the Kitchen. In *Low Thermal Expansion Glass Ceramics*; Bach, H., Krause, D., Eds.; Springer: Berlin, 2005; pp 51–58, ISBN 978-3-540-28245-7.
138. Xing, P.; Wang, C.; Wang, L.; Ma, B.; Chen, Y.; Wang, G. Clean and efficient process for the extraction of rubidium from granitic rubidium ore. *Journal of Cleaner Production* **2018**, *196*, 64–73, doi:10.1016/j.jclepro.2018.06.041.
139. Ma, J.; Zhai, K.; Li, Z. Desilication of synthetic Bayer liquor with calcium sulfate dihydrate: Kinetics and modelling. *Hydrometallurgy* **2011**, *107*, 48–55, doi:10.1016/j.hydromet.2011.01.002.
140. Wolf, D.M. *Master Thesis: (Rück-)Gewinnung von Lithium aus Prozessflüssigkeiten;* Heinrich Heine Universität: Düsseldorf, 2022.
141. *CRC handbook of chemistry and physics*: *A ready-reference book of chemical and physical data;* Lide, D.R., Ed., 90. ed.; CRC Press: Boca Raton, FL, 2009, ISBN 9781420090840.
142. Mulwanda, J.; Senanayake, G.; Oskierski, H.; Altarawneh, M.; Dlugogorski, B.Z. Leaching of lepidolite and recovery of lithium hydroxide from purified alkaline pressure leach liquor by phosphate precipitation and lime addition. *Hydrometallurgy* **2021**, *201*, 105538, doi:10.1016/j.hydromet.2020.105538.
143. He, K.; Chen, Y.; Tang, Z.; Hu, Y. Removal of heavy metal ions from aqueous solution by zeolite synthesized from fly ash. *Environ. Sci. Pollut. Res. Int.* **2016**, *23*, 2778–2788, doi:10.1007/s11356-015-5422-6.
144. Golomeova, M.; Zendelska, A.; Blazev, K.; Krstev, B.; Golomeov, B. Removal of Heavy Metals from Aqueous Solution using Clinoptilolite and Stilbite. *International Journal of Engineering Research & Technology* **2014**, *Vol. 3*, 1029–1035.
145. Nölte, J. *ICP-Emissionsspektrometrie für Praktiker*: *Grundlagen, Methodenentwicklung, Anwendungsbeispiele*, 1. Nachdr. 2003; Wiley-VCH: Weinheim, 2003, ISBN 9783527303519.
146. Douvris, C.; Vaughan, T.; Bussan, D.; Bartzas, G.; Thomas, R. How ICP-OES changed the face of trace element analysis: Review of the global application landscape. *Sci. Total Environ.* **2023**, *905*, 167242, doi:10.1016/j.scitotenv.2023.167242.
147. König, U.; Simões Angélica, R.; Norberg, N.; Andrade Gobbo, L. de. Rapid X-ray diffraction (XRD) for grade control of bauxites. *Conference Paper, ICSOBA, Belem* **2012**, 1–11.
148. Spieß, L.; Teichert, G.; Schwarzer, R.; Behnken, H.; Genzel, C. *Moderne Röntgenbeugung*: *Röntgendiffraktometrie für Materialwissenschaftler, Physiker und Chemiker*, 3. Auflage; Springer Spektrum: Wiesbaden, 2019, ISBN 9783834882325.
149. Waseda, Y.; Matsubara, E.; Shinoda, K. *X-ray diffraction crystallography*: *Introduction, examples and solved problems;* Springer: Heidelberg, New York, 2011, ISBN 1-283-08194-6.
150. Dang, J.; Wang, N.; Atiyeh, H.K. Review of Dissolved CO and H_2 Measurement Methods for Syngas Fermentation. *Sensors* **2021**, *21*, 2165, doi:10.3390/s21062165.

151. Stuart, B.H. *Infrared spectroscopy*: *Fundamentals and applications;* Wiley: Chichester, 2008, ISBN 0470854278.
152. Günzler, H.; Gremlich, H.-U. *IR-Spektroskopie*: *Eine Einführung*, 4. Auflage; Wiley-VCH: Weinheim, 2003, ISBN 9783527308019.
153. Brunauer, S.; Emmett, P.H.; Teller, E. Adsorption of Gases in Multimolecular Layers. *J. Am. Chem. Soc.* **1938**, *60*, 309–319, doi:10.1021/ja01269a023.
154. Lowell, S.; Shields, J.E.; Thomas, M.A.; Thommes, M. *Characterization of porous solids and powders*: *Surface area, pore size and density*, First Edition; Springer Science+Business Media: New York, 2004, ISBN 9781402023033.
155. Webb, P.A.; Orr, C. *Analytical methods in fine particle technology*, 1. ed.; Micromeritics Instrument Corp: Norcross, Ga., 1997, ISBN 096567830X.
156. Goldstein, J.I. *Scanning Electron Microscopy and X-ray Microanalysis*: *Third Edition;* Springer: Boston, MA, 2003, ISBN 9781461502159.
157. Miehe, G. Program for Interpreting Electron Diffraction Patterns PIEP, version 7.12. *Department of Materials Science, Darmstadt University of Technology* **2002**.
158. Seto, Y.; Ohtsuka, M. ReciPro: free and open-source multipurpose crystallographic software integrating a crystal model database and viewer, diffraction and microscopy simulators, and diffraction data analysis tools. *J Appl Crystallogr* **2022**, *55*, 397–410, doi:10.1107/S1600576722000139.
159. Williams, D.B.; Carter, C.B. *Transmission Electron Microscopy*: *A Textbook for Materials Science*, 2nd ed.; Springer US: Boston, MA, 2009, ISBN 9780387765013.
160. Thomas, J.; Gemming, T. *Analytische Transmissionselektronenmikroskopie*: *Eine Einführung für den Praktiker;* Springer: Wien, Heidelberg, 2013, ISBN 978-3-7091-1439-1.
161. Stiess, M. *Mechanische Verfahrenstechnik - Partikeltechnologie 1*, 3rd ed.; Springer Berlin Heidelberg: Berlin, Heidelberg, 2009, ISBN 9783540325529.
162. Tagai, T.; Ried, H.; Joswig, W.; Korekawa, M. Kristallographische Untersuchungen eines Petalits mittels Neutronenbeugung und Transmissionselektronenmikroskopie. *Zeitschrift für Kristallographie* **1982**, *160*, 159–170, doi:10.1524/zkri.1982.160.3-4.159.
163. Necke, T.; Peter, J.; Rossa, J.D.; Kleebe, H.-J.; Balke, B.; Weidenkaff, A. Investigations on Lithium-containing Glass-Ceramics during Mechanochemical Recycling. *Poster Presentation at Microscopy Conference (MC), Darmstadt* **2023**.
164. Kleebusch, E.; Rüssel, C.; Patzig, C.; Höche, T. Evidence of epitaxial growth of high-quartz solid solution on $ZrTiO_4$ nuclei in a Li_2O-Al_2O_3-SiO_2 glass. *Journal of Alloys and Compounds* **2018**, *748*, 73–79, doi:10.1016/j.jallcom.2018.03.128.
165. Subotić, B.; Škrtić, D.; Šmit, I.; Sekovanić, L. Transformation of zeolite A into hydroxysodalite: I. An approach to the mechanism of transformation and its experimental evaluation. *Journal of Crystal Growth* **1980**, *50*, 498–508, doi:10.1016/0022-0248(80)90099-8.
166. Peng, H.; Vaughan, J.; Vogrin, J. Effect of Alkalinity on Zeolite LTN Formation under Bayer Process Pre-desilication Conditions. *Ind. Eng. Chem. Res.* **2021**, *60*, 10119–10128, doi:10.1021/acs.iecr.1c02134.
167. Baerlocher, C.; McCusker, L.B. Database of Zeolite Structures. Available online: http://www.iza-structure.org/databases/ (accessed on 5 February 2024).
168. Marsh, A.; Heath, A.; Patureau, P.; Evernden, M.; Walker, P. A mild conditions synthesis route to produce hydrosodalite from kaolinite, compatible with extrusion processing. *Microporous and Mesoporous Materials* **2018**, *264*, 125–132, doi:10.1016/j.micromeso.2018.01.014.
169. Daramola, M.O.; Oloye, O.; Yaya, A. Nanocomposite sodalite/ceramic membrane for pre-combustion CO_2 capture: synthesis and morphological characterization. *Int J Coal Sci Technol* **2017**, *4*, 60–66, doi:10.1007/s40789-016-0124-3.
170. Mikuła, A.; Król, M.; Koleżyński, A. The influence of the long-range order on the vibrational spectra of structures based on sodalite cage. *Spectrochim. Acta A Mol. Biomol. Spectrosc.* **2015**, *144*, 273–280, doi:10.1016/j.saa.2015.02.073.
171. Henderson, C.; Taylor, D. Infrared spectra of anhydrous members of the sodalite family. *Spectrochimica Acta Part A: Molecular Spectroscopy* **1977**, *33*, 283–290, doi:10.1016/0584-8539(77)80032-9.

172. Esaifan, M.; Hourani, M.; Khoury, H.; Rahier, H.; Wastiels, J. Synthesis of hydroxysodalite zeolite by alkali-activation of basalt powder rich in calc-plagioclase. *Advanced Powder Technology* **2017**, *28*, 473–480, doi:10.1016/j.apt.2016.11.002.
173. Welsch, A.-M.; Behrens, H.; Ross, S.; Murawski, D. Structural control of ionic conductivity in $LiAlSi_2O_6$ and $LiAlSi_4O_{10}$ glasses and single crystals. *Zeitschrift für Physikalische Chemie* **2012**, *226*, 491–511, doi:10.1524/zpch.2012.0230.
174. Zhao, Z.-F.; Zheng, Y.-F. Diffusion compensation for argon, hydrogen, lead, and strontium in minerals: Empirical relationships to crystal chemistry. *American Mineralogist* **2007**, *92*, 289–308, doi:10.2138/am.2007.2127.
175. Effenberger, H.; Fuess, H.; Müller, G.; Vogt, T. Crystal structure and hydrogen bonding in Li/H-exchanged petalite, $HAlSi_4O_{10}$. *Zeitschrift für Kristallographie* **1991**, *197*, 27–40, doi:10.1524/zkri.1991.197.1-2.27.
176. Effenberger, H. Petalit, $LiAlSi_4O_{10}$: Verfeinerung der Kristallstruktur, Diskussion der Raumgruppe und Infrarot-Messung. *TMPM Tschermaks Petr. Mitt.* **1980**, *27*, 129–142, doi:10.1007/BF01082403.
177. Burmeister, C.F.; Kwade, A. Process engineering with planetary ball mills. *Chem. Soc. Rev.* **2013**, *42*, 7660–7667, doi:10.1039/c3cs35455e.
178. Sato, A.; Kano, J.; Saito, F. Analysis of abrasion mechanism of grinding media in a planetary mill with DEM simulation. *Advanced Powder Technology* **2010**, *21*, 212–216, doi:10.1016/j.apt.2010.01.005.
179. Li, C.-T. Transformation mechanism between high-quartz and keatite phases of $LiAlSi_2O_6$ compositon. *Acta Cryst.* **1971**, 1132–1140.
180. López, M.C.; Ortiz, G.F.; Arroyo-de Dompablo, E.M.; Tirado, J.L. An Unnoticed Inorganic Solid Electrolyte: Dilithium Sodium Phosphate with the Nalipoite Structure. *Inorg. Chem.* **2014**, *53*, 2310–2316, doi:10.1021/ic4030537.
181. Franger, S.; Le Cras, F.; Bourbon, C.; Rouault, H. $LiFePO_4$ Synthesis Routes for Enhanced Electrochemical Performance. *Electrochem. Solid-State Lett.* **2002**, *5*, A231, doi:10.1149/1.1506962.
182. Maccario, M.; Croguennec, L.; Wattiaux, A.; Suard, E.; Lecras, F.; Delmas, C. C-containing $LiFePO_4$ materials — Part I: Mechano-chemical synthesis and structural characterization. *Solid State Ionics* **2008**, *179*, 2020–2026, doi:10.1016/j.ssi.2008.07.004.
183. Hughes, J.M. The many facets of apatite. *American Mineralogist* **2015**, *100*, 1033–1039, doi:10.2138/am-2015-5193.

List of Figures

Figure 1-1. Investigated lithium sources including end-of-life LAS glass-ceramic and primary lithium silicate minerals such as lepidolite, spodumene and petalite. 2
Figure 2-1. Reported defects in mechanical activated crystalline solids including point defects (Frenkel and Schottky defects), dislocations, amorphous regions and grain boundaries. Redrawn from [29]. 4
Figure 2-2. Schematic drawing of the magma-plasma model for mechanochemical reactions after Thiessen et. al [40], where (E) represents excited electrons, (N) the non-deformed solid, (D) the deformed surface layer and (P) the triboplasm. Image reproduced from [31]. 5
Figure 2-3. Pseudo-fluid model for mechanochemical reactions, where the blue and red spheres represent reactant particles, which were converted to a product (black) while milling. Thereby the contact reaction occurring between reactants is fast but self-limiting due to the formation of a product layer at the interface (a). Therefore, continuous milling is required for entire transformation of the reactants to the product phase (b). Figure reproduced from [41]. 6
Figure 2-4. Schematical drawings of different mill types, capable for mechanochemical treatments, including (a) ball mill, (b) planetary ball mill, (c) vibration mill, (d) attritor mill (also known as stirring ball mill), (e) pin mill and (f) roller mill. Image reproduced from [42]. 7
Figure 2-5. Schematic showing the comminution mechanisms occurring in planetary ball mills including impact, friction and shear scenarios. Besides the comminution of particles, partly amorphous samples were observed during mechanical activation experiments. Own work, reproduced from [43]. 7
Figure 2-6. Summary of the most important reactions of lithium. Please note, there was no consideration of the stoichiometry and the exact reaction conditions. Image Redrawn from https://commons.wikimedia.org /wiki /File: Lithium _reactions.svg 10
Figure 2-7. Relevant examples of worldwide lithium deposits and operations; (a) reveals evaporation ponds of a lithium brine operation in the Salar de Atacama, Chile, (b) represents a geological map of the Greenbushes pegmatite deposit in Western Australia with predominant tin, tantalum and lithium mineralization, while (c) shows an enormous spodumene crystal of up to 14 m in length and 82 t in weight, which was mined as lithium ore at the renowned Etta Mine in the Black Hills of South Dakota, U.S. at the beginning of the 20th century. Figures adapted and slightly modified from [77–79]. 11
Figure 2-8. Pressure-temperature phase diagram for lithium aluminosilicates under quartz-saturated conditions, occurring in LCT-type pegmatites. Redrawn from [84]. 13
Figure 2-9. Global mine production in t of lithium for 2022, sorted by country. Own figure, data derived from [4]. 16
Figure 2-10. Estimates of the global end-use markets for lithium compounds in 2022. Own work, data derived from [4]. 23
Figure 2-11. Schematic drawing of a conventional LIB cell during discharging (a) and charging (b), while illustrating the most relevant components including anode, cathode, separator, electrolyte and collector foils. Figure adapted and slightly modified from Goodenough & Park [124]. 24
Figure 2-12. Idealized crystal structure on the unite cell level of a hexagonal high-quartz derived LAS phase, with a chemical composition of $Li_{0.33}Al_{0.33}Si_{0.67}O_2$, where significant amounts of the initial SiO_2 were substituted by Al_2O_3 and Li_2O to stabilize the structure for room temperature applications. Note that the figure was created with the use of VESTA 3 [134] employing atomic radii. 26
Figure 3-1. (a) to (c) Glass-ceramic samples derived from an end-of-life cooktop, (a) shard after manual dismantling, (b) after jaw crushing and (c) powder < 500 µm. (d) to (f) Lepidolite samples from the Bikita pegmatite, Simbabwe, (d) as received, (e) flakes after jaw crushing and (f) powder < 500 µm. (g) to (i) Spodumene samples from the Sahatany pegmatite, Madagascar, (g) as received, (h) cleavage pieces after jaw crushing and (i) powder < 500 µm. (j) to (l) Petalite samples from the Luolamäki pegmatite, Finland, (j) as received, (k) cleavage pieces after jaw crushing and (l) powder < 500 µm. 28
Figure 3-2. Graphical abstract of typical experimental parameters during mechanochemical sample treatment. Own work, reproduced from [43]. 29
Figure 3-3. Flowchart of analytical techniques applied during this work to evaluate liquid and solid samples, arising during mechanochemical investigations or the associated hydrometallurgical procedures. The corresponding samples are marked in ochre, while the methods are highlighted in blue. 33
Figure 3-4. Relevant components of an ICP-OES system. The most remarkable feature of this type of spectrometer is the argon plasma, in which the injected substances are immediately atomized at high temperatures, while atoms and

ions are subsequently excited to emit electromagnetic radiation, thereby providing a chemical fingerprint of the sample. Figure adopted from [146]. 34
Figure 3-5. Typical PXRD setup in Bragg-Brentano geometry including several beam optics to ensure a high signal-to-noise ratio. During the measurements, both the X-ray tube and the detector are moved upwards to collect data at higher 2Θ angles. Figure adopted from [147]. 35
Figure 3-6. Schematic illustration of a Michelson interferometer adopted for Fourier transform infrared (FT-IR) investigations. Figure adopted from [152]. 36
Figure 3-7. Gas adsorption/desorption investigations exemplarily shown for one of the zeolite samples. (a) Full adsorption/desorption isotherm and (b) BET plot based on a 10-point measurement at relative pressures between 0.05 and 0.3 p/p_0, which represents the linear section of the isotherm (a). The intercept (i) and the slope (s) in (b) are considered for the calculation of the monolayer adsorption v_m, which in turn is necessary for the determination of the BET surface area S_{BET} according to equation (25). 37
Figure 4-1. Diffraction patterns of the investigated source materials revealing the presence of lithium-rich phases besides minor amounts of cogenetic phases or trace minerals. (a) LAS glass-ceramic (LAS), (b) lepidolite (Lpd), (c) spodumene (Spd) and (d) petalite (Ptl). Own work, reproduced from [23,24]. 43
Figure 4-2. Optical microscopy images of source material powders (≤ 500 µm) after pretreatment: (a) LAS glass- ceramic, (b) lepidolite, (c) spodumene and (d) petalite. 44
Figure 4-3. SEM-SE micrographs at different magnifications with corresponding SEM-EDS measurements of selected areas of (a) to (c) LAS glass-ceramic (LAS), (d) to (e) lepidolite (Lpd), (g) to (i) spodumene (Spd) and (j) to (l) petalite (Ptl) samples, highlighting the most prominent cleavage planes and the areas where EDS data were acquired. Notably, small EDS signals of C and Cu originate from sample coating. 45
Figure 4-4. TEM investigations on glass-ceramic samples. (a) and (b) represent TEM-BF micrographs with corresponding SAED and EDS measurements, revealing β-SiO_2 (*P*6_222) and $ZrTiO_4$ (*Pbcn*) crystallites *in a glassy matrix, while HRTEM images (c) and (d) reveal nanosized* $ZrTiO_4$ *crystallites in* [1-10] *and* [0-10] *orientation. Own work, reproduced from [163].* 46
Figure 4-5. (a) Effect of NaOH concentration and reaction time on the lithium extraction. Corresponding PXRD patterns of the leaching residues obtained after mechanochemical treatments for (b) 30 min; (c) 60 min and (d) 120 min at various NaOH concentrations in the range of 1 to 9 mol/L. During these investigations, the rotational speed and BPR were kept constant at 600 rpm and 50 g/g. Own work, reproduced from [23]. 50
Figure 4-6. Zeolite frameworks being present in leaching-residues such as (a) GIS, (b) LTA, (d) SOD, (e) LTN, while (c) reveals the building units of these structures. Note that the frameworks and building units are simplified representations of the structures focusing on the bonding of aluminum and silicon, while oxygen atoms and metal ions (e.g., Na^+) are not shown for better illustration. Therefore, the corners of the polyhedra represent a silicon or aluminum atom, while each polyhedron edge symbolizes a Si-O-Al bond. Figures reproduced from Baerlocher and McCusker [167]. 51
Figure 4-7. (a) Effect of the rotational speed on the lithium extraction and the temperature during mechanochemical treatment. (b) Corresponding PXRD patterns of the leaching residues. Experiments were conducted for 60 min at different rotational speeds ranging from 200 to 600 rpm, while all other parameters were kept constant at 7 mol/L, 50 g/g, and 60 min. Own work, reproduced from [23]. 53
Figure 4-8. (a) Effect of the ball-to-powder ratio (BPR) on the extraction rate and the temperature during mechanochemical treatment. (b) Corresponding PXRD patterns of the leaching residues. During this study the BPR was varied in the range of 20 to 50 g/g, while other parameters were retained at 7 mol/L, 600 rpm, and 60 min. Own work, reproduced from [23]. 53
Figure 4-9. Diffraction patterns (PXRD) of the leaching residues after mechanochemical treatment for 120 min without and with intermittence. During the intermittent experiments, 12 intervals were run, each consisting of 10 min of milling and a 10 min break for cooling, reaching a total milling time of 120 min. NaOH concentration, rotational speed and ball-to-powder ratio (BPR) are kept constant at 7 mol/L, 600 rpm, and 50:1 g/g. SOD and LTN stand for hydrosodalite and zeolite N, respectively. Own work, reproduced from [23]. 54
Figure 4-10. PXRD patterns of the leach residues after regular leaching for 120 min and 360 min at 90 °C using 7 mol/L NaOH and s liquid-to-solid ratio (LSR) of 10 mL/g. Here, SOD and LTN are abbreviations for hydrosodalite and zeolite N, respectively. Only after a prolonged leaching time of 360 min the initial high quartz phase started to decompose. Own work, reproduced from [23]. 55
Figure 4-11. SEM-BSE image of a particle cross-section obtained after regular leaching under optimal conditions including 12 hours reaction time at 2 mol/L NaOH. It indicates the presence of a core-shell particle consisting of a LAS core surrounded by a layer of Na-rich aluminosilicate, which has been identified as the GIS-type zeolite according to PXRD measurements on corresponding samples. Figure adapted and slightly modified from Lee et al. [122]. 56

Figure 4-12. PXRD patterns of the glass-ceramic starting material compared to samples ball-milled in water for 30; 60 and 120 min to obtain reference data without chemical side reaction. The broadening of the main diffraction peak at 29.5 °2Θ was selected to estimate variations in the crystallite size with the aid of the Scherrer equation. 57
Figure 4-13. (a) PXRD patterns and (b) FTIR spectra of the starting material compared to byproducts (leaching residues) obtained after 30; 60 and 120 min of ball-milling in alkaline solution. Experimental parameters such as concentration, rotational speed and BPR were retained at 7 mol/L, 600 rpm, 50:1 g/g, respectively. Own work, reproduced from [23,163]. 58
Figure 4-14. (a) SEM and (b) TEM micrographs including localized EDS measurements of leaching residues obtained at optimum conditions (7 mol/L NaOH, 120 min reaction time), revealing the presence of euhedral crystals of LTN, which was identified via SAED in conjunction with EDS. Own work, reproduced from [163]. 60
Figure 4-15. Recovery rates for lithium extracted from the minerals petalite, lepidolite, and spodumene at different reaction times using 7 or 9 mol/L sodium hydroxide solution. Own work, reproduced from [24]. 62
Figure 4-16. PXRD patterns of the leaching residues based on lepidolite (a) and spodumene (b) after mechanochemical treatment using 7 mol/L NaOH solution at different reaction times. Own work, reproduced from [24]. 63
Figure 4-17. (a) PXRD patterns and (b) FT-IR spectra of petalite based leaching residues after mechanochemical treatment using 7 mol/L NaOH solution at different reaction times. Own work, reproduced from [24]. 64
Figure 4-18. SEM-SE micrographs of petalite based leaching residues obtained under optimal conditions (7 mol/L NaOH, 120 min ball milling). In (a) a remnant of an unreacted petalite cleavage lamella surrounded by hydrosodalite crystals is revealed, while (b) exhibits intergrown isometric hydrosodalite (SOD) crystals with a distinct dodecahedral habit. Corresponding SEM-EDS measurements (b) confirmed Na, Al, Si, and O as the main components of sodalite, while small signals of Fe and Cu originate from iron-rich fragments or sample coating. Own work, reproduced from [24]. 65
Figure 4-19. Diffraction patterns (PXRD) of reference samples, obtained by ball milling of (a) lepidolite, (b) spodumene and (c) petalite specimens in water for different times. All samples revealed a broadening of main diffraction peaks, which was further applied for crystallite size estimation via the Scherer equation. 67
Figure 4-20. Particle sizes (d_{50}) of reference samples, which were ball milled for various times in water. Notably these values were acquired via laser diffraction measurements on dry dispersed samples. 67
Figure 4-21. Idealized crystal structures on the unite cell level of the investigated minerals (a) lepidolite; (b) spodumene and (c) petalite. The grayish colored areas indicate the most important cleavage planes within the structures, while the orientation of the unit cell is given next to each structure. Note that the figures were created using VESTA 3 [134] employing atomic radii. 68
Figure 4-22. Desilication of the Li-enriched solution became mandatory as an intermediate step prior to the precipitation of a lithium compound. Therefore, the desilication behavior of petalite-based solutions were studied at various CaO-SiO_2 ratios ranging from 0.6 to 1.4. Own work, reproduced from [24]. 74
Figure 4-23. PXRD patterns of desilication products revealed the predominant formation of torbermorite ($Ca_5Si_6O_{16}(OH)_2 \cdot 4H_2O$), which can be further converted into wollastonite ($Ca[SiO_3]$) via calcination at 900 °C for 30 min. Own work, reproduced from [24]. 74
Figure 4-24. PXRD patterns of lithium phosphates obtained after precipitation with H_3PO_4 using various P:Li ratios ranging from 1.0:3.0 to 1.8:3.0. Own work, reproduced from [24]. 76
Figure 4-25. PXRD patterns of products obtained during transformation of precipitated Li_3PO_4. (a) hydroxylapatite byproduct and (b) intended lithium hydroxide obtained after crystallization of the solution. Own work, reproduced from [24]. 77
Figure 4-26. Removal efficiency as a function of zeolite dosage (g/L) in synthetic wastewater solutions containing the heavy metal ions Pb^{2+}, Cu^{2+}, Zn^{2+} and Ni^{2+}. Here, (a) concerns the application of a SOD/LTN mixture derived from LAS glass-ceramics, while (b) shows the result obtained when SOD based on petalite was investigated. 79
Figure 5-1. Graphical summary of the holistic approach adopted to LAS glass-ceramics, which involved a mechanochemical treatment as a key component, converting the feed material into a hydrosodalite zeolite, while lithium was significantly leached into the solutions. In addition, downstream processing of the NaOH solution included desilication prior to precipitation of Li_3PO_4, while the zeolite by-product was potentially considered as an adsorbent for heavy metal ions from aqueous solutions. 82
Figure 5-2. Graphical summary of the mechanochemical treatments of the lithium silicate minerals lepidolite, spodumene and petalite. These investigations revealed petalite to be much more suitable for this approach, as the lower coordination of lithium and the activation of cleavage planes along specific crystallographic lithium sites during ball milling significantly enhance the leaching. The downstream processing of the enriched solution involved several operations to obtain $LiOH \cdot H_2O$ as a final product. During these intermediate steps, particular attention was paid to obtain value-added byproducts such as wollastonite or apatite, contributing to the holistic approach. 83

List of Tables

Table 2-1. Most important lithium-bearing minerals including their chemical composition and theoretical lithium content [75,79]. The three minerals highlighted in blue will be discussed in more detail throughout the text. For better comparison with the own analysis data, the lithium content of each mineral was additionally converted into lithium oxide values. 12
Table 2-2. Selected physical and optical properties of investigated lithium minerals [88–90]. Highlighted in blue are the Mohs hardness and the coordination of the lithium, which are of particular importance for wear of the milling balls and the lithium extraction during the mechanical-chemical treatments. 14
Table 2-3. Methods reported in the literature for Li extraction from hard rock ores, including the most relevant reagents required, which are discussed in the following subsections [12,97]. The abbreviation sc stands for super critical. 18
Table 3-1. Solubility of relevant lithium and sodium salts at different temperatures [141]. Most notable is the generally low solubility of Li_3PO_4 and the temperature-dependent solubility of Li_2CO_3, both of which are relevant for lithium precipitation. 31
Table 4-1. Chemical composition of the feed materials based on ICP-OES measurements, recalculated into oxide values. The values in bold are discussed in the following section, while the Li_2O content is highlighted additionally in blue as it is most relevant to this study. Highlighted in green is the loss on ignition (LOI), which corresponds to the proportion of volatile components in the starting materials. 42
Table 4-2. Structural details on relevant zeolite frameworks, obtained during mechanochemical treatments of LAS glass-ceramic samples. Data derived from [167]. 52
Table 4-3. Particle sizes of glass-ceramic samples in reference experiments, based on ball-milling in water instead of NaOH solution. Values were obtained from laser diffraction measurements. 57
Table 4-4. Indexed absorption bands of hydrosodalite (SOD) shown in the FT-IR spectra (see Figure 4-13). 58
Table 4-5. BET surface area of LAS glass-ceramic-based samples in dependency of reaction time and phase composition. 59
Table 4-6. BET surface area of petalite-based samples depending on reaction time and phase composition. 66
Table 4-7. Wear of the stainless-steel grinding balls [g/h] determined during the mechanochemical treatment of various samples in comparison to their Mohs hardness. These values were experimentally acquired at identical milling parameters involving the use of 7 mol/l NaOH, rotational speed of 600 rpm, milling balls of 10 mm and a BPR of 50 g/g, corresponding to the use of 500 g balls per 10 g sample. Highlighted in red is the spodumene sample, which caused severe wear during the ball milling experiments. 71
Table 4-8. Lithium recovery and obtained products using different P:Li ratios. Notably, the recoveries were calculated based ICP-OES investigations on liquid samples, while the phases present in the solids were determined via PXRD. In addition, the optimum ratio which enabled the precipitation of a Li_3PO_4 single phase is highlighted in blue. 75
Table 4-9. Summary of relevant adsorptions studies, including zeolite precursors, zeolite phases and a comparison of removal efficiencies [%] for divalent heavy metal ions in wastewater solutions at a zeolite dosage of 6 g/L. The own results are highlighted in blue. 80

Acknowledgments

First and foremost, I would like to thank Prof. Dr. Hans-Joachim Kleebe for giving me the opportunity to write this dissertation in the research group of Geomaterial Sciences. I am especially grateful for his encouraging support and his constructive and motivating advices, which contributed significantly to the success of this thesis. Furthermore, I would like to thank him very much for his great interest in the topic of the thesis, which is situated partly aside from his common research focus.

I would like to express my gratitude to Prof. Dr. Christoph Schüth for his work as second reviewer and to the committee members Prof. Dr. Anke Weidenkaff and Prof. Dr. Jörg J. Schneider for their time and interest.

Likewise, I am grateful to the institute and department leadership of the Fraunhofer IWKS, especially Prof. Dr. Anke Weidenkaff and PD Dr. habil. Benjamin Balke-Grünewald for giving me the space and opportunities to work in a pleasant and rewarding environment. I would also like to thank all colleagues from Fraunhofer IWKS and TU Darmstadt who have provided me with exceptional support in my experimental and analytical work over the past few years. In that sense, I would like to thank Nina Kintop, Regine Peter, Jürgen Dieter Rossa, Birgit Huth and Konrad Opelt for their tremendous assistance during ICP-OES, BET, SEM, LOI and particle size analysis, respectively. Particularly, I also would like to express my gratitude to Dr. Isabel Kinski and Dr. Songhak Yoon for their support with analytic methodology, their helpful scientific advices and the fruitful discussions on PXRD data. My special thanks goes to Dr. Johannes Peter for his efforts and advices with the TEM measurements, the intensive scientific exchange and the good cooperation in so many things. Moreover, I am grateful to David Magnus Wolf and Johannes Stein, who supported me in the laboratory during their Master's thesis.

I would like to extend my gratitude to Dr. Katrin Berberich, who always found the time to discuss results or make constructive recommendations. I highly appreciate her scientific input and I am pleased that I was able to benefit from her experience and knowledge, particularly in the field of zeolite sciences.

Now, I would like to thank all of my doctoral colleagues from TU and IWKS such as Max, Johannes, Kerstin, Ann-Katrin, Emilia, Marius and Ronja for the enjoyable time together, the academic and non-academic discussions and the occasional after-work activities.

I would like to thank my family and my parents for their constant encouragement during my doctorate and in all circumstances.

Finally, I would like to thank my wife Cathrin and my son Philipp for their unlimited moral and mental support through all the ups and downs and for always being there for me.

Publications & Conference Contributions

Publications

1. **Necke, T.**; Stein, J.; Kleebe, H.-J.; Balke-Grünewald, B. Lithium Extraction and Zeolite Synthesis via Mechanochemical Treatment of the Silicate Minerals Lepidolite, Spodumene, and Petalite. *Minerals* **2023**, *13*, 1030, doi:org/10.3390/min13081030.

2. Choi, B.; Domínguez, B.; D'Souza, A.; Khadse, H.; Kunkel, A.; Nagarajan, S.; **Necke, T.**; Peche, R., Revello, M.; Rossa, J.; Sauer, F.; Huyer, S., Schulz, O., Vorwerg, S.; Walls, C.; Wickleder, M.; Beck, G. Sustainable recycling process for tantalum recovery from printed circuit boards. *Resources, Conservation and Recycling* **2023**, *198*, 107201, doi:org/10.1016/j.resconrec.2023.107201.

3. Holzer, A.; Zimmermann, J.; Wiszniewski, L.; **Necke, T.**; Gatschlhofer, C.; Öfner, W.; Raupenstrauch, H. A Combined Hydro-Mechanical and Pyrometallurgical Recycling Approach to Recover Valuable Metals from Lithium-Ion Batteries Avoiding Lithium Slagging. *Batteries* **2023**, *9*, 15, doi:org/10.3390/batteries9010015.

4. **Necke, T.**; Wolf, D.M.; Bachmann, A.-L.; Berberich, K.; Kleebe, H.-J. and Weidenkaff, A. Mechanochemical Lithium Extraction and Zeolite Synthesis from End-of-Life Glass–Ceramics *ACS Sustainable Chemistry & Engineering* **2022**, *10*, 10849-10857, doi: 10.1021/acssuschemeng.2c02342.

5. **Necke, T.**; Trapp, M.; Lauterbach, S.; Amthauer, G. and Kleebe, H.-J. Electron microscopy investigations on the mineral lorándite ($TlAsS_2$) from Allchar in Macedonia. *Zeitschrift für Kristallographie - Crystalline Materials* **2021**, *236*, 51-60, doi:org/10.1515/zkri-2020-0070.

Conference Contributions

1. **Necke, T.**; Peter, J.; Rossa, J.D.; Kleebe, H.-J.; Balke, B.; Weidenkaff, A. Investigations on Lithium-containing Glass-Ceramics during Mechanochemical Recycling. *Microscopy Conference, Darmstadt, Germany*, 02/2023 (poster presentation).

2. **Necke, T.**; Bachmann, A.-L.; Bokelmann, K.; Homm, G.; Weidenkaff, A.; Kleebe, H.-J. Mechanochemistry: Sustainable extraction and recovery of metals: The case of lithium silicate minerals. *International Conference on Resource Chemistry, Alzenau, Germany*, 03/2021. (poster presentation).

3. **Necke, T.** Mechanochemie - Nachhaltige (Rück)gewinnung versorgungskritischer Rohstoffe, *Ressourceneffizienz-Kongress „24 Stunden für Ressourceneffizienz“, Pforzheim, Germany*, 02/2019, (oral presentation, **best presentation award**).